Study of 3D-Printed Polymers for Aerospace Structural Applications

Jacob Chekal

A thesis
submitted in partial fulfillment of the
requirements for the degree of

Master of Science in Civil Engineering

University of Washington

2021

Committee:

Richard Wiebe, Chair

Dawn E. Lehman

Michael Motley

Program Authorized to Offer Degree:
Civil and Environmental Engineering

©Copyright 2021

Jacob Chekal

University of Washington

Abstract

Study of 3D-Printed Polymers for Aerospace Structural Applications

Jacob Chekal

Chair of the Supervisory Committee:
Assistant Professor Richard Wiebe
Civil and Environmental Engineering

This work focuses on the use of additively manufactured polymers for the design of parts subjected to structural loads and environmental degradation. A major advantage of additive manufacturing is the ability to produce parts with complex geometries that would be costly or infeasible with other manufacturing techniques. A major disadvantage of additive manufacturing is the large knowledge gap that exists in the performance of additively manufactured polymers. This project sought to help fill that knowledge gap through pristine material testing and environmental degradation testing, as well as developing protocols to help overcome some of the challenges of using additive manufactured polymers.

The project focused on a case study problem, that of a service access door for a Boeing airliner. The focus of the work was initially to identify a candidate set of materials and printing processes. After this, the focus was to characterize the behavior of the set of materials through testing. This material characterization was used to reduce the list of possible material systems to two candidates to be considered for future work for this project. The work also focused on the design of a new access door that would be suitable for the materials and printing processes selected for this project. The work

then focused on testing subcomponents of the final designs to characterize the behavior of built-up parts printed with additively manufactured polymers.

Acknowledgements

This thesis and the research presented were made possible because of the help and support of many family, friends, staff, and organizations. I must first thank Boeing for continuing to strive for innovations in the field of aerospace and structural engineering which led to the funding of this project.

I am most grateful to my thesis adviser, Professor Richard Wiebe for approaching me with this project. His knowledge and passion for experimental and analytical research were a tremendous help to my thesis. Also, this project was started and completed during the Covid-19 pandemic in the United States, and I must thank him for striving to find ways to ensure that work could still continue on this project in a safe and efficient manner.

I must also thank William F. Kuykendall, the lab engineer in the mechanical engineering labs during this project, for continuing to assist me during the testing phase of this project. Due to the Covid-19 restrictions, their workload was very high between lab maintenance, new user training, remote labs, and test assistance however they were always able to find time to assist me when needed.

I would also like to thank Tatyana Galenko with the Material Science department at UW for coordinating with the project team and helping the team print with the Markforged printers in the MSE labs.

A special thanks to Eric Wang, Liam Quigley, and all of the BARC staff for their assistance and support on the project.

...

Contents

List of Figures

List of Tables

1 Introduction

1.1 Motivation

This research project focused on the potential use of additively manufactured materials, specifically polymers, on the fuselage, or shell, of an aircraft. Additionally, the aerospace industry is still in the early days of using additively manufactured polymers for structural applications. The motivation of this project was to explore the possibility of using additively manufactured polymers on the fuselage, but also to provide valuable insight into the use of additively manufactured polymers for structural applications in general. The project was funded by Boeing and was carried out in close collaboration with their engineers. The part selected for this study was a service access door on the fuselage. This service access door is considered to be non-structural. This means it is not a part of the load path needed to ensure flight safety, which includes pressurization. However, it is still subjected to structural loads during a flight, but the aircraft would still be able to make a safe landing if this part were to fail. As seen in Figure 1.1, this door is on the tapered part of the tail which is aft of the rear pressure cap.

The fact that this service access door is non-structural makes it an ideal part for introducing additive manufacturing to the fuselage of the aircraft. Additionally, this access door was selected because the current aluminum access door (see Figure 1.2) is a built-up part with many fastened components, and it requires a large amount of labor and is slow to manufacture.

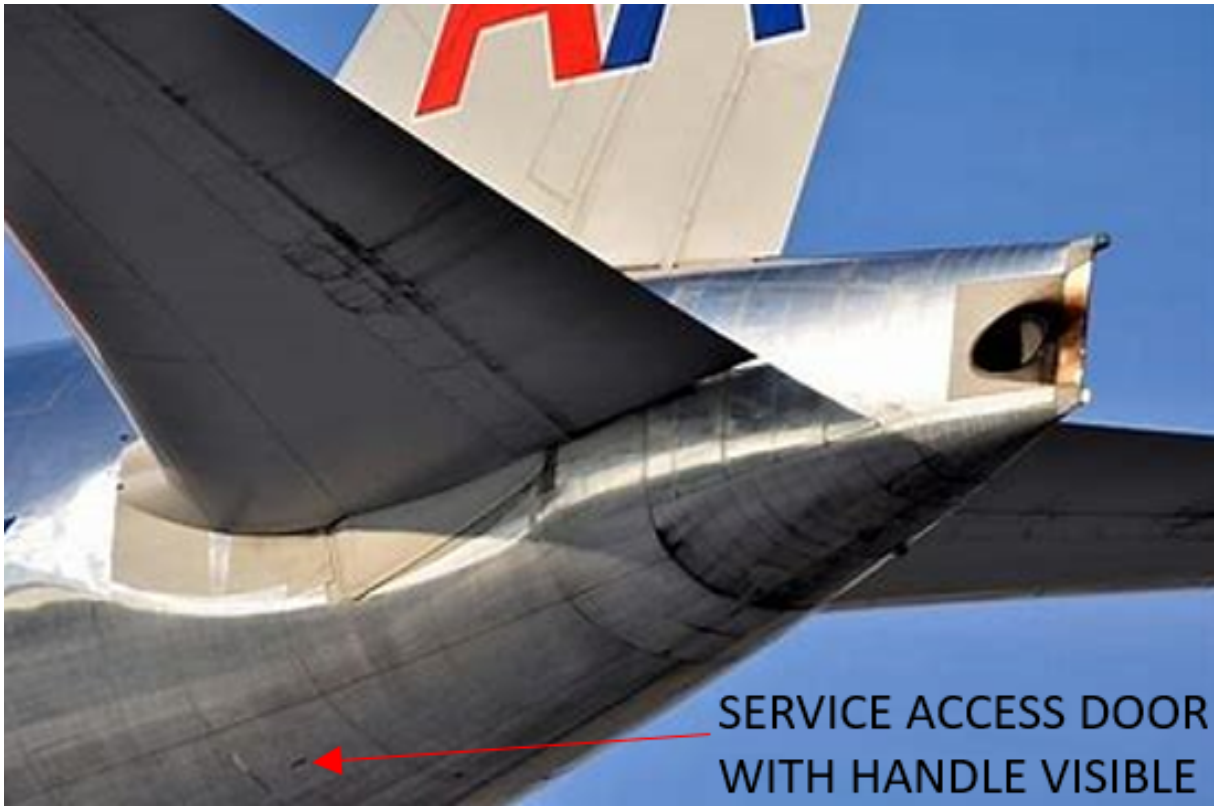

FIGURE 1.1: Existing access door location on aircraft

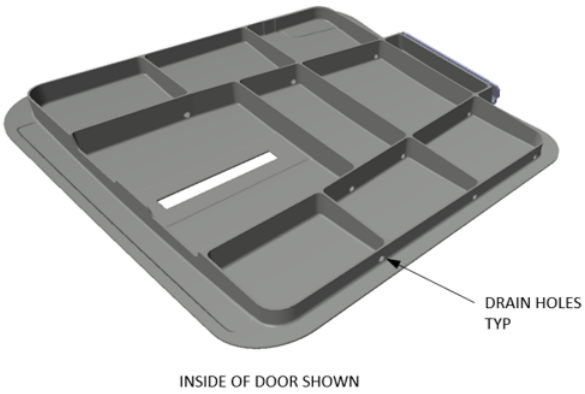

FIGURE 1.2: Existing door design

1.2 Problem Statement

This section discusses the project goals as well as the performance needs of the final part.

The first goal of the project was to identify suitable material systems to be used. This included identifying polymers and fiber reinforcing that would be suitable for structural applications. This also included identifying the associated 3D printing method and 3D printer to be used with the material systems. The choice was made by Boeing to use additively manufactured polymers for this project rather than additively manufactured metals due to the better corrosion protection and higher resistance to thermal expansion of polymers. The material systems to be used were to have a wide range in stiffness to explore if less costly materials would be feasible for the part.

The second goal of the project was to identify suitable panel geometries. The panel geometry would need to be able to withstand an ultimate transverse pressure load of 1.5 psi. This pressure load simulates the conditions of aft pressure bulkhead rupture. The panel would also need to withstand an abuse load of 150 lbs in an open door condition. This load simulates an impact load that could occur while the access door is open while the aircraft is on the ground. Additionally, the access door would need to be able to withstand the forces caused by a 65-knot wind gust while in an open position. In this project, the geometry was sized using the 1.5 psi pressure load. The part geometry in combination with the material systems selected would need to match the stiffness of the current aluminum access door, ensure no material yielding, and avoid local and global buckling under load.

The third goal of this project was to robustly characterize the structural performance of the material systems selected. This characterization would help determine which of the selected material systems would be suitable for future use on the project and for other structural applications.

The fourth goal of the project was to explore the effects of environmental degradation on the selected material systems. In use, the access door would be subjected to air erosion, UV degradation, salt spray, de-icing fluids, and temperature ranges from -65 to

210 degrees Fahrenheit. The material systems selected for this part need to show resistance to these forms of degradation. Due to time and testing equipment constraints, not all of these types of environmental degradation were tested. The project focused instead on degradation due to temperature cycling.

The fifth goal of this project was to explore knowledge gaps related to scaling in the additive manufacturing of polymers. This goal was presented because the part used in this project was too large to be printed using the printers available to the University of Washington or Boeing at the time of this project. Since the full part would not be able to be printed and tested, it was important to explore if testing smaller scale models would accurately predict the performance of the full-sized part.

1.3 Overview

This project included material selection (see Chapter 2), material testing (see Section 2.3), part geometry selection (see Section 5.2), part design (see Section 5.3), and structural analysis (see Section 5.4).

In Chapter 2, the material selection for the access door is investigated. This includes a preliminary material selection (see Section 2.2) and material testing results (see Section 2.3). The material testing in this section was done to characterize the materials to be used in the final part design.

In Chapter 3, special considerations of coupon and material behavior as well as testing protocols developed during this project are discussed. This includes an investigation of the yield strength of the materials tested in the project (see Section 3.2). This also includes a discussion of the protocol used for printing vertical coupons with the Fused Filament Fabrication (FFF) method of 3D printing. These vertical coupons proved difficult to print and required additional support during the printing process (see Section 3.3). Included in this section is also an investigation of the effect that coupon shape and

size had on the performance of the material for FFF printed coupons (see Section 3.4). Lastly, included in this section is a discussion of a protocol developed for determining the effect of printer layer time on the bond strength between layers in vertically printed FFF coupons (see Section 3.5).

In Chapter 4, the final recommendations for what materials should be used for future work on this project are discussed. These recommendations are based on the results and discussions presented in Chapters 2 and 3.

In Chapter 5, the geometry selection for the new access door design is discussed. This includes a discussion on the process used to determine what the new geometry for the part would be (see Section 5.2). Also included in this section are the design process used for sizing the geometry for the new part and the results of the sizing (see Section 5.3). Additionally, included in this section is a discussion of the structural analysis performed on the final design (see Section 5.4).

In Chapter 6, component testing is investigated. Component testing refers to printing a small section of the full final design and testing it. This was required because the full part was actually too large to print using any printer available to the University of Washington or Boeing during this project. This section includes the results of the component testing (see Section 6.2) and structural analysis of the components to determine the stresses in the components during testing (see Section 6.3). The component testing in this section explicitly looks at a qualitative study on the robustness of the bond between the web and flange of stiffeners when the stiffener is buckled.

In Chapter 7, future work that could be done on this project will be discussed.

2 Material Selection

2.1 Overview

The first step of the project was to select a set of candidate material systems. Material systems refer to a material, or potentially a composite, together with a print protocol. An initial set of candidates was chosen based on specified material properties given by material suppliers and based on the material availability. Once an initial set of candidates was selected, coupon testing was performed to characterize the material performance to determine which ones would be suitable for this project. After the material testing was completed, the list of possible material systems was reduced to two candidates to be considered for future work for this project (see Chapter 4). This section discusses the material selection process and the testing of the selected materials.

2.2 Preliminary Material Selection

The preliminary material selection for the service access door was the first step of the project. The list below shows the initial set of candidate materials. The process of selecting these materials and then down-selecting further is covered in this section.

- FR-106 by Advanced Laser Materials (ALM). This is a Nylon 11 powder used for Selective Laser Sintering (SLS) 3D printing (see Subsection 2.2.2) [*FR-106 - Material Specifications*].
- HT-23 by ALM. This is a chopped fiber reinforced Polyetherketoneketone (PEKK) powder reinforced with carbon fiber used for SLS printing [*HT-23 Overview*].

- HexPEKK by Hexcel. This is a chopped fiber reinforced PEKK powder reinforced with carbon fiber used for SLS printing [Hexcel Corporation, 2021].
- Onyx by Markforged. This is a chopped fiber reinforced nylon filament reinforced with carbon fiber used in Fused Filament Fabrication (FFF) printing (see Subsection 2.2.2) [Markforged, 2021c].
- Onyx with continuous carbon fiber reinforcement by Markforged. This is printed with the FFF method and uses the chopped fiber Onyx filament with a separate continuous Carbon Fiber filament for additional reinforcing [*Material Descriptions - Composites* 2020].
- ThermaX PEEK by 3DXTECH. This is a Polyether ether ketone (PEEK) filament used for FFF printing [*Technical Data Sheet: ThermaX™ PEEK 3D Printing Filament* 2021].

It can be seen in the list above that two common printing types, SLS and FFF, were chosen. The preliminary material selection was based on the raw material mechanical properties, the type of 3D printer used, and the material availability to both Boeing and the University of Washington (UW).

2.2.1 Raw Material Mechanical Properties

In this section, it is important to note a distinction between raw material properties and effective printed properties. The raw material properties are the properties intrinsic to the material without regard to the printing approach. The effective printed properties are how the material behaves after the printing process and can be largely affected by the printing approach used. The raw material properties considered for the preliminary material selection were stiffness, strength, ductility, and durability against environmental degradation. These properties would all determine if the access door would meet the loading and impact requirements for the part, which were determined by Boeing (see Section 1.2). With the final design goal of creating an access door to

go on the exterior of an aircraft fuselage, the part would need to be able to withstand environmental degradation (see Section 1.2). While it was important for the selected materials to have high durability when exposed to these environmental conditions, the paint applied to the part plays a large role in resisting the degradative effects of the environmental conditions listed above. The candidate materials were selected because they were either known to have good performance, or they were unknown, but the team (UW plus Boeing) was interested to see if they had good performance (particularly for low-cost materials).

2.2.2 Methods of 3D Printing

As discussed above, the project sought to employ two printing methods. These two methods are described in this section. Three materials listed above are printed using the SLS method which is a part of the Powder Bed method of 3D printing. The materials used in SLS printing start in granular powder form, then a laser selectively sinters the particles of the powder which fuses them together. This process is done as more layers of powder are added to the print bed until the printed part is complete [Varotsis, Alkaios B., 2021b]. Figure 2.1 shows a graphic of how the SLS printing process works.

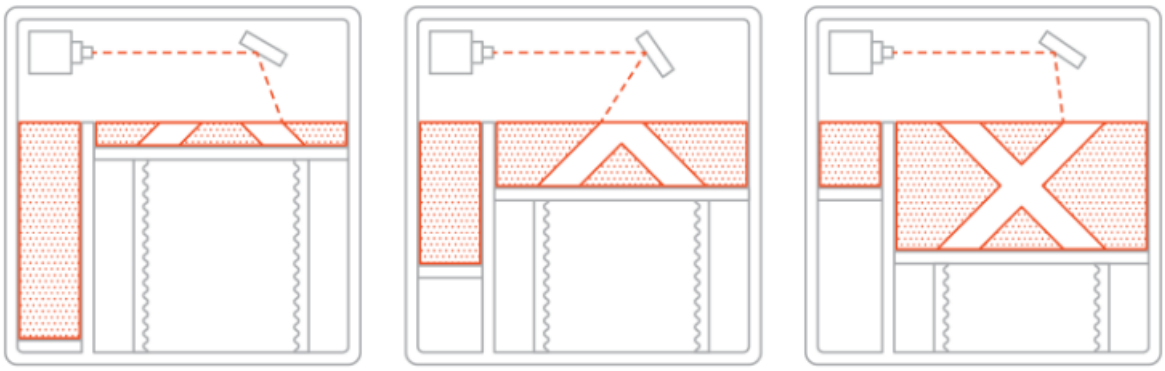

FIGURE 2.1: Printing of an X-shaped part using SLS printing. The powder bed is lowered and the reservoir maintains the top surface height [Varotsis, Alkaios B., 2021b]

One of the main advantages of the SLS method of 3D printing is the lack of support structures required, which are often required with complex FFF prints. As seen in Figure 2.1, the entire printer volume is filled with powder and the powder not required to print the part is simply not sintered. Each layer of powder supports the layer above it which removes the need for printed support structures. Another advantage of SLS printing is that it produces parts that are nearly isotropic [Varotsis, Alkaios B., 2021b].

While SLS prints require no support structures (but can still use them to allow for more uniform cooling through conduction), there is still a large amount of post-processing work to be done after the print is complete. The finished part is encased in powder and needs to be removed from the block of powder, and it needs to be cleaned off. Additionally, drainage holes are required for parts with hollow spaces in order to remove the powder within. Drainage holes are also a major problem for sandwich panels, which are common in aerospace structural parts. With a densely packed core of a sandwich panel, it would be very challenging to create drainage holes that would ensure all of the excess powder within each cell in the core could be removed. The extra post-processing work required to remove excess powder is one of the disadvantages of SLS printing [Varotsis, Alkaios B., 2021b]. Another disadvantage of the SLS printing process is the waste of material that occurs. Not all of the powder that is not sintered to the part is recyclable after the print is complete. This leads to more waste if the entire print volume is not being used. Additionally, when the SLS printing process is complete, the printers need to cool down. This is a long process for many SLS printers and can result in long wait times in between consecutive prints [Gregurić, Leo, 2019].

Two of the materials listed above are printed using the FFF method, also referred to as Fused Deposition Modeling (FDM). In this method of 3D printing, the material is heated and extruded through a nozzle that can move in the plane of the print bed, which are commonly referred to as the X and Y directions, as well as vertical or Z direction. The material is extruded layer by layer until the part is complete [Varotsis,

Alkaios B., 2021a]. Figure 2.2 shows a graphic of how the FFF printing process works.

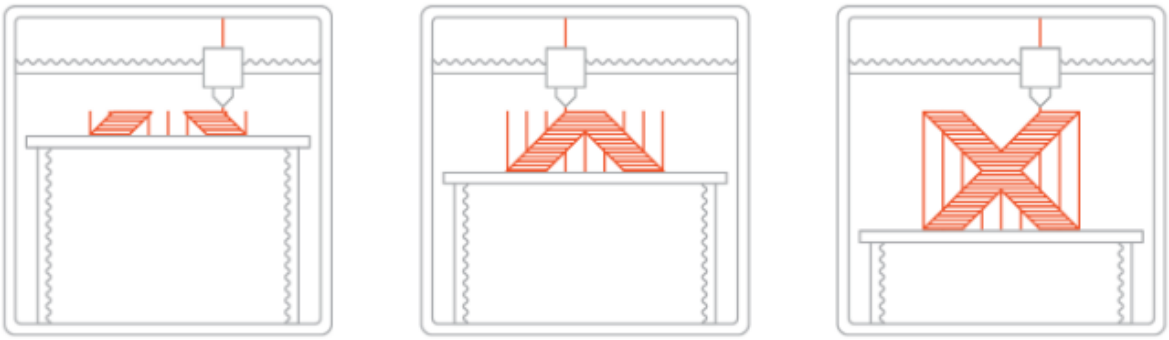

FIGURE 2.2: Printing of an X-shaped part using FFF printing. The print bed is lowered as the nozzle continues to deposit material layer by layer [Varotsis, Alkaios B., 2021a]

Additionally, some FFF printers use a second nozzle to simultaneously lay continuous strands of reinforcement material along with the original matrix material to create composite parts. Parts with continuous fiber reinforcement have better structural performance than parts printed with only the matrix material [Markforged, 2021a]. Figure 2.3 shows a graphic of how this process works.

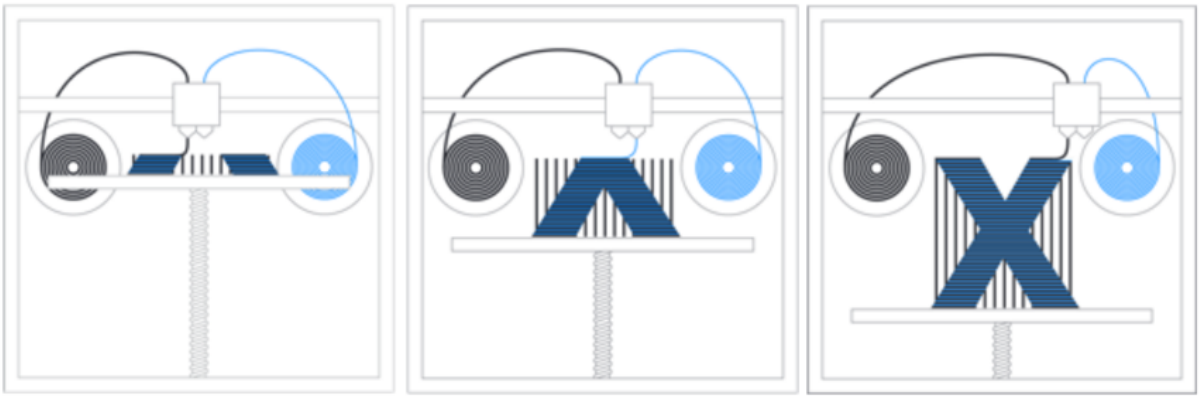

FIGURE 2.3: Printing of an X-shaped part using FFF printing with continuous fiber reinforcing. The print bed is lowered as the nozzles work together to deposit matrix and reinforcing material layer by layer [Markforged, 2021a]

One of the disadvantages of printing with continuous fiber reinforcement is that it reduces the level of geometric complexity that a part can be printed with.

One of the advantages of FFF printing is that the printer is ready to be used as soon as the previously printed part is removed from the print bed. Additionally, FFF printers allow the user to control the infill density of the part. Figure 2.4 shows the same part printed with varying infill densities.

FIGURE 2.4: Varying infill densities [Varotsis, Alkaios B., 2021a]

During an FFF print, the outer perimeter is traced using several passes. The outer perimeter layers are called the shell. The material inside the shell layers is referred to as the infill [Varotsis, Alkaios B., 2021a]. The user has a choice to print with solid or less dense infills. If a non-solid infill is chosen, the user can also choose the shape in which the infill is printed. Common infill shapes are triangular, rectangular, and hexagonal or honeycomb infills [Markforged, 2021b]. Figure 2.5 shows the same part printed with varying infill shapes.

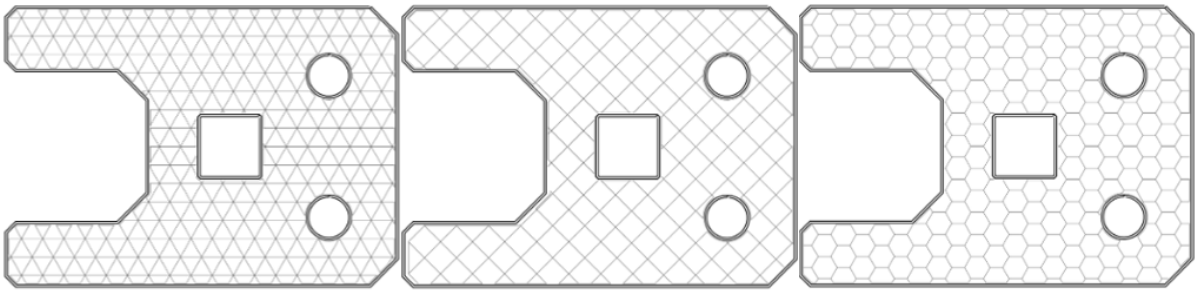

FIGURE 2.5: Varying infill types [Markforged, 2021b]

The number of shell layers used, infill density, and infill shape all affect the performance of a part. A study by [Rinaldi et al., 2018] investigated the performance between tensile coupons of varying infill densities, and it concluded that in parts with infill densities of less than 50%, the load is carried primarily by the shell layers. The ability to control shell thickness, infill density, and infill shape allows the user to place more material in critical locations and to use less material where it is not needed. Additionally, controlling the infill settings allows the user to have more control over the print speed of an FFF printer. While this is an advantage of FFF printing, this project focused only on solid infills for the FFF prints.

One of the main disadvantages of FFF printing is the part anisotropy that develops from the printing process. A part printed with FFF printing is anisotropic and the anisotropy depends on the raster angle, the print orientation, the printer settings, and the material being printed ["Experimental Characterization of the Mechanical Properties of 3D-Printed ABS and Polycarbonate Parts"]. The raster angle refers to the direction the extrusion nozzle moves in the XY plane. This project focused on raster angles of [00,90] and [-45,+45]. The raster angle for a part is given as two angles. The filament directions alternate between the two angles for each layer of a print. The print orientation refers to how the part is oriented on the print bed while being printed. Figure 2.6 shows an example of multiple tension coupons oriented on the print bed for multiple print orientations and raster angles. Figure 2.7 shows the outline of tension coupons with the raster angles of [00,90] and [-45,+45] that have the filament directions shown in red and blue. When raster angles or print orientations are mentioned in this thesis, they are consistent with the ones shown in these figures.

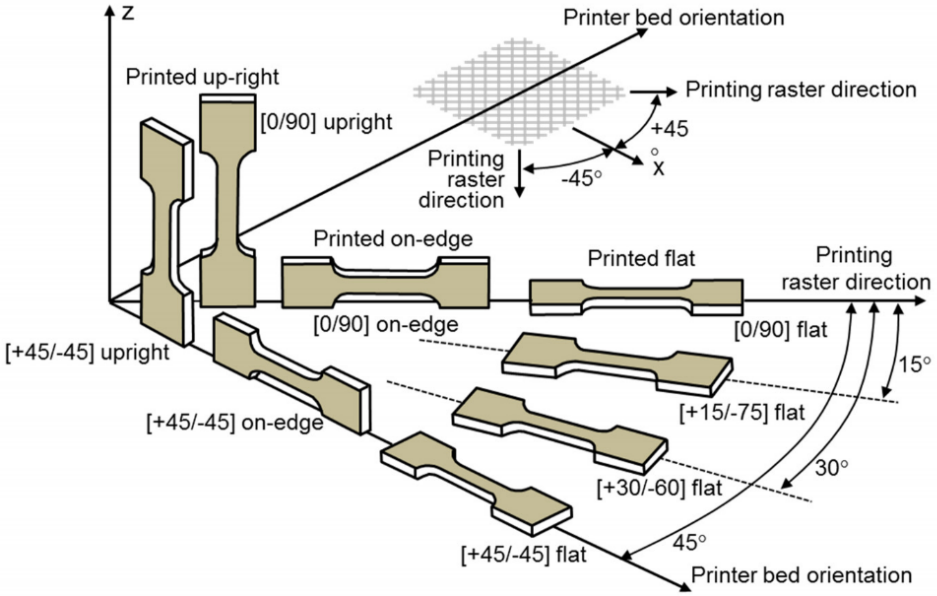

FIGURE 2.6: Varying raster angles and print orientations ["Experimental Characterization of the Mechanical Properties of 3D-Printed ABS and Polycarbonate Parts"]

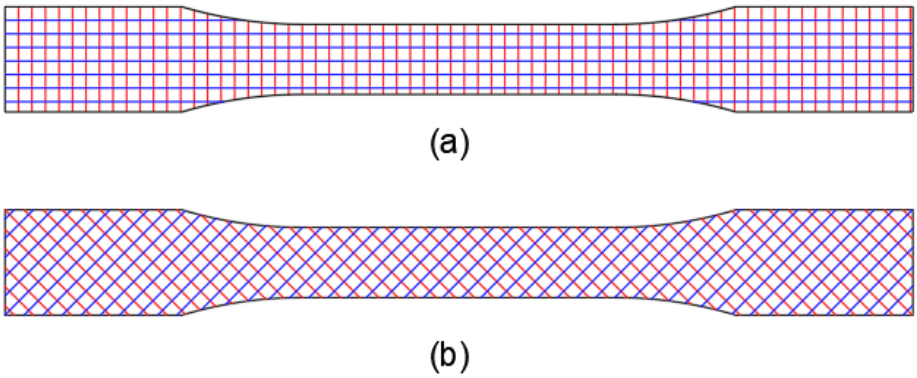

FIGURE 2.7: Tension coupons with filament directions shown in red and blue. (a) Raster angle [00,90] (b) Raster angle [-45,+45]

The combination of print orientation and raster angle determines if a part is loaded primarily through the filaments or the bonds between the layers. The bonds between the print layers are weaker than the printed material itself, which leads to parts with up-right or vertical print orientations having low performance in strength and ductility when compared to other print orientations [Rinaldi et al., 2018]. The bond strength between consecutive layers is affected by the material, the print temperature, and the

time it takes for a layer to be completed. The longer it takes for a layer to be completed, the worse the bond between the layers will be. Another disadvantage of FFF printing is the need for support material as seen in Figure 2.2. The melted material leaving the print nozzle cannot be deposited on thin air, therefore support structures are often required to hold up unsupported sections of the print. Parts requiring support structures require more material to print and more post-processing time to remove the supports from the finished part.

There are distinct advantages and disadvantages between the two methods of printing used in this project, but there are also shared advantages and disadvantages as well. The largest advantage shared between the two methods of printing is that they allow for the production of parts with complex geometries that would be difficult to construct by other manufacturing methods. One of the disadvantages shared between the two printing methods is that parts are susceptible to warping. Warping occurs due to different temperatures in a part during the printing process. As the uppermost layers of a part cool during the printing process, they shrink and pull the lower layers of the part up as shown in Figure 2.8 [Varotsis, Alkaios B., 2021a].

FIGURE 2.8: Warping of 3D printed part [Varotsis, Alkaios B., 2021a]

While both methods of printing have ways of mitigating this process, warping is something that needs to be considered by the user of the printer. Another disadvantage of 3D printing, in general, is that the same part with the same material can have varying

performance based on what printer settings and what printers are used [Markforged, 2021b][Rinaldi et al., 2018][Varotsis, Alkaios B., 2021b][Varotsis, Alkaios B., 2021a].

2.2.3 Material Availability

Material availability was the third consideration for the preliminary material selection. Boeing suggested the use of three SLS materials - FR-106, HT-23, and HexPEKK - however, limitations meant that only FR-106 and HT-23 were used. The FR-106 and HT-23 coupons were printed by third-party suppliers. The FR-106 coupons used for this project were supplied by Rapid Application Group, and the HT-23 coupons were supplied by EOS North America.

The material availability was the main driving factor for the selection of the FFF printer materials. The University of Washington campus had FFF printers by Markforged that could print both Onyx and Onyx with continuous carbon fiber reinforcement. The Markforged printers used were the Mark Two and X7. The Boeing Advanced Research Center (BARC) at UW also purchased a printer, the Intamsys Funmat HT Enhanced, capable of printing PEEK during the project, and was already planning to use ThermaX PEEK for a different project that was exploring rapid part prototyping. This made it ideal to coordinate with the other project team and to use ThermaX PEEK for this project as well. Once all the materials for the project were selected, it was time to print and test coupons.

2.3 Material Testing Results

The materials listed above, except for HexPEKK, were subjected to tension and bending tests to determine the pristine material performance and the performance of the material after environmental degradation. In this thesis, pristine performance refers to the behavior of the material before being subjected to environmental degradation.

Since these materials would be on the exterior of an aircraft, they would be subjected to multiple sources of environmental degradation (see Subsection 2.2.1); however, this project only explored the effects of degradation due to temperature cycling without humidity control. Ideally, it is best to perform temperature cycling simultaneously with humidity control to simulate the freeze and thaw cycles that a part would experience in real-world conditions, but the environmental chamber used for this project was not capable of controlling humidity. Additionally, thermal cycling was performed and then the coupons were tested at room temperature. This method of thermal testing is often used in the aerospace industry to check fatigue caused by thermal cycles. Thermal testing at high or low temperatures can also be done to explore the effect of temperature on strength. While this is a useful approach to determine the effects of thermal degradation, it is less used in the industry because it requires expensive equipment.

The tension tests were performed in accordance with ASTM D638-14 [*Standard Test Method for Tensile Properties of Plastics* 2014] (see Appendix A). The bending tests were performed in accordance with ASTM D790-17 [*Standard Test Methods for Flexural Properties of Unreinforced and Reinforced Plastics and Electrical Insulating Materials* 2017] (see Appendix B). While bending tests were performed for most of the materials considered for this project, tension testing was the main method of characterizing the materials. This was because of the fact that many of the bending coupons did not experience failure before the end of test strain limit. When materials do not fail in bending before the end of test strain limit is reached, ASTM recommends the use of other testing methods to characterize the material, such as tension testing [*Standard Test Methods for Flexural Properties of Unreinforced and Reinforced Plastics and Electrical Insulating Materials* 2017]. The test results for the materials chosen from the preliminary material selection are presented and discussed in the following sections. These test results led to the list of possible materials to be reduced to two candidates to be considered for future work

on this project (see Chapter 4). Extensive testing reports are available for each material system which are available upon request. This section will summarize those test reports.

2.3.1 FR-106 (SLS Printing) Test Results

The FR-106 material was tested in tension using Type I tension coupons (see Appendix A). The results of the pristine tension testing are shown in Figure 2.9 and Table 2.1.

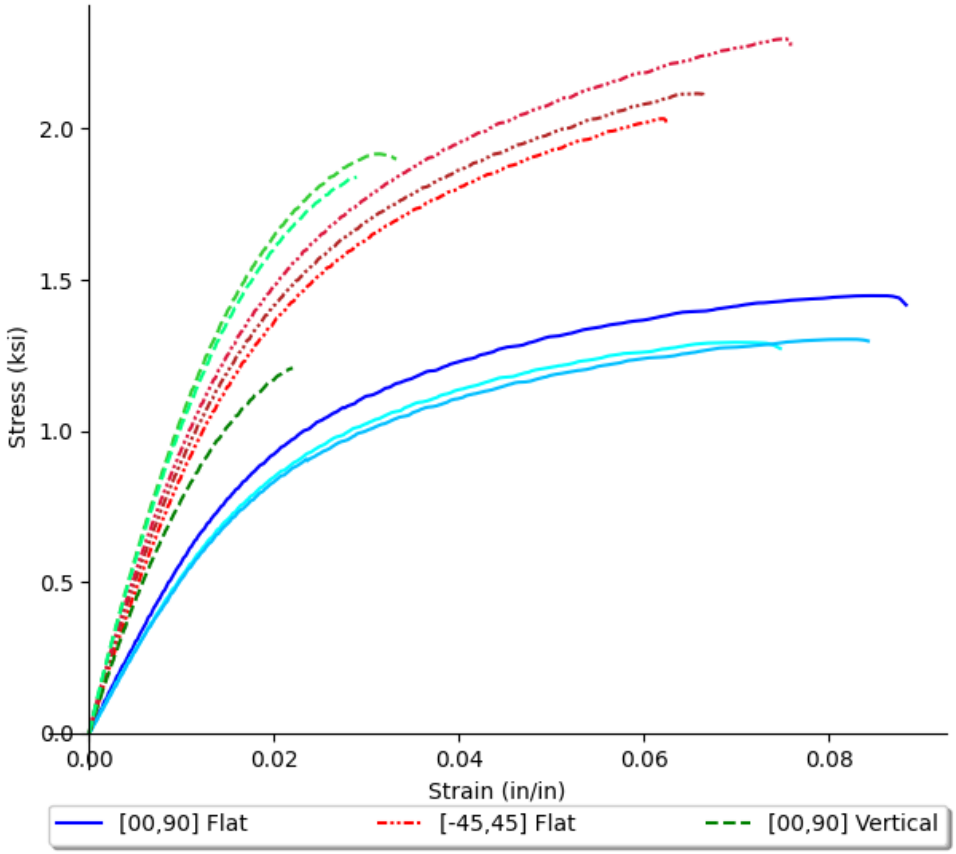

FIGURE 2.9: FR-106 pristine tension stress vs strain curves

The FR-106 material was tested in bending using the standard bending coupons (see Appendix B). The results of the pristine bending testing are shown in Figure 2.10 and Table 2.2. Due to the brittle behavior of the tension tests, the rate of straining of the outer fiber was 0.01 mm/mm/min for the FR-106 bending tests.

Print Orientation	Test Modulus (ksi)	Specified Modulus (ksi)	Test Ult. Stress (ksi)	Specified Ult. Stress (ksi)	Test Break Strain (%)	Specified Break Strain (%)
[00,90] Flat	57	202	1.3	6.7	8.2	38.0
[-45,+45] Flat	107	202	2.1	6.7	6.8	38.0
[00,90] Vertical	110	202	1.7	6.7	2.8	38.0

TABLE 2.1: FR-106 average pristine tension results

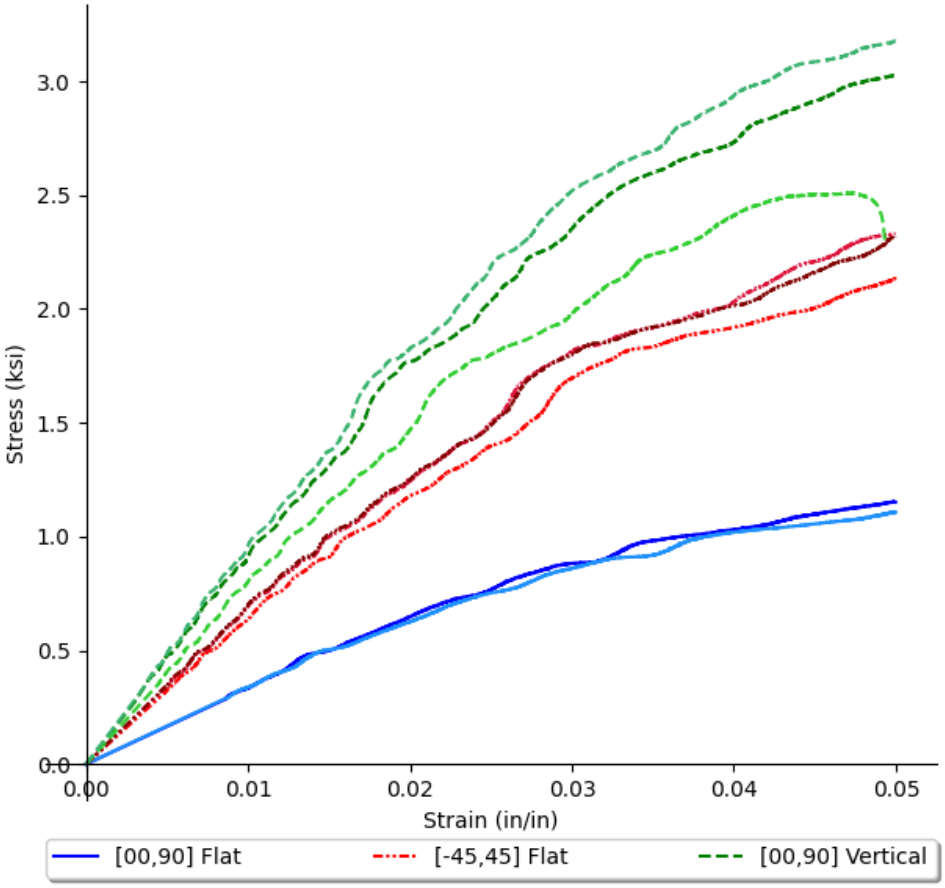

FIGURE 2.10: FR-106 pristine bending stress vs strain curves

This material demonstrated anisotropic behavior which is atypical of an SLS printed material. Additionally, the coupons performed poorly when compared to reported

Print Orientation	Test Modulus (ksi)	Specified Modulus (ksi)	Test Ult. Stress (ksi)	Specified Ult. Stress (ksi)
[00,90] Flat	33	195	1.1	N/A
[-45,+45] Flat	67	195	2.3	N/A
[00,90] Vertical	88	195	2.9	N/A

TABLE 2.2: FR-106 average pristine bending results

data from the material supplier [*FR-106 - Material Specifications*]. Due to the poor performance of these coupons, no further testing was done on this material, and it would not be a candidate for the final material selection (see Chapter 4).

2.3.2 HT-23 (SLS Printing) Test Results

The HT-23 material was tested in tension using Type I tension coupons (see Appendix A). The results of the pristine tension testing are shown in Figure 2.11 and Table 2.3.

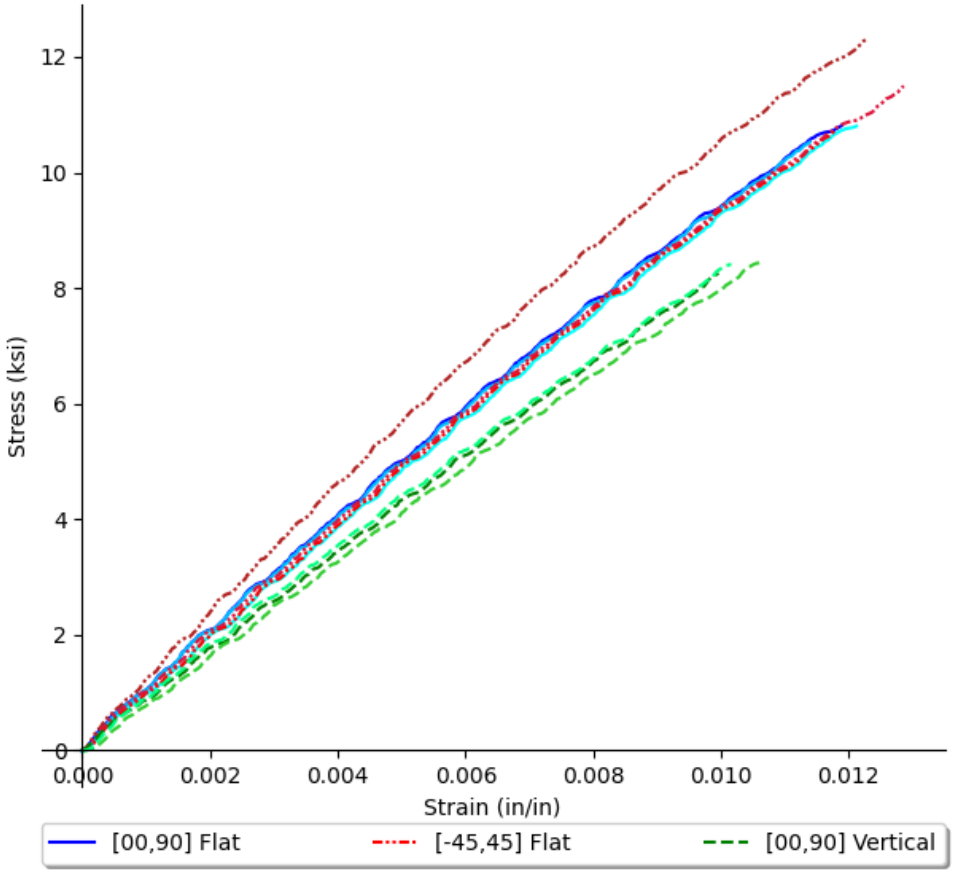

FIGURE 2.11: HT-23 pristine tension stress vs strain curves

Print Orientation	Test Modulus (ksi)	Specified Modulus (ksi)	Test Ult. Stress (ksi)	Specified Ult. Stress (ksi)	Test Break Strain (%)	Specified Break Strain (%)
[00,90] Flat	1005	943	10.7	10.3	1.2	1.3
[-45,+45] Flat	1042	943	11.5	10.3	1.2	1.3
[00,90] Vertical	862	841	8.4	8.6	1.0	1.1

TABLE 2.3: HT-23 average pristine tension results

The HT-23 material was tested in bending using the standard bending coupons (see Appendix B). The rate of straining of the outer fiber was 0.01 mm/mm/min for HT-23 bending tests. The results of the pristine bending testing are shown in Figure 2.12 and Table 2.4.

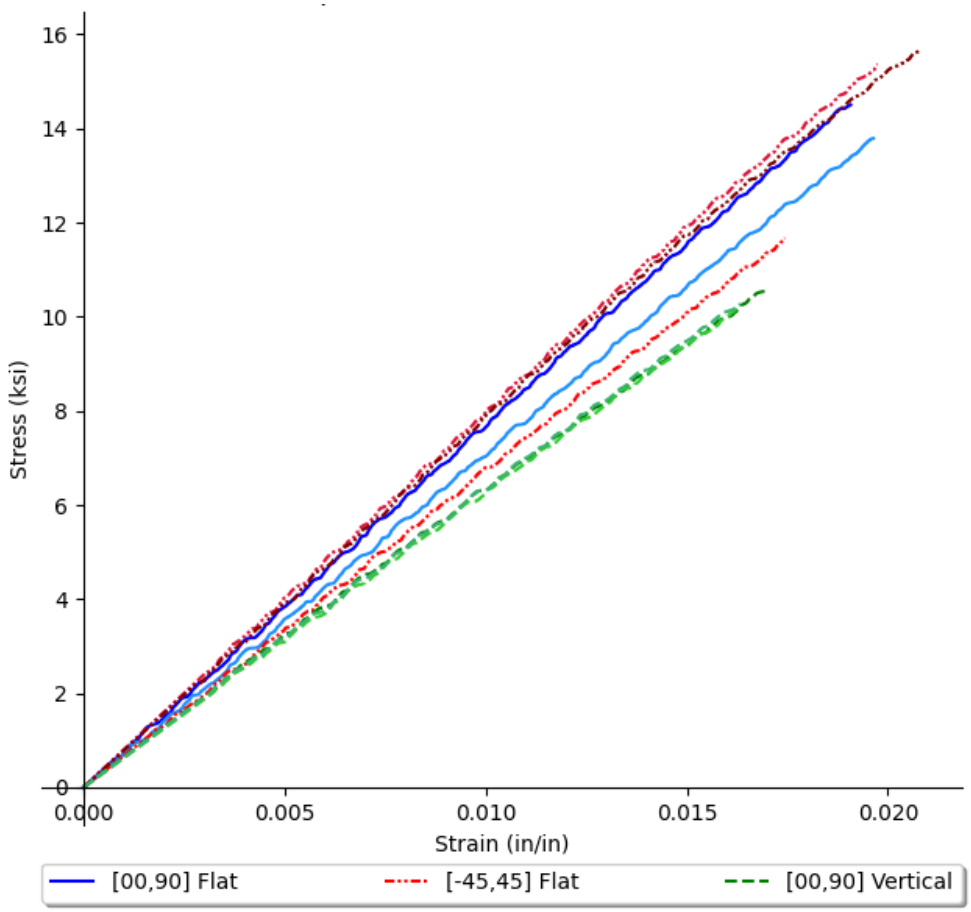

FIGURE 2.12: HT-23 pristine bending stress vs strain curves

Print Orientation	Test Modulus (ksi)	Specified Modulus (ksi)	Test Ult. Stress (ksi)	Specified Ult. Stress (ksi)	Test Break Strain (%)	Specified Break Strain (%)
[00,90] Flat	778	886	14.7	14.6	1.9	N/A
[-45,+45] Flat	753	866	14.2	14.6	1.9	N/A
[00,90] Vertical	634	744	10.4	11.7	1.7	N/A

TABLE 2.4: HT-23 average pristine bending results

The material showed isotropic behavior in the XY, or flat, plane with only a slight drop off in performance in the vertical direction, which was expected. The test data also closely matched the material specifications provided by the material supplier [*HT-23 - Material Specifications*]. While this material is stiff compared to the other materials considered for this project, it is also the most brittle. As seen in Figure 2.11, the material behaves linearly until failure with no apparent ductile response before failure. The brittleness of the material can also be seen by examining the tested coupons (see Figure 2.13).

FIGURE 2.13: HT-23 broken tension coupon

It can be seen that the coupon does not have a distinct failure location. Rather, the coupon breaks in multiple locations due to the brittleness.

After the pristine characterization of the coupons was completed, the next step was to then subject the material to temperature degradation. Three coupons were subjected to 20 temperature cycles from -49 to 203 degrees Fahrenheit. Then three coupons were subjected to 20 temperature cycles from -49 to 0 degrees Fahrenheit, and three coupons were subjected to 20 temperature cycles from 0 to 203 degrees Fahrenheit. The coupons were then brought to room temperature and tested in tension. All of the coupons subjected to environmental degradation were [00,90] flat coupons. The results of the tension tests on these coupons are shown in Figure 2.14 and Table 2.5.

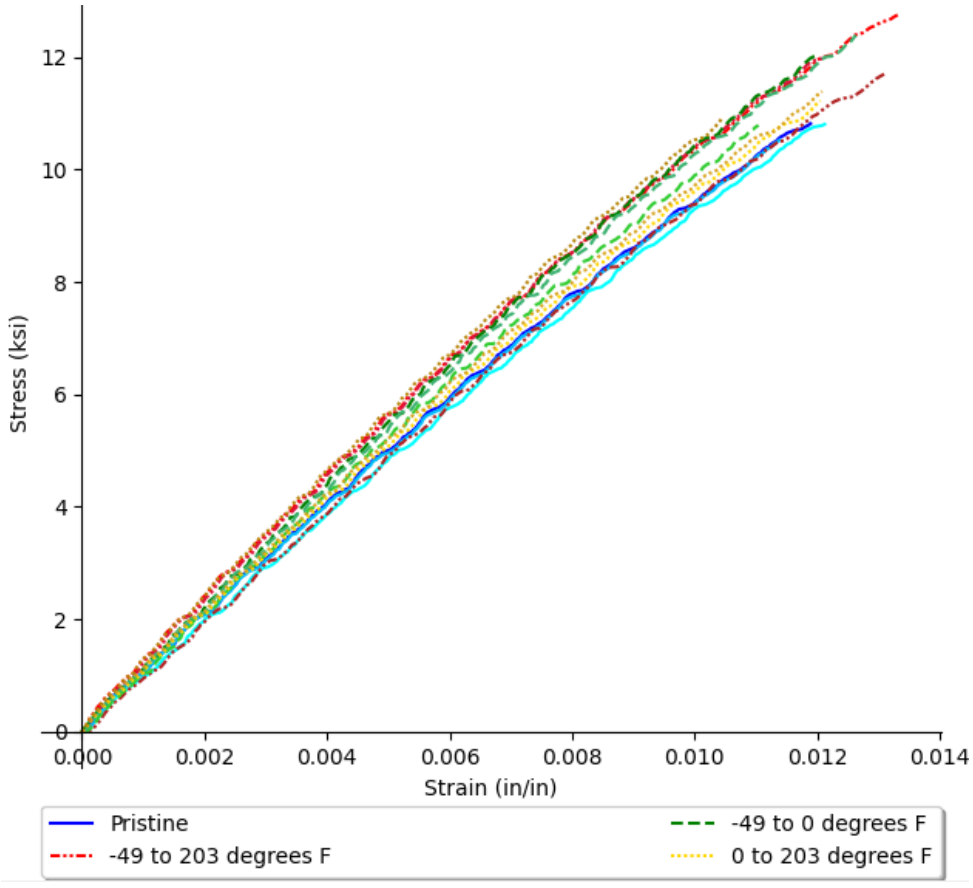

FIGURE 2.14: HT-23 environmental tension stress vs strain curves

The material showed no significant change in performance when subjected to the temperature cycles described above. Additional testing was performed on this material to

Coupon Type	Modulus (ksi)	Ult. Stress (ksi)	Break Strain (%)
Pristine	1005	10.7	1.18
-49°F to 203°F	1099	12.2	1.29
0°F to 203°F	1088	11.2	1.15
-49°F to 0°F	1089	11.7	1.19

TABLE 2.5: HT-23 average environmental tension results

determine its yield point, or lack of one, through cyclic loading (see Chapter 3). Due to its high stiffness and strength, this material was one of the materials chosen for the final material recommendations (see Chapter 4).

2.3.3 Onyx (FFF Printing) Test Results

The Onyx material was tested in tension using Type I tension coupons (see Appendix A). The results of the pristine tension testing are shown in Figure 2.15 and Table 2.6. The specified values presented in Table 2.6 are values from the material supplier [*Material Datasheet - Composites* 2020].

Print Orientation	Test Modulus (ksi)	Specified Modulus (ksi)	Test Ult. Stress (ksi)	Specified Ult. Stress (ksi)	Test Break Strain (%)	Specified Break Strain (%)
[00,90] Flat	328	348	5.6	5.8	14.9	25.0
[-45,+45] Flat	186	348	5.6	5.8	38.2	25.0
[00,90] Vertical	174	348	3.2	5.8	5.4	25.0
[-45,+45] Vertical	167	348	3.0	5.8	4.1	25.0

TABLE 2.6: Onyx average pristine tension results

The Onyx material was tested in bending using the standard bending coupons (see Appendix B). The rate of straining of the outer fiber was 0.01 mm/mm/min for one of the [00,90] flat coupons, but it did not fail before the end of test was reached. Due to this, the rate of straining was increased to 0.10 mm/mm/min for the remaining flat

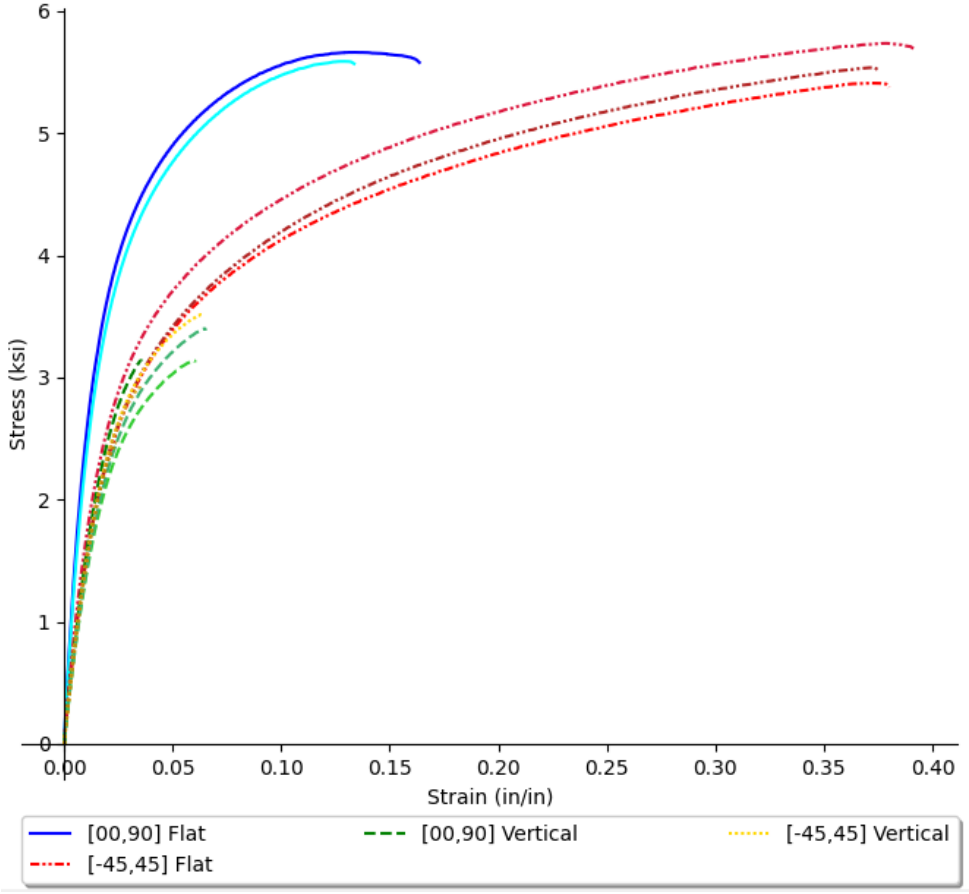

FIGURE 2.15: Onyx pristine tension stress vs strain curves

coupons. Since vertical prints are much more brittle for FFF printing, it was thought that the vertical bending coupons may break before the end of test strain limit. For this reason, the vertical bending coupons were tested at a strain rate of 0.01 mm/mm/min. The results of the pristine bending testing are shown in Figure 2.16 and Table 2.7. The specified values presented in Table 2.7 are values from the material supplier [*Material Datasheet - Composites* 2020].

Print Orientation	Test Modulus (ksi)	Specified Modulus (ksi)	Test Ult. Stress (ksi)	Specified Ult. Stress (ksi)
[00,90] Flat	123	435	4.9	10.3
[-45,+45] Flat	83	435	3.5	10.3
Vertical	96	435	3.6	10.3

TABLE 2.7: Onyx average pristine bending results

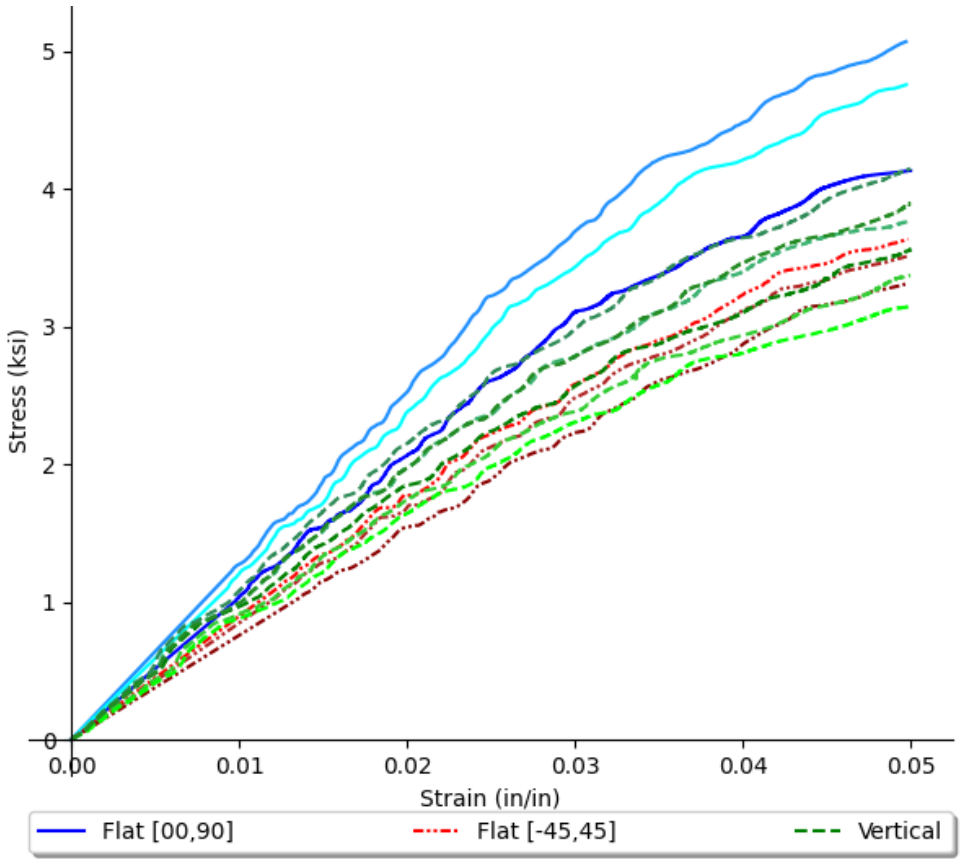

FIGURE 2.16: Onyx pristine bending stress vs strain curves

The material demonstrated anisotropic behavior between the flat and vertical print orientations as well as between the two different raster angles for the flat printed coupons. This was to be expected as this behavior is typical of FFF 3D printed parts (see Subsection 2.2.2).

The next step after characterizing the pristine behavior was to subject the material to environmental degradation. Four sets of coupons were tested in tension and compared to characterize the degradation from thermal cycling: a set of pristine coupons, a set that was placed at -49°F for 24 hours, a set that was cycled from -49°F to 68°F 5 times, and a set that was cycled from -49°F to 68°F 15 times. These four sets of coupons were printed flat with a raster angle of [-45,+45]. The results of this testing can be seen in Figure 2.17 and Table 2.8.

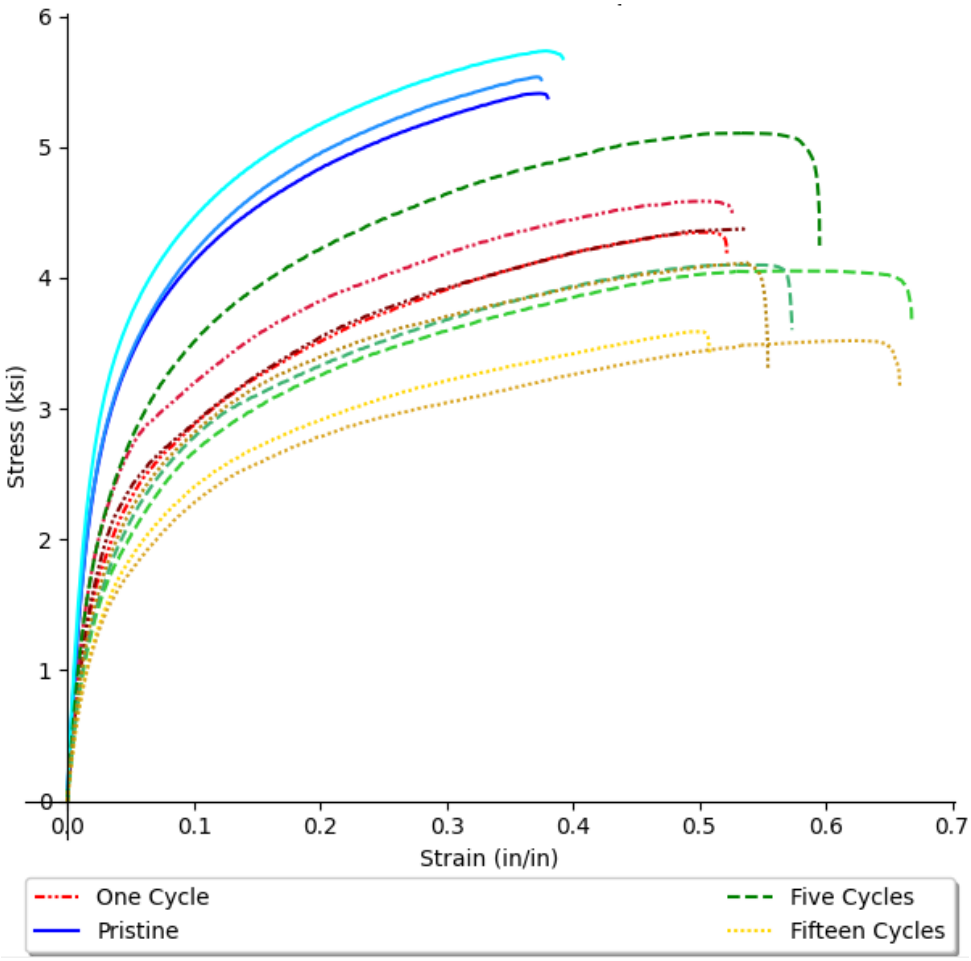

FIGURE 2.17: Onyx environmental coupons tension stress vs strain curves

Coupon Type	Modulus (ksi)	Ult. Stress (ksi)	Break Strain (%)
Pristine	186	5.6	38.2
1 Cycle	112	4.4	52.8
5 Cycles	102	4.4	61.2
15 Cycles	82	3.7	57.4

TABLE 2.8: Onyx average environmental testing results

From the test results, Onyx appears to be affected significantly in its performance when subjected to the temperature ranges stated above. At the point in the project when the environmental testing was being performed on the Onyx material, it had already been determined that Onyx would not be a candidate for the final material selection (see Chapter 4) due to the low yield stress value seen in testing (see Chapter 3). Due to this, no further environmental studies were performed on the Onyx material. For more

studies conducted on the Onyx material exploring different coupon sizes and types, see Chapter 3.

2.3.4 Onyx with Continuous Carbon Fiber (FFF Printing) Test Results

The Onyx with continuous carbon fiber was tested in tension using Type I tension coupons (see Appendix A). The results of the pristine tension testing are shown in Figure 2.19 and Table 2.9. The data shown for these coupons was calculated using the gross area of the entire coupon, which includes the contribution from the Onyx matrix and the carbon fiber reinforcement. Coupons of various raster orientations for the matrix and fiber were tested; however, all of the coupons had two concentric fiber rings along the perimeter. This means that the carbon fiber nozzle in the printer made two passes that follow the shape of the perimeter of the coupon. The two concentric fiber rings can be seen in Figure 2.18 in which the carbon fiber filament is shown in blue. The coupon shown in Figure 2.18 has a matrix raster of [-45,+45] and a fiber raster of [00,45,90,135]. This figure is taken from the Markforged slicer software, Eiger, which shows an internal view of the coupon with the fiber filaments highlighted in blue.

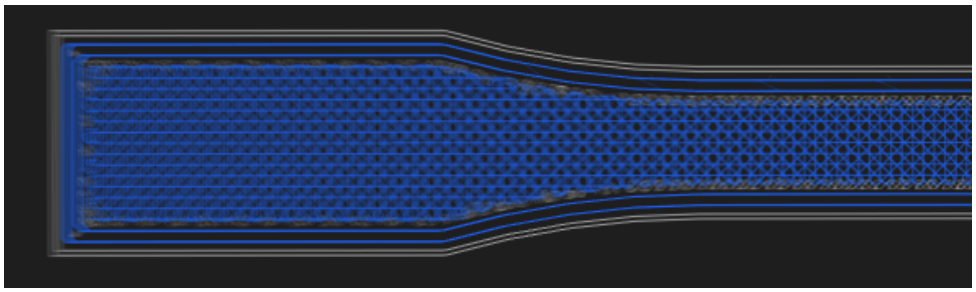

FIGURE 2.18: Onyx with continuous carbon fiber filament placement, fiber filaments shown in blue

All the coupons tested with continuous carbon fiber were printed in the flat orientation. Due to the linear behavior of the coupons, the moduli presented for the Onyx with

continuous carbon fiber reinforcing are determined using a linear regression of all the data points during the loading.

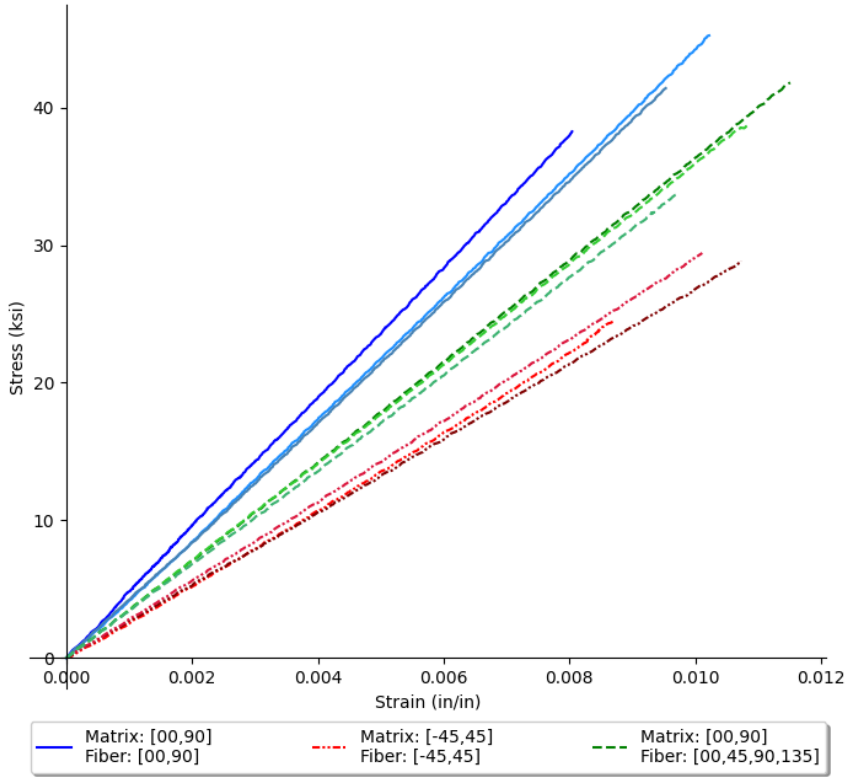

FIGURE 2.19: Onyx with continuous carbon fiber pristine tension stress vs strain curves

Matrix Orientation	Fiber Orientation	Modulus (ksi)	Ult. Stress (ksi)	Break Strain (%)
[00,90]	[00,90]	4514	42	0.93
[-45,+45]	[-45,+45]	2814	28	0.99
[00,90]	[00,45,90,135]	3583	38	1.07

TABLE 2.9: Onyx with continuous carbon fiber average pristine tension results

These coupons behaved similarly to other carbon fiber reinforced composites documented in literature [Al-Qrimli, Mahdi, and Ismail, 2015]. The material behaves almost linearly until a brittle failure. As can be seen in Figure 2.20, the coupon did not break entirely at failure. Instead, a few of the reinforcing carbon fibers break and the Onyx matrix separates, but the coupon can still carry a reduced load through the remaining fibers.

FIGURE 2.20: Onyx with continuous carbon fiber coupon after test

These coupons were also tested with temperature cycling. Three coupons were tested in the pristine state, and three coupons were subjected to 20 temperature cycles from -49 to 203 degrees Fahrenheit. These six coupons were all printed in with a matrix raster of [-45,+45] and a fiber raster of [00,45,90,135]. The results of this testing are shown in Figure 2.21 and Table 2.10.

Coupon Type	Modulus (ksi)	Ult. Stress (ksi)	Break Strain (%)
Pristine	3679	46.2	1.26
Environmental	4020	46.8	1.16

TABLE 2.10: Onyx with continuous carbon fiber average environmental tension results

From the temperature cycling testing results, it can be seen that there is a change in the loading modulus between the pristine and environmental coupons; however, it does not appear that temperature cycling has a detrimental impact on the behavior of these coupons, which are dominated by the carbon fiber reinforcing.

Chapter 3 discusses the results of a study to determine if this material demonstrated any yielding after repeated loading cycles. While this material is the stiffest and strongest of all the materials tested, using continuous carbon fiber reinforcing reduces the allowed print complexity. Additionally, the matrix material, Onyx, was already shown to degrade under thermal cycling. Even though the fiber is providing strength to overcome that for the few cycles that were run, it is a concern. Due to this, it was determined that this material would not be a candidate for the final material recommendation (see Chapter 4).

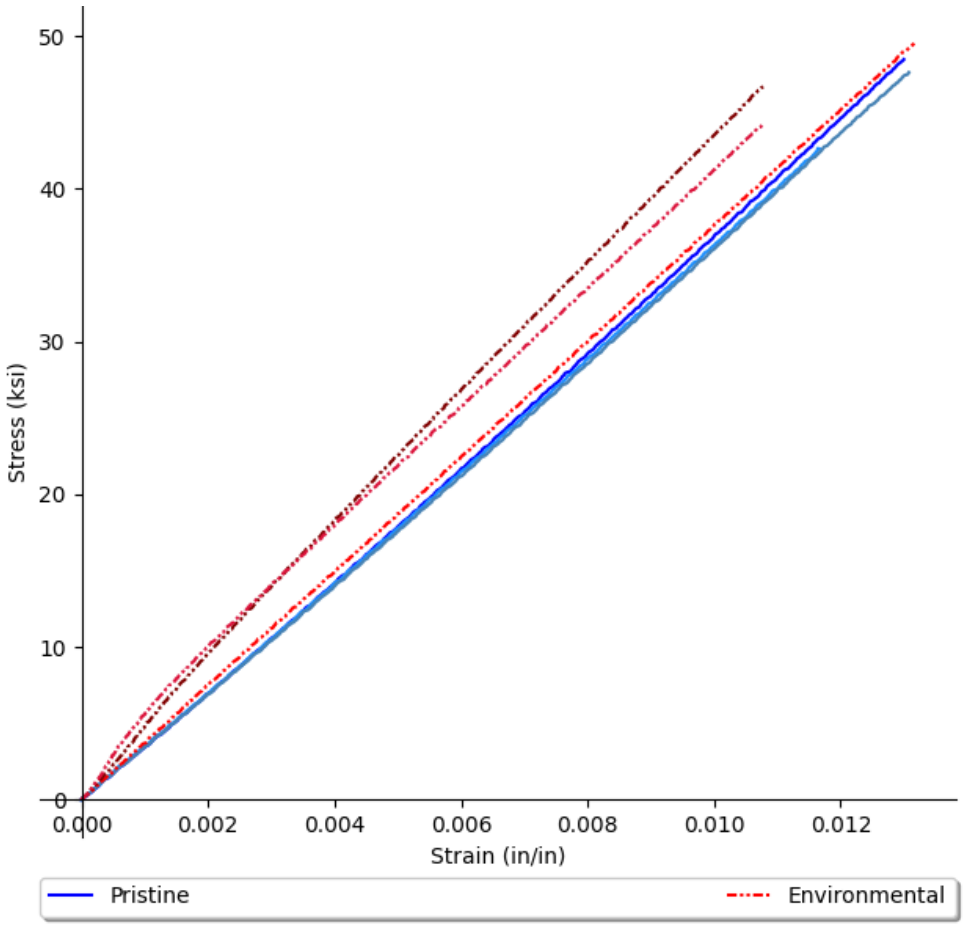

FIGURE 2.21: Onyx with continuous carbon fiber environmental coupon tension stress vs strain curves

2.3.5 ThermaX PEEK (FFF Printing) Test Results

The ThermaX PEEK material was tested in tension using Type I tension coupons (see Appendix A). The results of the pristine tension testing are shown in Figure 2.22 and Table 2.11.

The ThermaX PEEK material was tested in bending using the standard bending coupons (see Appendix B). Only one print orientation and raster angle was tested for ThermaX PEEK in bending. This was due to the limited amount of printer availability and the need for more tensile coupons. The print orientation selected was flat with a raster angle of [-45,+45]. The strain rate of the outer fiber was 0.01 mm/mm/min for the first coupon test. The first coupon did not break before the end of test strain limit was

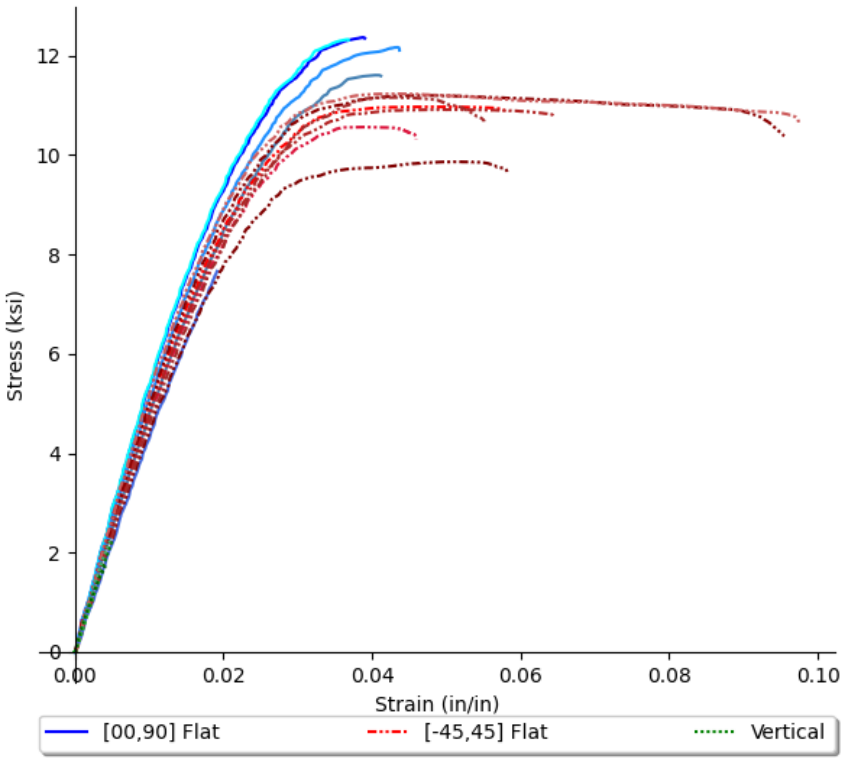

FIGURE 2.22: ThermaX PEEK pristine tension stress vs strain curves

reached. Due to this, the rest of the coupons were tested with a strain rate of 0.10 mm/mm/min. The results of the pristine bending testing are shown in Figure 2.23 and Table 2.12.

The material demonstrated anisotropic behavior between the flat and vertical print orientations as well as between the two different raster angles for the flat printed coupons. This was to be expected as it is typical of FFF 3D printed parts (see Subsection 2.2.2). The stiffness and strength of the coupons also closely matched the supplier values for strength and stiffness of the flat prints [*Technical Data Sheet: ThermaX™ PEEK 3D Printing Filament* 2021].

The next step after characterizing the pristine behavior was to subject the material to degradation from temperature cycling. Due to limited printer availability, the Type V Tensile Coupons (see Appendix A) were used for the environmental characterization of ThermaX PEEK. Three coupons were not subject to any temperature cycles, and three

Print Orientation	Test Modulus (ksi)	Supplier Modulus (ksi)	Test Ult. Stress (ksi)	Supplier Ult. Stress	Test Break Strain (%)	Supplier Break Strain (%)
[00,90] Flat	550	540	12.1	14.5	4.02	28.0
[-45,+45] Flat	505	540	10.8	14.5	6.78	28.0
Vertical	459	540	1.95	14.5	0.43	28.0

TABLE 2.11: ThermaX PEEK average pristine tension results

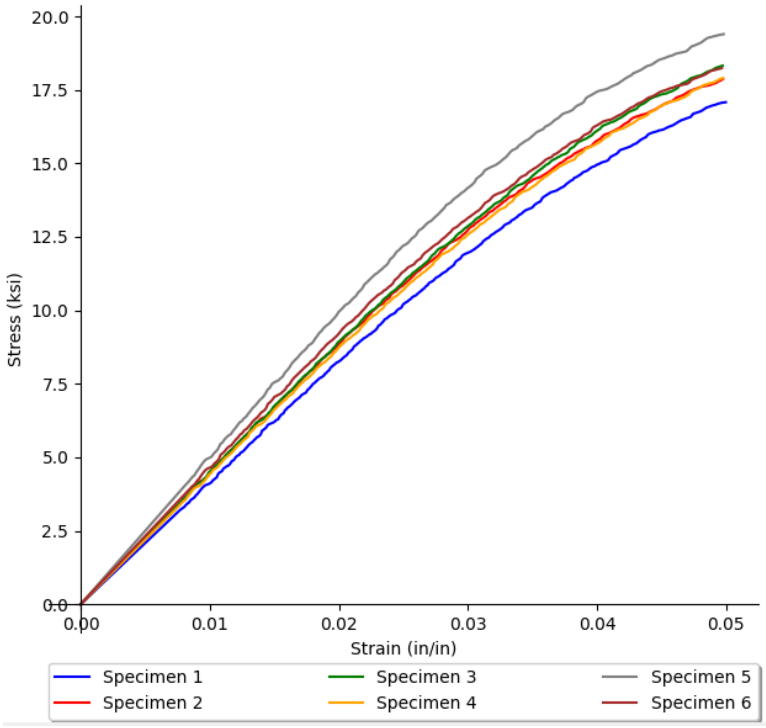

FIGURE 2.23: ThermaX PEEK pristine bending stress vs strain curves

coupons were subjected to 20 temperature cycles from -49 to 203 degrees Fahrenheit. Then three coupons were subjected to 20 temperature cycles from -49 to 0 degrees Fahrenheit, and three coupons were subjected to 20 temperature cycles from 0 to 203 degrees Fahrenheit. The coupons were then brought to room temperature and tested in tension. All of the coupons subjected to the degradation from temperature cycling were [-45,+45] flat coupons. The results of the tension tests on these coupons are shown in Figure 2.24 and Table 2.13.

Print Orientation	Test Modulus (ksi)	Specified Modulus (ksi)	Test Ult. Stress (ksi)	Specified Ult. Stress (ksi)
[-45,45] Flat	453	392	18.1	18.9

TABLE 2.12: ThermaX PEEK average pristine bending results

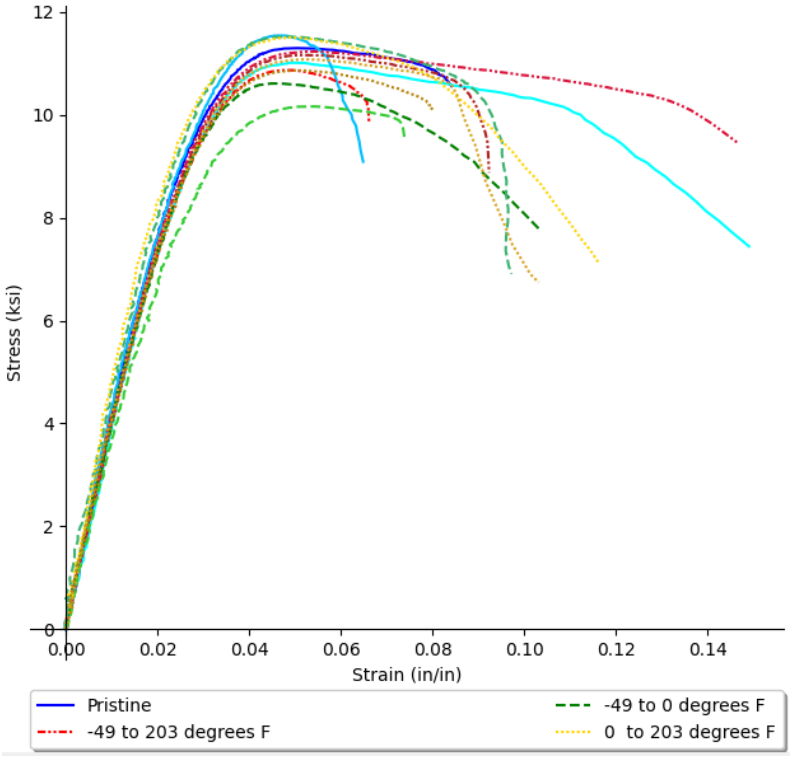

FIGURE 2.24: ThermaX PEEK environmental tension stress vs strain curves

Coupon Type	Modulus (ksi)	Ult. Stress (ksi)	Break Strain (%)
Pristine	406	11.3	9.93
-49°F to 203°F	406	11.1	10.2
0°F to 203°F	426	11.1	9.98
-49°F to 0°F	409	10.8	9.15

TABLE 2.13: ThermaX PEEK average environmental tension results

The material showed no significant change in performance when subjected to the temperature cycles described above. Additional testing was performed on this material to determine its yield point and to investigate the effect of different coupon shapes on

performance (see Chapter 3). Due to its high stiffness and strength, this material was one of the materials chosen for the final material recommendations (see Chapter 4).

3 Special Considerations and Testing Protocols

3.1 Overview

Test results for 3D printed polymers are more variable and parameter sensitive than older manufacturing methods. During testing, several special protocols were developed to address issues that arose. These protocols were (i) a method of determining the yield point of the material systems; (ii) a method for producing successful vertically printed parts; (iii) a method of determining the size effects present in 3D printing of polymers; (iv) and a method of determining the bond strength with varying layer times for FFF printing. The results from these protocols are discussed in the following sections.

3.2 Yield Identification

Many of the materials tested in this project displayed nearly immediate (from the onset of loading) nonlinear stress-strain curves with no clear yield point. For metals that are often used in structural design, such as heat-treated steel or aluminum, it is common to use the 0.2 percent offset method to determine the yield point of the material [Ugural and Fenster, 2012]. While this arbitrary yield point created by the 0.2% offset method has proven to work well in design with these materials, it was unknown if this method would be reliable for the materials tested in this project. Due to this, cyclic tension tests

were run to determine at which stress level the loading modulus would deviate from the initial loading modulus and would cause permanent deformation to occur. The coupons in this section were loaded in cycles of increasing tension stress until failure. The yield stress range was taken as when the onset of permanent deformation and stiffness degradation occurred. The results of these tests are discussed in the following subsections.

3.2.1 FR-106 Yield Point Study

The pristine tension and bending coupons for FR-106 (see Section 2.3) behaved poorly when compared to material supplier data. Due to this poor performance and due to permanent deformation occurring almost immediately during the pristine testing of the material, no yield point study was conducted on this material.

3.2.2 HT-23 Yield Point Study

During the pristine characterization testing of HT-23, the material displayed predominately linear behavior until brittle failure. Since brittle materials often experience failure shortly after the end of the elastic region, it was expected that the material's loading modulus would not degrade until a stress level close to the failure stress was reached [MechaniCalc Inc., 2021]. Figure 3.1 shows the typical stress-strain curve for the flat HT-23 coupons tested by cyclic loading. The noise seen in this figure was also seen in many other tests performed with the same equipment. Table 3.1 shows the typical results of the loading moduli for the flat coupon shown in Figure 3.1 as well as the percent difference from the initial loading modulus. In Table 3.1, the loading moduli are denoted by E. The data points for the first cycle, from 0 ksi to 1.1 ksi, were too noisy to produce a reliable initial loading modulus; therefore, the loading modulus of the second cycle, from 0 ksi to 2.1 ksi, was taken as the initial loading modulus. The

moduli presented in Table 3.1 are calculated by taking a linear regression from 0 ksi to 2.1 ksi which was the peak stress of the second loading cycle.

Peak Stress (ksi)	2.1	3.2	4.3	5.4	6.4	7.5	8.6	9.7	10.7	11.8
E (ksi)	959	965	965	966	965	967	971	969	965	964
% Diff.	0.0	0.6	0.6	0.7	0.6	0.8	1.2	1.0	0.5	0.5

TABLE 3.1: HT-23 typical cyclic results

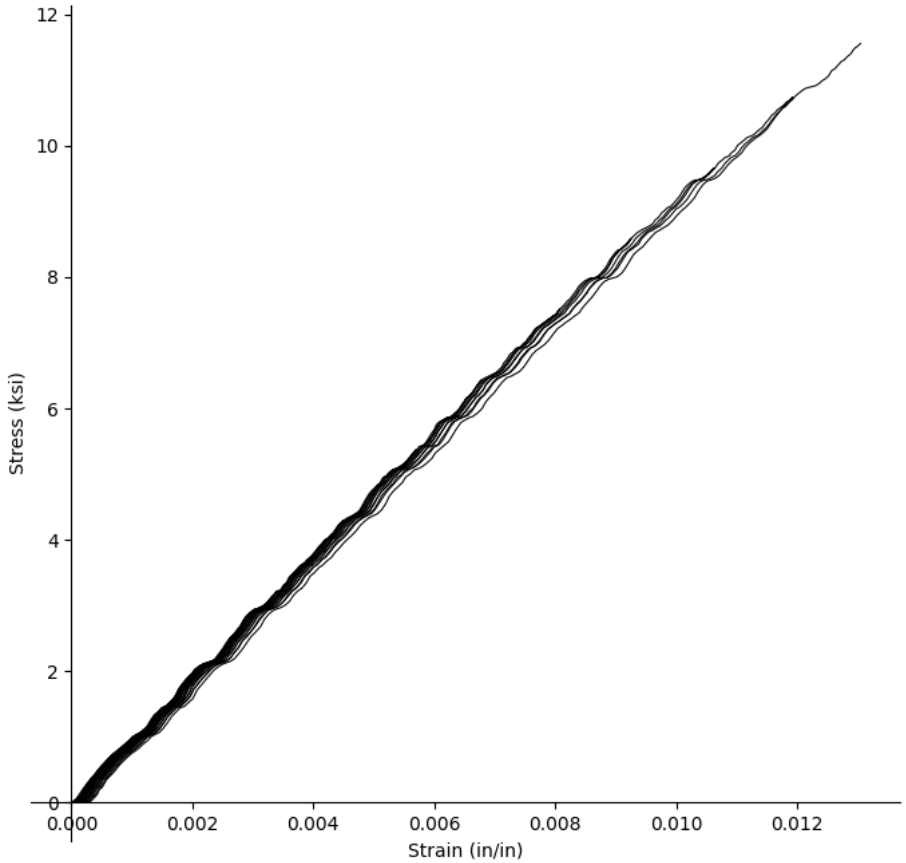

FIGURE 3.1: HT-23 typical cyclic stress vs strain curves

The results from Figure 3.1 and Table 3.1 show no significant deterioration of the stiffness as the load increases. The same cyclic tests were performed on vertically printed HT-23 coupons with similar results. This means that the material behaves mostly elastic until fracture. It is important to note that fatigue was not explored. Cyclic loading

near fracture would likely cause accumulated damage which was not a part of this study.

3.2.3 Onyx Yield Point Study

During the pristine characterization testing of Onyx, the material displayed non-linear behavior. The non-linear behavior of the material also showed no clear yield point between the transition from elastic to plastic behavior. Due to this, the material was subjected to cyclic loading to determine where this transition point was. Figure 3.2 and Table 3.2 show the results of this testing for a [00,90] flat specimen. In Table 3.2, the loading moduli are denoted by E. The cyclic stress-strain curves follow the backbone curve from the Onyx pristine testing. Due to this, the moduli were calculated by taking a line from 0 ksi to the previous cycle peak stress, which was a good representation of the moduli for each cycle. Since this could not be done for the first cycle, the first cycle modulus is an initial tangent modulus.

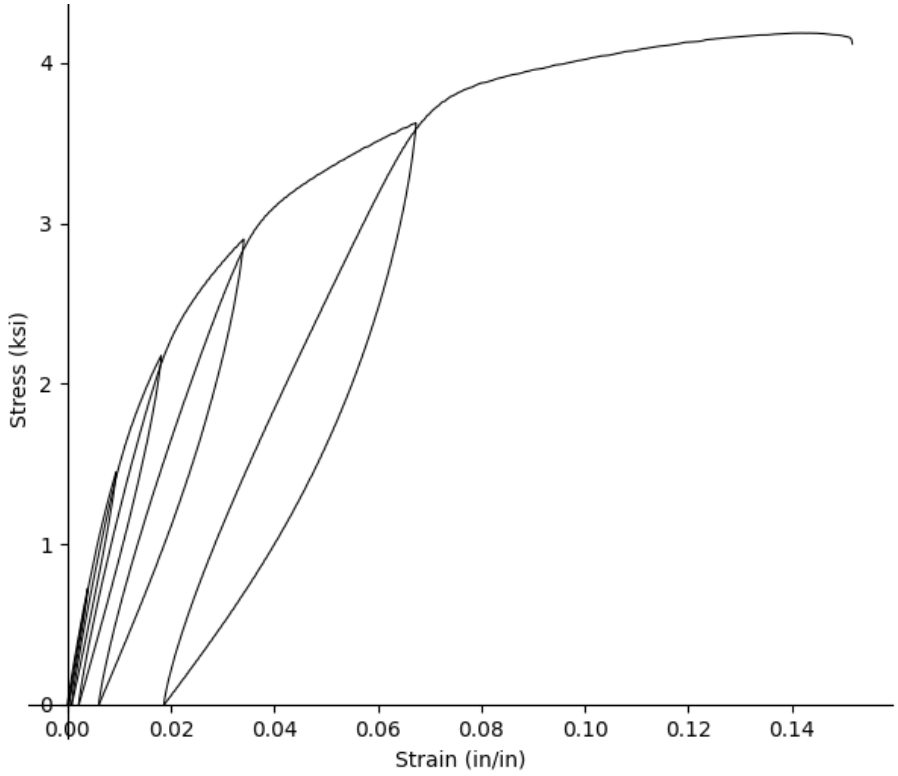

FIGURE 3.2: Onyx typical cyclic stress vs strain curves

Peak Stress (ksi)	0.73	1.45	2.18	2.90	3.63	4.35
E (ksi)	202	199	169	137	104	75
% Diff.	0.0	1.4	15.9	32.1	48.5	63.0

TABLE 3.2: Onyx typical cyclic results

The results of the testing show a rapid degradation in stiffness after the second cycle, which means the material becomes inelastic at a very low stress level. This was typical of all the coupons tested. Due to the low yield stress, it was decided that this material would not be suitable for the final material recommendations (see Chapter 4).

3.2.4 Onyx with Carbon Fiber Yield Point Study

During the pristine characterization testing of Onyx with continuous carbon fiber reinforcing, the coupons displayed predominately linear behavior until brittle failure. Similar to the HT-23 material, it was expected that the stiffness of these coupons would not degrade until a stress level close to the failure stress was reached. Figure 3.3 shows the typical stress-strain curve for the Onyx with continuous carbon fiber reinforcing coupons tested by cyclic loading. Table 3.3 shows the typical results of the loading moduli for the coupon shown in Figure 3.3 as well as the percent difference from the initial loading modulus. The coupons tested with cyclic loading for Onyx with continuous carbon fiber reinforcing had a matrix raster of [-45,+45] and a fiber raster of [00,45,90,135]. As discussed in Subsection 2.3.4, these coupons have two concentric rings of carbon fiber along the perimeter. In Table 3.3, the loading moduli are denoted by E. Due to the linear behavior of the coupons, the moduli presented for the Onyx with continuous carbon fiber reinforcing are determined using a linear regression of all the data points during the loading.

Peak Stress (ksi)	4.6	9.3	13.9	18.6	23.2	27.8	32.5	37.1	41.8	46.4
E (ksi)	3918	3925	3865	3850	3842	3842	3845	3858	3872	3888
% Diff.	0.0	0.2	1.4	1.8	1.9	1.9	1.9	1.5	1.2	0.8

TABLE 3.3: Onyx with continuous carbon fiber reinforcing typical cyclic results

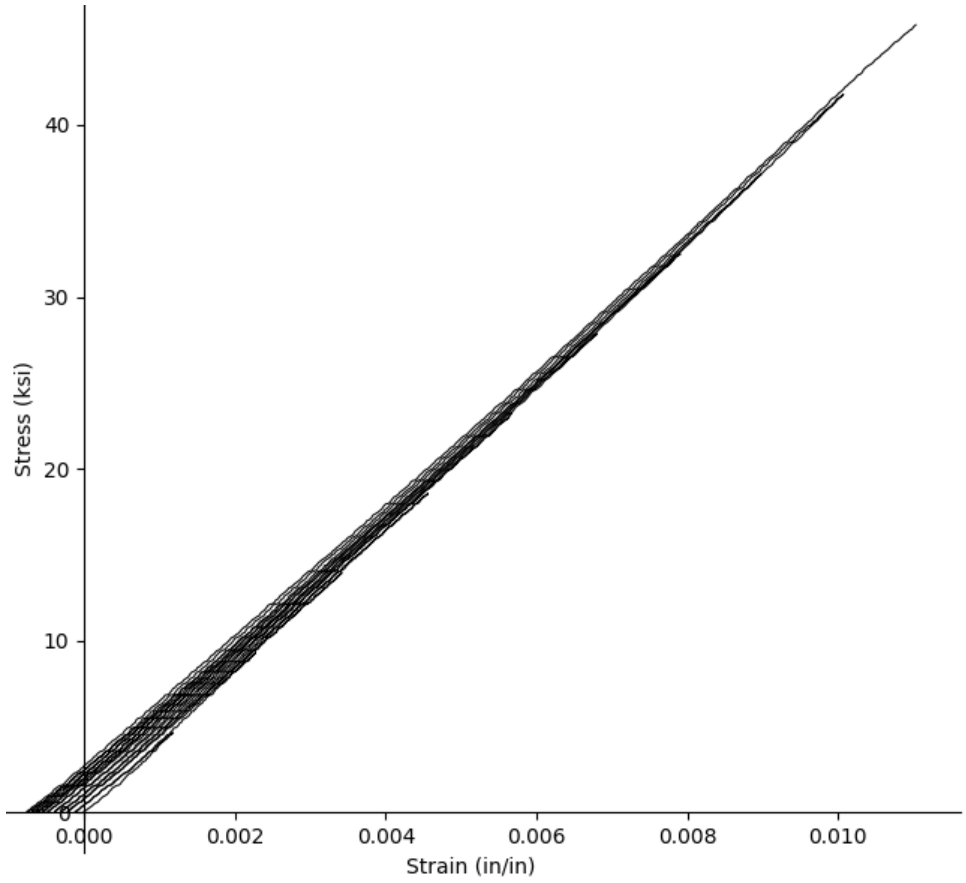

FIGURE 3.3: Onyx with continuous carbon fiber typical cyclic stress vs strain curves

The results from Figure 3.3 and Table 3.3 show no significant deterioration of the stiffness as the load increases. This means that these coupons behave mostly elastic until fracture.

3.2.5 ThermaX PEEK Yield Point Study

During the pristine testing of ThermaX PEEK, the stress vs strain curves showed an initial linear region followed by a transition into a non-linear region. As there was no clear transition point between the two, cyclic tension tests were run to determine when the transition between elastic and inelastic behavior occurs for this material. The typical results of this testing can be seen in Figure 3.4 and Table 3.4. In Table 3.4, the loading moduli are denoted by E. The data points for the first cycle, from 0 ksi to 1.2 ksi, were too noisy to produce a reliable initial loading modulus; therefore, the loading modulus of the second cycle, from 0 ksi to 2.3 ksi, was taken as the initial loading modulus. The moduli were calculated by taking a linear regression of the data points up to 2.3 ksi.

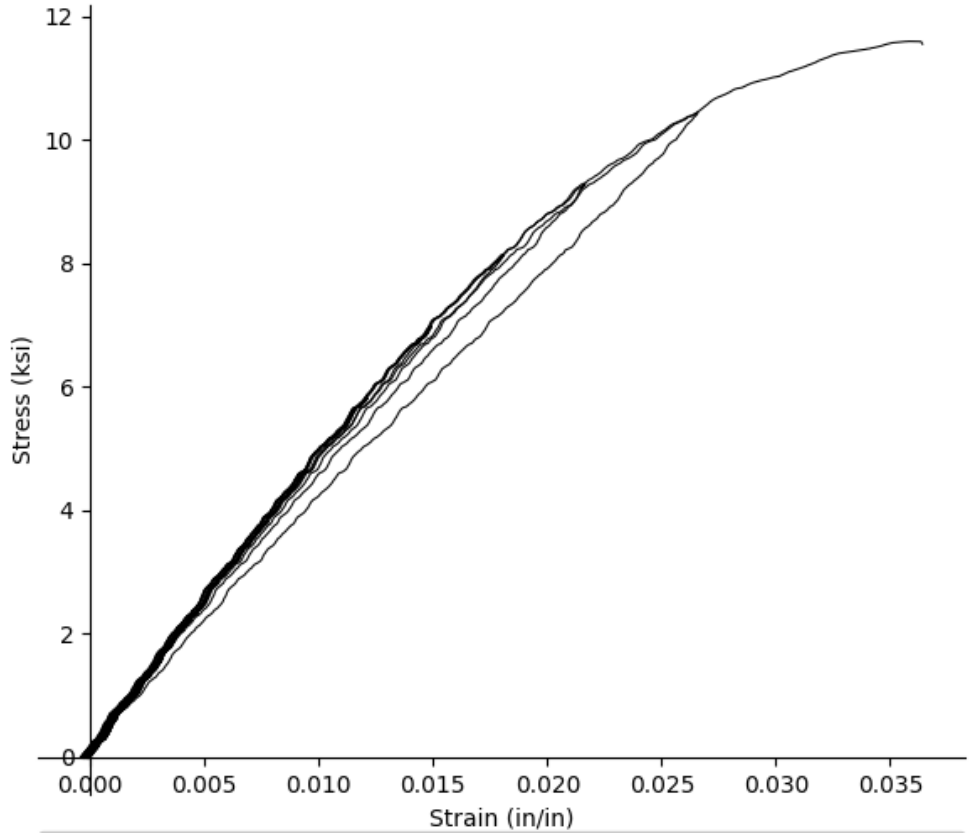

FIGURE 3.4: ThermaX PEEK typical cyclic stress vs strain curves

From the results in Figure 3.4 and Table 3.4 and from the results of the other coupons

Peak Stress (ksi)	2.3	3.5	4.6	5.8	7.0	8.1	9.3	10.4	11.6	12.8
E (ksi)	510	512	513	511	509	506	502	498	492	476
% Diff.	0.0	0.4	0.5	0.2	0.1	0.8	1.5	2.3	3.5	6.7

TABLE 3.4: ThermaX PEEK typical cyclic results

tested, it can be seen that the modulus begins to deviate between 9.3 to 10.4 ksi. This is approximately 80% to 90% of the ultimate stress for these coupons. This is useful guidance, as permanent deformation should be avoided under service loads.

3.3 Vertical Printing

During the testing of this project, vertically printed coupons were needed to help capture the behavior of FFF printed parts loaded primarily in the vertical direction. While printing these coupons for both Onyx and ThermaX PEEK, it was found difficult to successfully finish printing any coupons. This was only a problem for the materials that use FFF printing. This is because, unlike with SLS printing, FFF vertically printed coupons are unsupported during the printing process. Figure 3.5 shows an image of typical vertically printed coupons with Onyx that failed to finish.

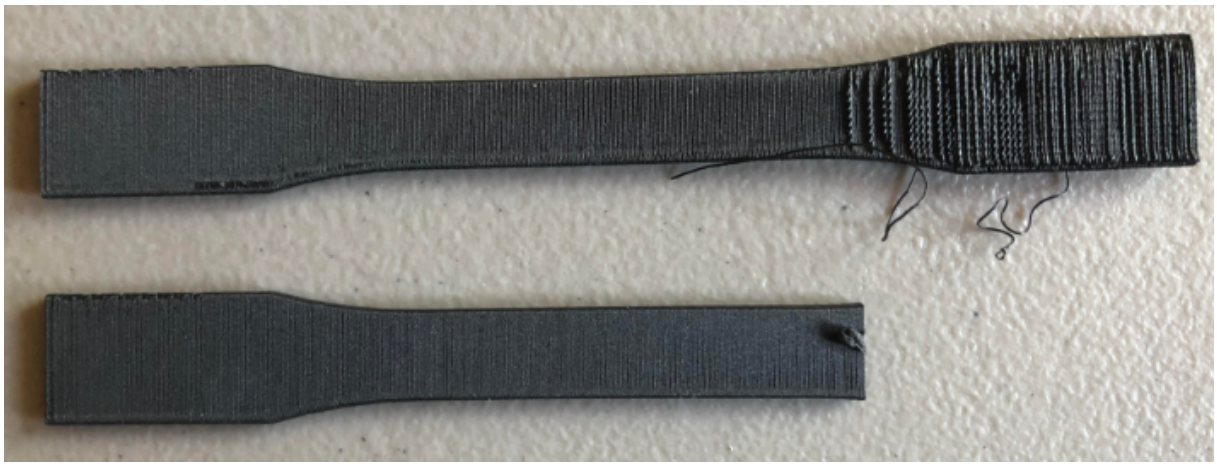

FIGURE 3.5: Typical failed vertical prints with Onyx

For the coupon on the top of Figure 3.5, the nozzle was able to place the filament correctly until about 75% of the way up the coupon. After that point, however, the coupon was not stiff enough to support itself, and as the nozzle began to place more material, the coupon would bend. This would cause the nozzle to place material in the wrong location. For the coupon on the bottom of the figure, once the coupon was too tall to support itself, the nozzle failed to place material in the correct location and the print failed at that point. This was the typical result of trying to print vertical coupons with Onyx. Either the coupons were complete with low quality at one end, or the coupons were simply incomplete. In order to successfully print vertical coupons, structural supports were added to the coupons during the printing process.

During the printing process of a coupon or part, the section of the part that has already been printing is cooling as more material is being placed by the nozzle. Due to the fact that the already printed section is still cooling, it has significantly less stiffness than the resulting part would have. This reduced stiffness becomes a problem for thin, vertically printed parts. With thin vertically printed parts, the part is often not stiff enough to support itself as the nozzle places more material. Due to this, structural supports are required for additional stiffness. The structural supports are good for the following reasons: (i) they add stiffness to the part; (ii) they increase the layer time of the part which gives the already printed material more time to cool before more material is placed above. While this additional cooling time can reduce the bond strength between layers, it does give the part a higher stiffness during the print. Figure 3.6 shows the different shapes that were considered for the structural supports.

From Figure 3.6 it can be seen that T section supports and triangular section supports of varying sizes were the two options used for the structural supports. These two shapes were ideal options for a structural support because they allow for minimal contact between the support and the coupon itself. The minimal contact between the support and the coupon allows for the support to be broken off with a low chance of damaging

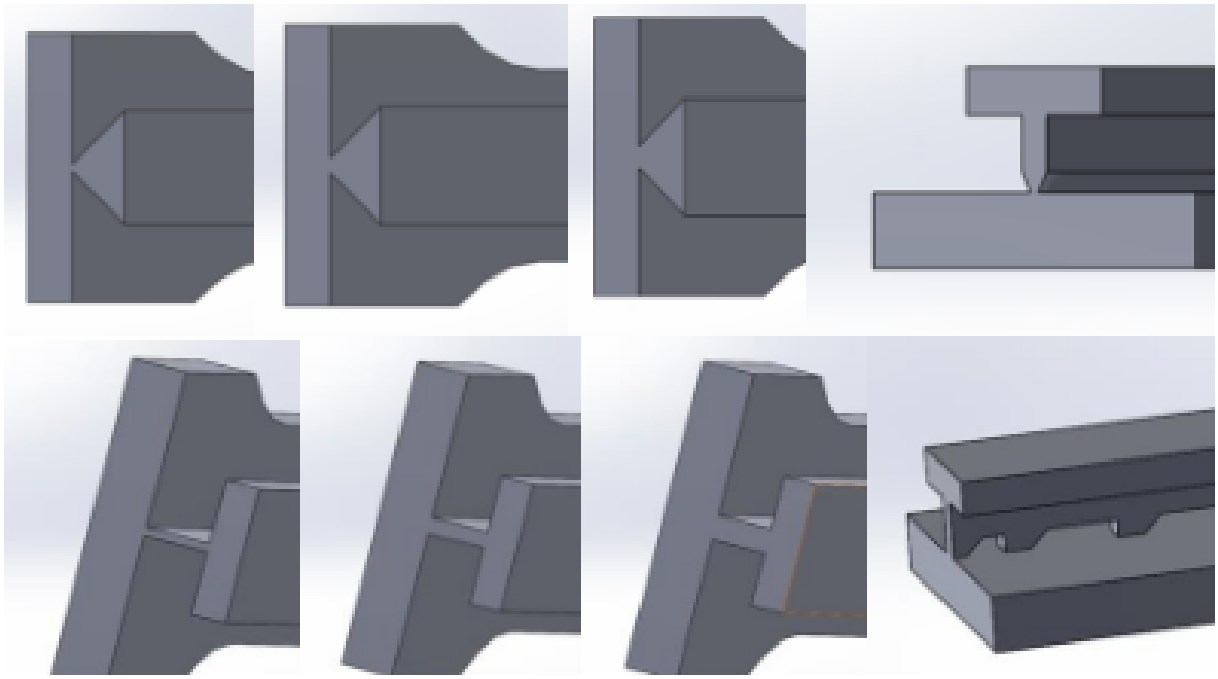

FIGURE 3.6: Structural support options

the coupon. By printing coupons with both types of structural supports, it was determined that the triangular support produced higher quality coupons than the T section support. An additional benefit of the triangular supports is that it allows for multiple coupons to be printed together for additional support as seen in Figure 3.7.

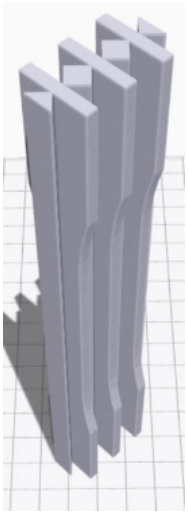

FIGURE 3.7: Vertical coupons printed together

While printing more coupons in the print bed at the same time could result in lower

performance of the coupons due to a lower bond strength due to a longer layer time, it does give the coupons more support during the printing process. This added support leads to higher quality coupons.

More vertical prints were performed on Onyx to try to find the best option for the thermal supports before trying to use them on the ThermaX PEEK material. This is because the ThermaX PEEK material is more difficult to print and requires more labor if a print is failed. This made it ideal to use the cheaper and more accessible Onyx material to determine what thermal supports should be used on the ThermaX PEEK vertical coupons. After more vertical coupon prints with Onyx were complete, it was determined that the best option for the thermal supports would be two triangular supports on each side of the coupon. This can be seen in Figure 3.17 in Section 3.5.

When the vertical coupon printing for the ThermaX PEEK material began, the coupons still failed to print even while using vertical supports which proved successful for the Onyx material. The nozzle of the printer would struggle to successfully place additional material on the new layers without causing a print failure. This is in part due to the fact the ThermaX PEEK needs to be printed at a higher temperature than Onyx. The higher temperature required to print ThermaX PEEK causes the layers to need more time to cool before they are stable enough to place another layer on top of them. In the end, it would take a large amount of trial and error with changing the print settings to produce completed coupons. Figure 3.8 shows one of the successful vertically printed ThermaX PEEK Type I Coupons.

While the surface finish of the successful vertical coupons was low, they were still able to be tested. Due to the low print quality and the significantly reduced strength (see Section 2.3) of vertically printed coupons, it is advised to avoid printing slender parts vertically on the print bed for FFF printing. However, for SLS printing, an industry approach is to use vertical print results as a conservative estimate for design values. For SLS printing, vertical print performance is typically only slightly worse than that of flat

FIGURE 3.8: Successful ThermaX PEEK vertical print

prints. This same approach is more difficult for FFF printing where the performance differences are more drastic, and hence vertical properties are overly conservative for flat printed parts.

3.4 Coupon Size and Shape Effects

One aspect of FFF printing that was studied was the effect that coupon size and shape had on performance. With FFF printing, the bond strength between consecutive filament passes is a function of multiple variables (see Subsection 2.2.1). One of these variables is the time it takes for consecutive filament passes to be printed. The longer it takes for consecutive passes to be printed, the longer the previous pass has had to cool down. This cooling will reduce the bond performance between the passes. Since the bond strength is dependent on the time it takes for consecutive layers to print, FFF part quality should be affected by the part size, which affects the print time. Additionally, this study on the effect of different coupon shapes was performed to try to prevent coupons from breaking in the radius of the coupon, which occurred with some of the

Type I coupons used in Section 2.3 as shown in Figure 3.9.

FIGURE 3.9: Type I ThermaX PEEK coupon broken in the radius

The first study on the effect that coupon types had on performance was done with Onyx (see Subsection 3.4.1).

3.4.1 Onyx Coupon Type Study

Four different types of Onyx coupons were tested in tension and compared. The different coupon types were the Type I coupon, Modified Type I coupon, Type II coupon, and Type V coupon (see Appendix A). The results of the testing are shown in Figure 3.10, in which all the coupons were printed flat with a [00,90] raster.

Based on the results of the testing, it appears that the coupon type affected the performance of Onyx in terms of stiffness, ultimate strength, and ductility. The Type II and Type V coupons are less likely to break in the radius of the coupon which can account for the greater ductility seen by those coupons. Additionally, the difference in performance between the different coupon types could be explained in part due to the shell layer of the coupons (see Subsection 2.2.2). The print direction of the shell layers is not dependent on the raster angle of the coupon. For the tension coupons, the shell layers were always printed in the direction of the load in the intended break region of the coupon. As the cross-sectional area of a coupon decreases, the shell layer begins to have a larger effect on the behavior of the coupon.

This material's performance being highly dependent on coupon shape is another reason why Onyx was not recommended for future use on this project (see Chapter 4). A

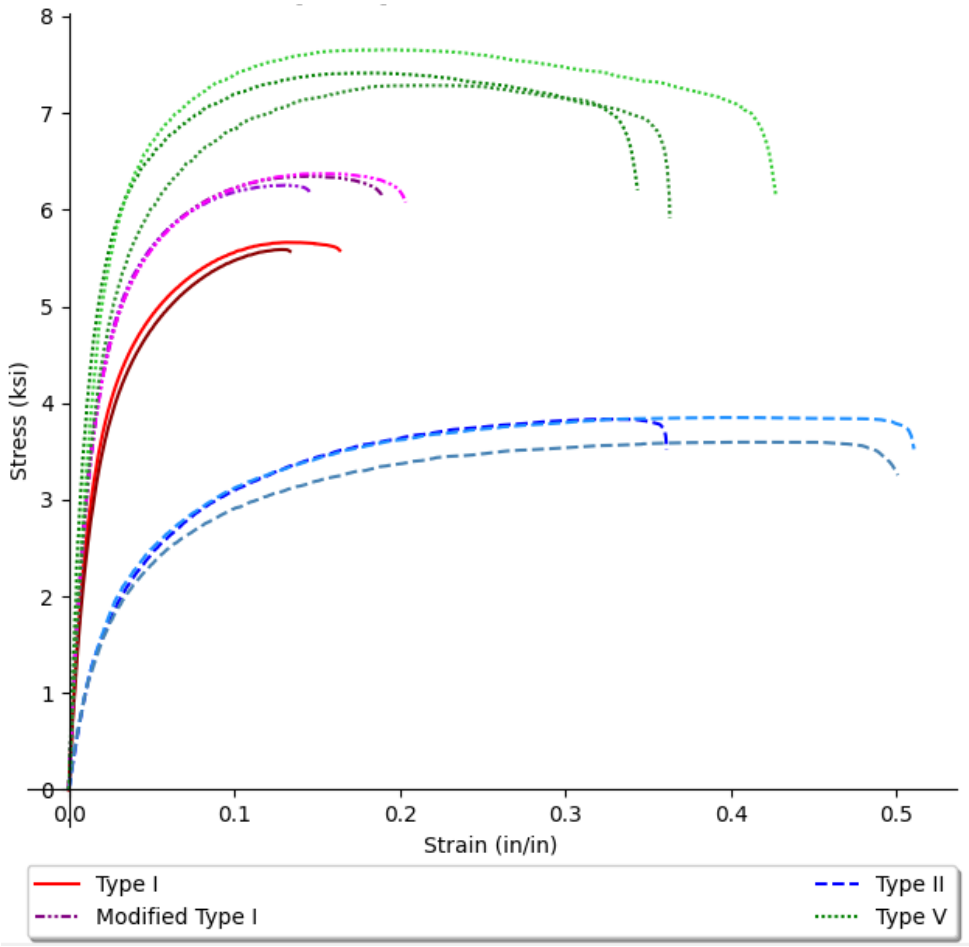

FIGURE 3.10: Onyx coupon type comparison stress vs strain curves

similar study on the effects of coupon type on performance was also done with ThermaX PEEK (see Subsection 3.4.2).

3.4.2 ThermaX PEEK Coupon Type Study

Three different types of ThermaX PEEK coupons were tested in tension and compared. The different coupon types were the Type I coupon, Modified Type I coupon, and Type V coupon (see Appendix A). The results of the testing are shown in Figure 3.11, in which all the coupons were printed flat with a [-45,+45] raster.

The results in Figure 3.11 show that there is less difference in the tensile behavior between the different coupon types when compared to Onyx. It is important to note that

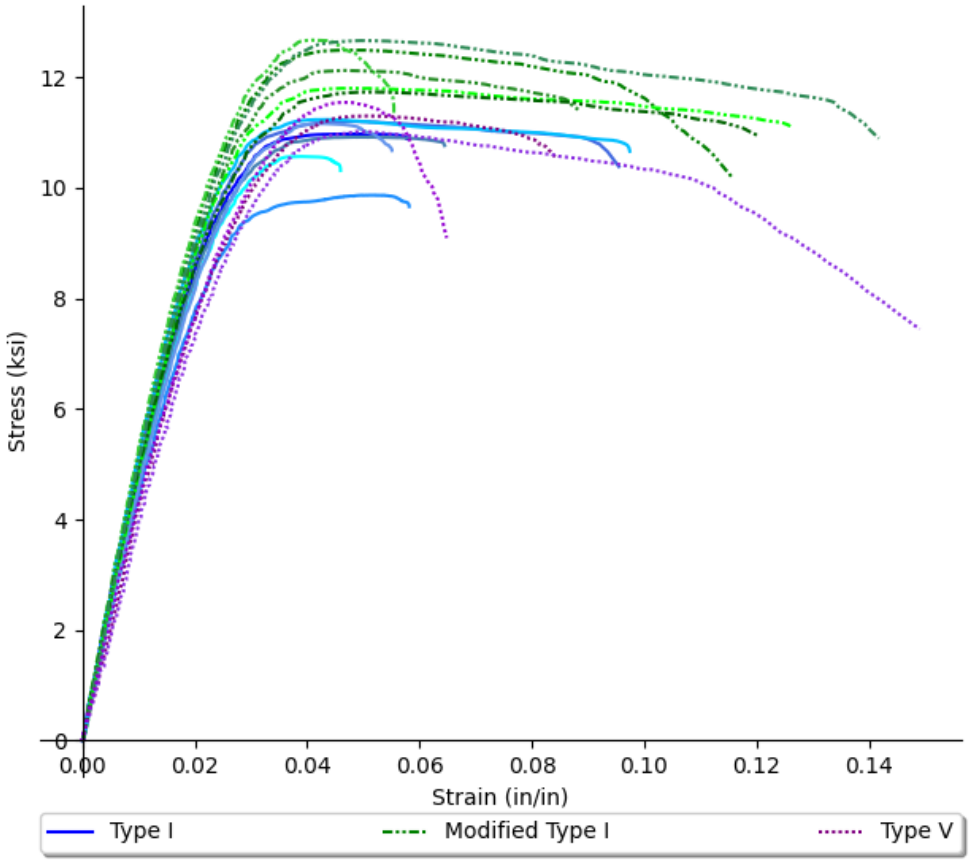

FIGURE 3.11: ThermaX PEEK coupon type comparison stress vs strain curves

the Type V coupon group in Figure 3.11 did not have a shell layer. The Type V coupon has a significantly smaller cross-sectional area when compared to the Type I coupon. This smaller cross-sectional area makes the behavior of the Type V coupon more susceptible to being dominated by the shell layers. The lack of shell layers on the Type V coupons could explain why there is not a significant difference in behavior between the three coupon types. It is important to note that when choosing a coupon type to characterize the material system behavior, one should consider whether it is the shell or infill behavior that is of interest. This would dictate which coupon size to use. Large coupons are dominated more by the infill.

A study was also performed on both ThermaX PEEK and Onyx to determine the effect that coupon thickness had on the performance of the tension coupons (see Subsection

3.4.3).

3.4.3 Coupon Thickness Study

This subsection investigates how coupon thickness affected the performance of the tensile coupons. The coupons discussed in this section are all the Type V coupon type (see Appendix A) with a [-45,+45] raster. Figure 3.12 shows the results of tension testing with Onyx that compares coupons with varying thicknesses.

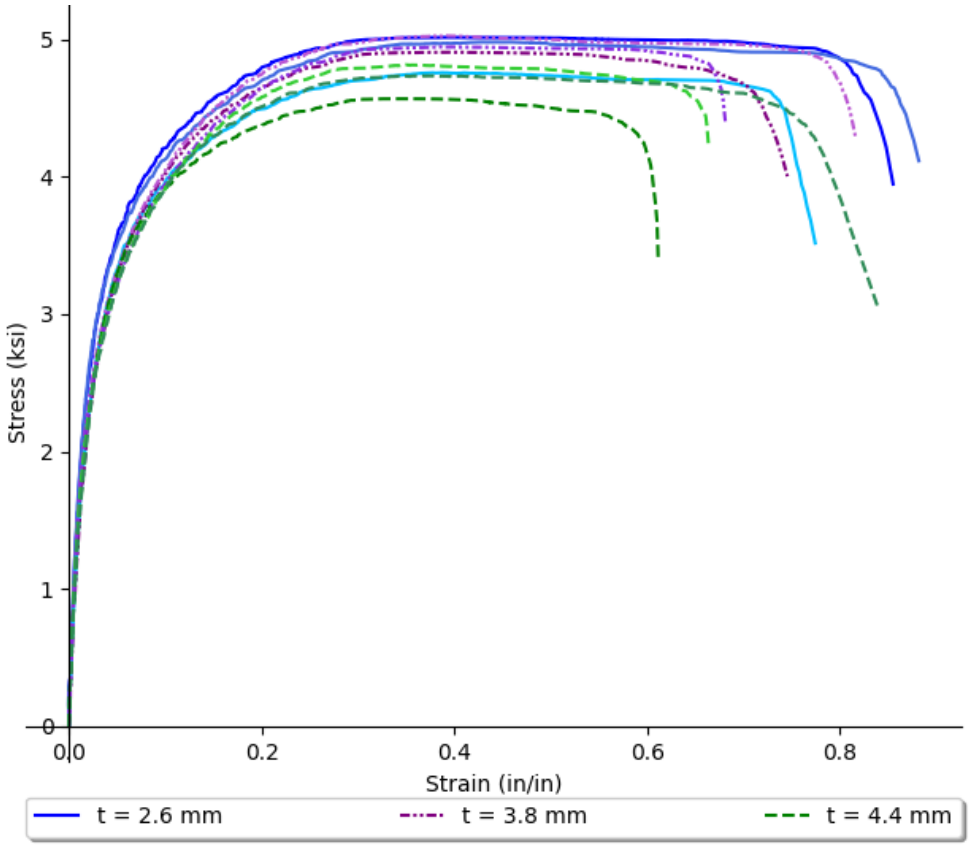

FIGURE 3.12: Onyx thickness study stress vs strain curves

Figure 3.13 shows the results of tension testing with ThermaX PEEK that compares coupons with varying thicknesses.

From Figures 3.12 and 3.13, thicker coupons appear to be less ductile, particularly for the ThermaX PEEK material. It is important to note here that the thicker ThermaX PEEK coupons did not have shell layers while the thinner ThermaX PEEK coupons

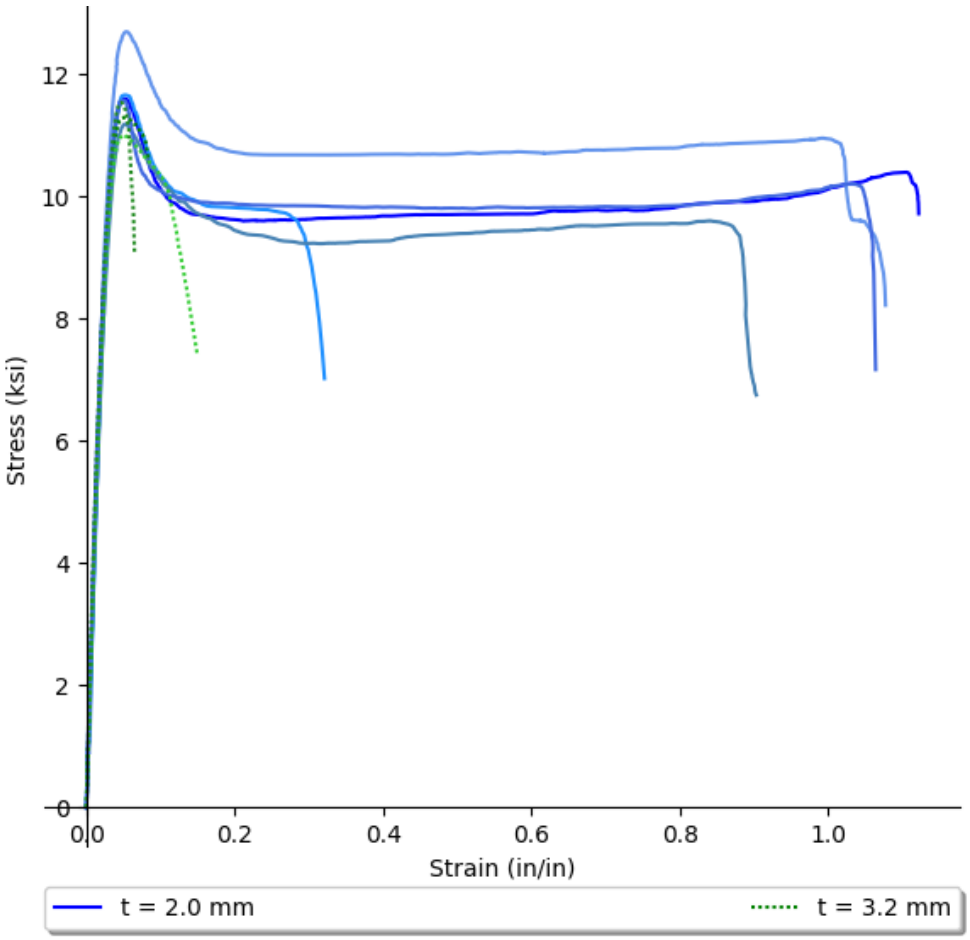

FIGURE 3.13: ThermaX PEEK thickness study stress vs strain curves

did have shell layers. This could be an explanation for the difference in ductility seen in Figure 3.13.

Both the Onyx and ThermaX PEEK materials demonstrated more ductile behavior from the thinner set of coupons. This behavior is the opposite of what is often seen by coupon tests of metals in literature. Often, coupons with higher slimness ratios, K, demonstrate less elongation during a tension test [*Measuring the Ductility of Metals*]. The slimness ratio is defined by the equation below:

$$K = \frac{L_o}{A_o^{1/2}}$$

$$K = \text{slimness ratio}$$

$$L_o = \text{original gauge length}$$

$$A_o = \text{original cross sectional area of specimen}$$

Coupons with a smaller cross-sectional area have a larger slimness ratio. If the coupons tested for the thickness study in this project had followed the slimness ratio trend presented in literature, the thicker coupons would have demonstrated a higher elongation; this was not the case. It was believed that, if the differences in ductility were not caused entirely by the shell layers, the differences in ductility between the coupon groups of different thicknesses could be explained in part by plane stress versus plane strain behavior.

A thin part or coupon pulled in tension is usually considered to be in the 2D plane stress state in which the out-of-plane strain is completely unrestrained. As the thickness of that part increases, it begins to approach the 2D condition of plane strain in which the thickness is assumed to be so large that out-of-plane strains are considered to be zero [Ugural and Fenster, 2012]. For the same given stress state, a part modeled in the plane stress condition will have higher longitudinal strains than a part modeled in the plane strain condition. Figure 3.14 shows the percent difference in the longitudinal strain calculated using the two different conditions as a function of Poisson's ratio.

From Figure 3.14 it can be seen that for a material that has a Poisson's ratio in the typical polymer range, the percent difference in the calculated strains can be up to 18%. It is important to note that while the difference between a plane stress and a

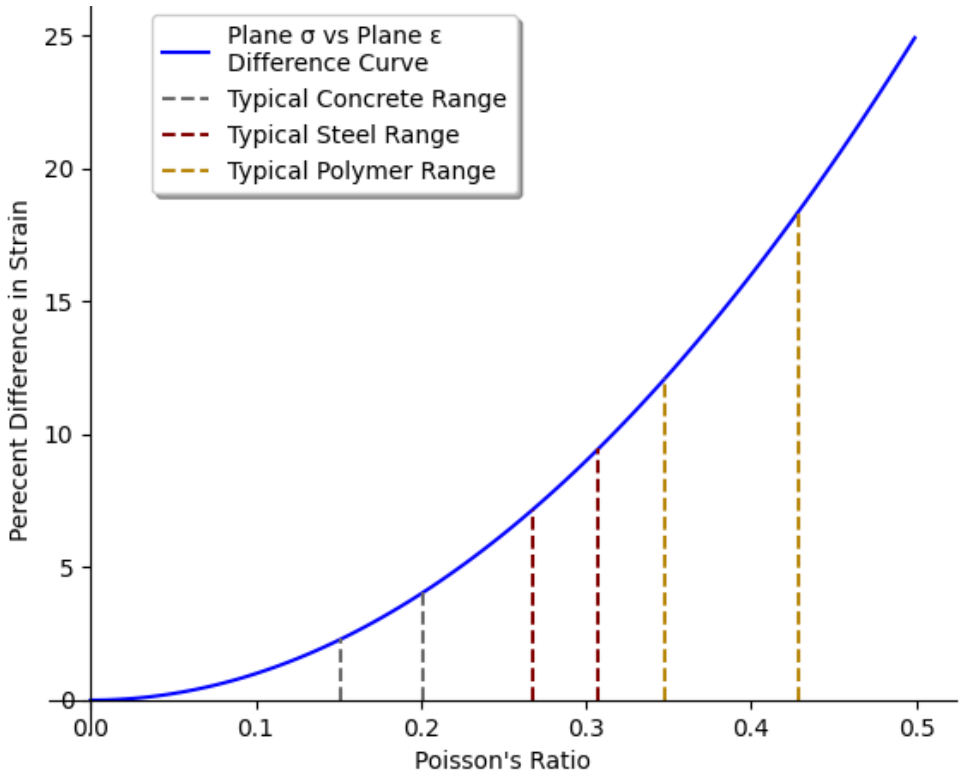

FIGURE 3.14: Percent difference in longitudinal strain between plane stress and plane strain

plane strain state could be responsible for some of the differences in ductility seen in Figures 3.12 and 3.13, it is unlikely to be the main cause of the differences. This is because the plane stress and plane strain conditions are only to be applied to linear elastic materials. While the tension stress vs strain curves for Onyx and ThermaX PEEK appear to be linear at the start of the test, the differences in ductility seen between the different coupon groups present themselves after the linear behavior is over and after plastic behavior begins. Additionally, the thicknesses used in the tension tests were unlikely to be large enough to approach a condition of plane strain. To verify this, a finite element analysis of coupons of varying thicknesses was done to determine the difference in the out-of-plane and longitudinal strain as a function of the thickness of the coupons.

The finite element analysis was performed on coupons ranging in thickness from 1 mm to 30 mm. The boundary conditions were created to recreate the boundary conditions

of the grips used during tension testing. The bottom grip boundary condition was replicated by fixing two opposing faces, or the faces that touch the grips as shown in Figure A.3. The top grip boundary condition was replicated by fixing the faces of the coupon that would touch the grips but allowing displacement in the axial direction. The coupon was loaded with a pressure on the top face of the coupon. The Poisson's ratio used for the analysis was 0.4 which is a typical value for polymers. The load and modulus of elasticity were chosen to be 30 MPa and 1200 MPa respectively, which is within the range of loading moduli found for Onyx (see Subsection 2.3.3). Once the analysis was performed, the values of the out-of-plane strain in the thickness direction and the values of the axial strain were taken at the midpoint of the coupon. These values were then normalized by the axial stress at the midpoint of the coupon. Figure 3.15 shows the Abaqus model boundary conditions and loading as well as the partitioned view of the coupon at the midpoint after the analysis was complete.

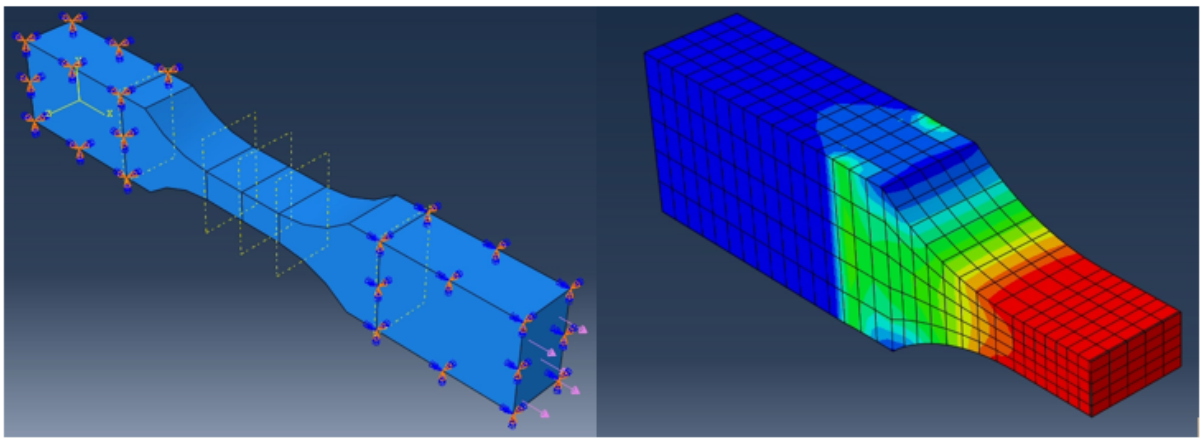

FIGURE 3.15: Type V coupon with t = 6.0 mm Abaqus model (a) Boundary conditions and loading (b) Axial strain contour partitioned with a view cut at the midpoint

Figure 3.16 shows the results of the Abaqus analysis.

The results shown in Figure 3.16 match the expected results. Coupons with a small

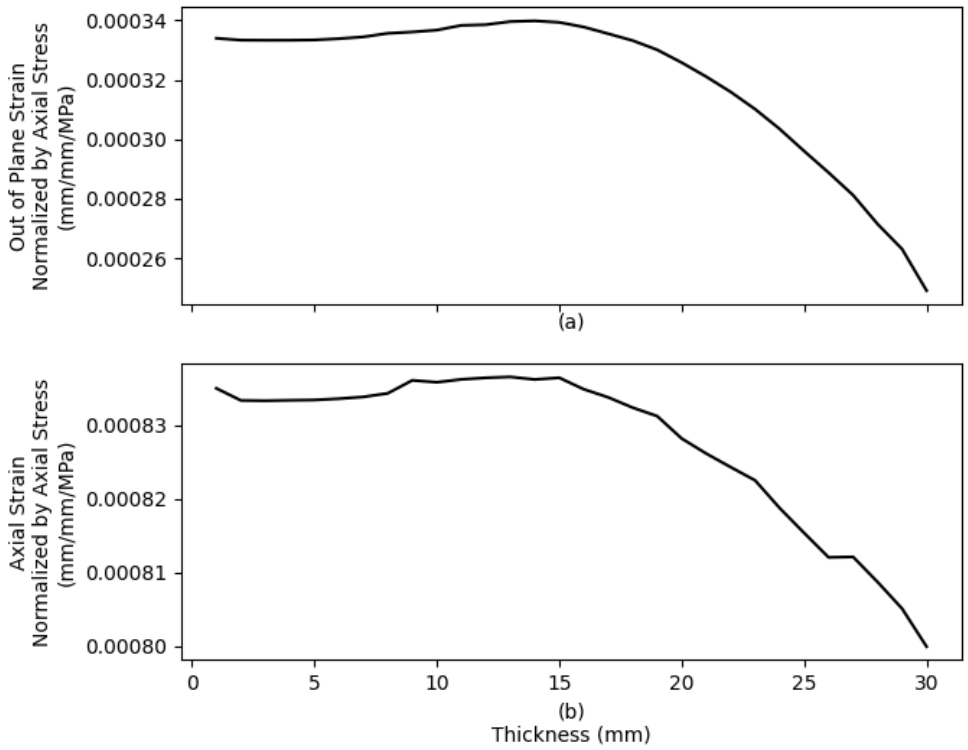

FIGURE 3.16: (a) Out of plane strain in the thickness direction normalized by axial stress vs coupon thickness (b) axial strain normalized by axial stress vs coupon thickness

thickness are in the plane stress state and should have a higher unrestrained out-of-plane strain. As the coupon thickness increases, the coupons should trend towards a plane strain condition in which the out-of-plain strain is restrained. This behavior is shown in Figure 3.16(a). For coupons that have a larger thickness, more stress is also required to produce an equivalent axial strain as would be seen in a thinner coupon. This behavior is shown in Figure 3.16(b). While the Abaqus results do show that thickness can have an impact on the axial strain of coupons due to a difference between plane stress and plane strain, this difference does not begin to occur until coupons with a thickness of at least 15 mm are used. This thickness is significantly larger than the thickness of the coupons used during the actual testing. This means that the differences in the ductility of the coupons seen in Figures 3.12 and 3.13 are likely due to the additive manufacturing process.

3.5 FFF Layer-Time Control Protocol

As discussed in Subsection 2.2.2 the vertical print strength depends on the bond strength between the layers. The bond strength between consecutive layers is affected by the material, the print temperature, and the time it takes for a layer to complete. This section discusses a potential method for quantifying how different layer times affect the bond strength between layers.

Three coupons were printed in the print bed alone (3 separate prints resulting in three coupons), and three coupons were printed in the print bed along with a plate near it at mid-height (3 separate prints resulting in three coupons). The goal of the coupons printed with a plate at mid-height was to induce a cold joint at that location. An image of what this looks like is shown below in Figure 3.17.

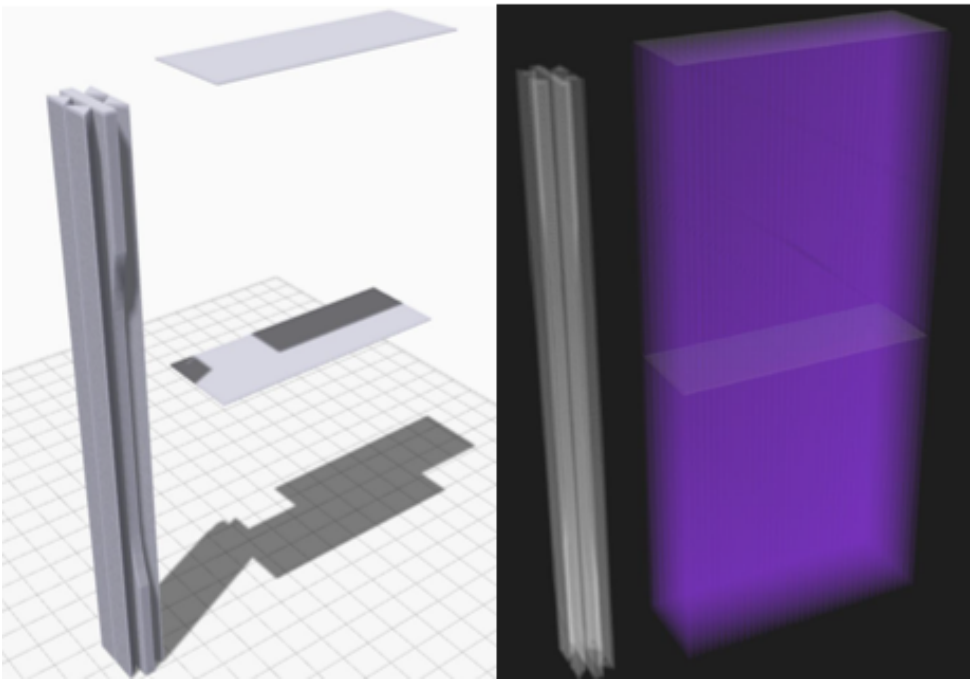

FIGURE 3.17: Vertical print with cold joint induced at mid-height

On the left of the image, it can be seen that the tensile coupon is printed with 2 triangular supports on each side of the coupon. These are structural supports required to ensure quality prints (see Section 3.3). On the left of the image, one can also see the

plate at mid-height of the coupon. This requires support material to be printed in order to hold up the plate at mid-height (purple color in the right image). Another plate was printed at the top of the coupon in order to cause support material to be printed on the top half which results in uniform support layer time throughout the height of the coupon.

The coupons were then subjected to tension testing. For the coupons printed without the plate in the print bed, the layer time is 17 seconds. For the coupons printed in the bed with the plate at mid-height, the layer time is 54 seconds below and above mid-height; the layer time is 103 seconds at the mid-height of the coupon. There would have also been an option to simply pause the print when the printer nozzle was at the mid-height of the coupon; however, there was good reason not to do this. When FFF printers pause during a print, a geometric imperfection often occurs in the location where the nozzle was paused. There is also the potential of a material imperfection occurring in a location where the material flow is paused. This was seen both in prints using the printers for the Onyx material and the ThermaX PEEK material. If the vertical coupon prints had simply been paused at mid-height, the ensuing tension tests would have been testing the effect of a geometric and material imperfection on the coupon, rather than the effect of a cold joint on the coupon. This study of the cold joint effect on the bond strength was performed only on the Onyx material since it was the cheapest and most available material during this project. The results of the tension tests on these coupons can be seen in Figure 3.18 and Table 3.5. The third cold joint coupon that was tested was omitted from the results presented below. This is because it had a significantly higher modulus and ultimate stress than any of the other coupons. Additionally, this coupon did not break at the cold joint. The higher modulus and ultimate stress values are not believed to be related to the cold joint and therefore this coupon was treated as an outlier.

From the results, it can be seen that the cold joint does not seem to have a significant

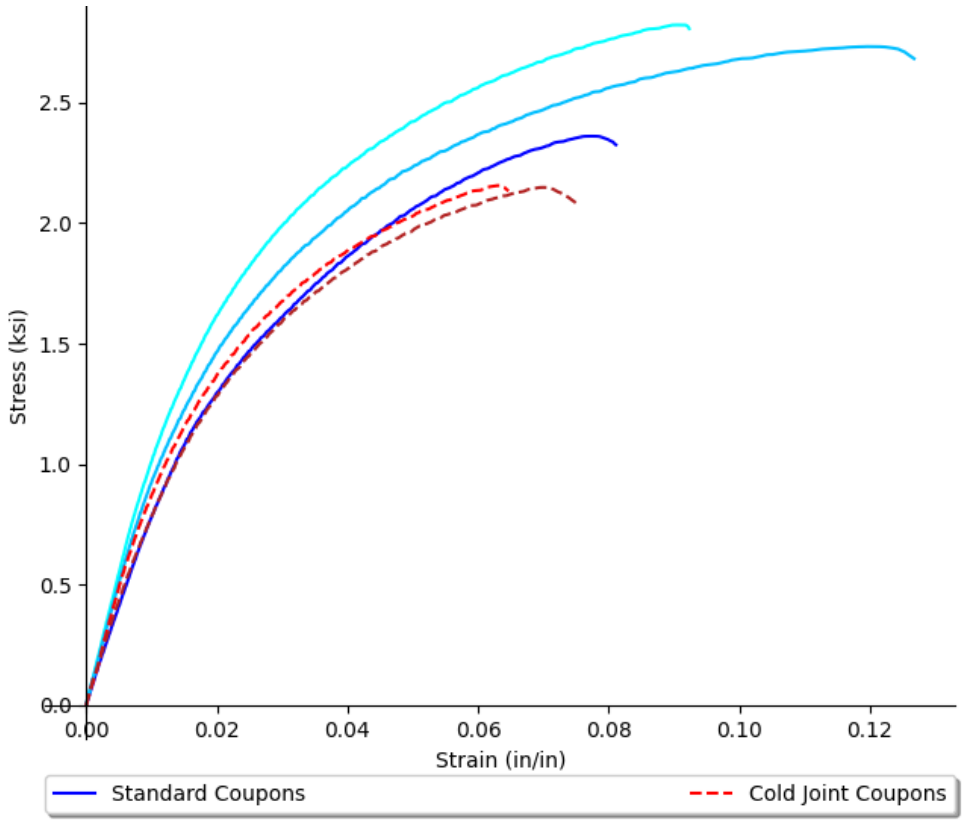

FIGURE 3.18: Vertical print with cold joint stress vs strain curves

Coupon Type	Test Modulus (ksi)	Test Ult. Stress (ksi)	Test Break Strain (%)
Standard	98	2.6	10.0
Cold Joint	93	2.2	7.0

TABLE 3.5: Cold joint testing average results

impact on the stiffness or ultimate stress, but it does seem to have a fairly significant impact on the breaking strain. Additionally, the cold joint forced the coupons to break right where the cold joint was created while it is common for the standard coupons to break at random locations along the narrow section or even in the radius of the coupon. Figure 3.19 shows an image of a standard coupon broken towards the end of the narrow section. Figure 3.20 shows a typical image of the coupons with the cold joint at mid-height broken at the location of the cold joint.

This process or a similar process could be implemented as a protocol to test the effect

FIGURE 3.19: Vertically printed standard broken coupon

FIGURE 3.20: Vertically printed broken coupon with cold joint broken at the cold joint

of layer time on the performance of FFF printed parts without inducing an unwanted geometric imperfection in the coupons being tested. Fracture initiates at imperfections in the coupon. It is dictated by the most significant random imperfection. One of those imperfections is cold joints. That cold joint is usually the most significant imperfection, but it may not be.

This imperfection-driven failure (and the fact that 3D printing has a lot of imperfections) led to significant variability in breaking strain. This affected ductility more than the strength.

4 Final Material Recommendations

From the material testing results shown in Chapters 2 and 3, it was determined that HT-23 and ThermaX PEEK would be the best materials to pursue in the future for this project. These materials were chosen for their stiffness, strength, and resistance to degradation from thermal cycling. Both materials do not seem to be significantly affected by degradation from thermal cycling. Additionally, both materials have about the same ultimate stress. The HT-23 material is stiffer than the ThermaX PEEK, but the ThermaX PEEK does have better ductility than HT-23. The importance of ductility has been left for a future study. That study will explore impact response, ability to handle drilled holes, and fatigue response.

The FR-106 is not recommended for further use due to the poor performance of the coupons as seen in Subsection 2.3.1. The testing of the FR-106 coupons showed that they had a low performance when compared to the material supplier specifications. While this low performance in comparison to the supplier specifications was the main reason for not pursuing FR-106 more for this project, the material would likely still not have made the final material recommendations. This is because FR-106 does not have a high stiffness even according to the material specifications. The FR-106 material is about 20% as stiff as HT-23. This lack of stiffness would have made it an unlikely candidate for the final material recommendations even if the coupons had performed well in comparison to the supplier specifications.

The Onyx material is not recommended for further use on this project mainly due to the low yield stress of the material. The access door will be subjected to dynamic or

cyclic loading under real flight conditions meaning that a material with a stiffness that degrades quickly under cyclic loading is not an ideal material for this project. Additionally, the performance of the material appears to have a high dependence on coupon shape (see Section 3.4). This makes the performance of the material difficult to predict which is not ideal for material to be used for the design of new parts. Also, the material did not perform well when subjected to degradation from thermal cycling. This makes Onyx a non-ideal material to use for a part that will be subjected to environmental conditions.

The Onyx material with continuous carbon fiber reinforcing is not recommended for further use due to the limited print complexity allowed. Using both a matrix and continuous reinforcing material greatly limits the allowed complexity of a part such as increasing the minimum thickness allowed for use, and continuous fiber cannot be placed efficiently along curves in the Z or vertical print direction. Since this part has thin walls and a curved skin (see Chapter 5), this matrix and reinforcing combination cannot be efficiently utilized for this project. Additionally, the degradation from thermal cycling of the matrix is a concern, however, that did not appear to affect the combined system response.

5 Geometry Selection

5.1 Overview

This chapter discusses the geometry selection process, the design process, and the structural analysis performed on the new designs for the access door.

5.2 Geometry Selection Process

The geometry selection for this part needed to result in an access door with the same stiffness as the original part. The design would also need to be suitable for both FFF and SLS printing. A common geometry seen in composites manufacturing and in additive manufacturing is a sandwich panel. A sandwich panel consists of a top and bottom plate with a core in the center and works in a very similar way to an I-beam. Typically with a sandwich panel, the amount of material in the plates is maximized while a minimal amount of material is used for the core. Since the core moves the plates away from the neutral axis, the plates provide a majority of the part's stiffness allowing for minimal material to be used. A common type of sandwich panel core is the honeycomb core as shown in Figure 5.1.

There were two main reasons as to why a sandwich panel was not pursued for the service access door. The first reason is that the part is exposed to moisture meaning it needs to be able to drain liquid if any becomes trapped on the inner face of the access door. Figure 1.2 shows how the original access door has draining holes to allow for liquid to drain away from the inner stiffeners. The access door is on the bottom

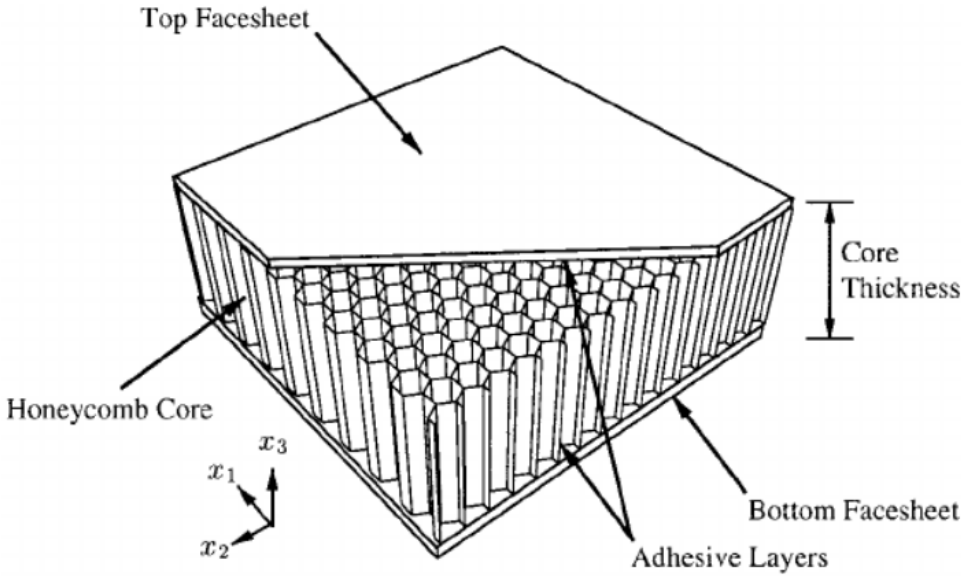

FIGURE 5.1: Typical sandwich panel with a honeycomb core [Han, 2002]

of the fuselage, and hence the stiffeners would hold water without the holes. While a limited number of drainage holes could work for a part with minimal stiffeners as seen in the original door design, a part with a densely packed core would struggle to drain liquid out of each individual hollow cell. This trapped water could lead to part damage during freeze and thaw cycles. If the core of a sandwich panel was sealed, then moisture would not be able to be let in. There was concern that, with 3D printing, the core would not be sealed, and hence an open design is better. The second main reason the sandwich panel was avoided was to make the new design compatible with SLS printing. With SLS printing, the entire print volume is filled with powder. While this allows the printer to avoid needing support structures, it causes any hollow spaces in a part to be filled with unsintered powder (see Subsection 2.2.2). To remove this powder inside of a hollow section of a part, drainage holes are required. Attempting to remove all of the powder from the hollow spaces in a dense core as seen in Figure 5.1 would be a very difficult process, and it would be nearly impossible to ensure all the powder was removed from the core. Due to the need for liquid drainage and powder removal, the sandwich panel was not pursued for this project, and a more open part design was

chosen.

Exposed stiffeners similar to those seen in the original part design were considered; however, due to the fact that the materials selected for this project were significantly less stiff than aluminum, more material would be needed to match the stiffness of the original part. To achieve an equal part stiffness with less stiff materials, a sandwich panel would have been an ideal geometry, however, a sandwich panel was already deemed unsuitable for reasons previously stated. Due to this, a middle ground between a sandwich panel and exposed stiffeners was chosen in the form of a waffle-grid of hat stiffeners as seen in Figure 5.2. In this thesis, a hat stiffener will refer to two vertical stiffeners connected together on the top and bottom creating a shape similar to a Hollow Structural Section (HSS) or a bridge box girder. This is a shape used often for structural engineering for its high bending and torsional stiffness.

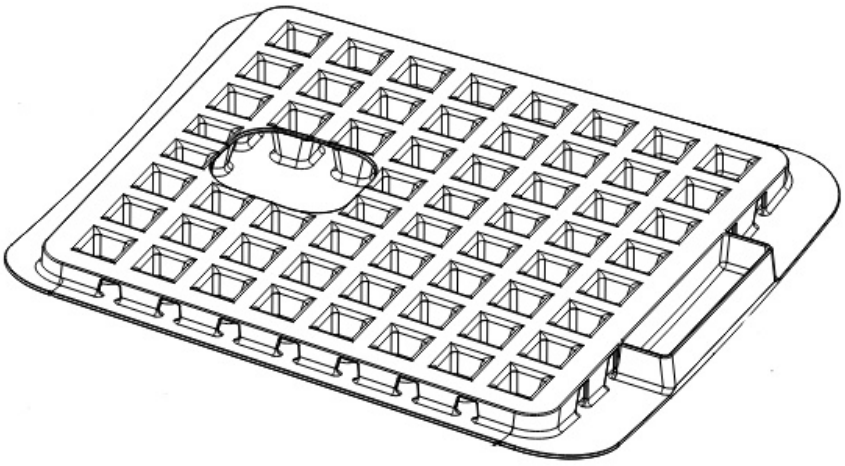

FIGURE 5.2: Waffle-grid layout of stiffeners

The waffle grid of stiffeners allows for large open channels to run in both directions as seen in Figure 5.3. As seen in the figure, the hat stiffeners have angled webs. The angled webs reduce the amount of support material required for printing the unsupported top flange during an FFF print. While the stiffener webs are angled in the final part design, they were approximated as vertical during the design process.

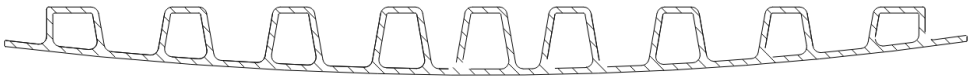

FIGURE 5.3: Cross section of hat-stiffeners

These channels make it possible for water to drain, and they allow excess powder to be removed after an SLS print. An added benefit of the open channels created by the hat stiffeners is that they allow for visibility on the interior of the entire panel. With a sandwich panel design, it is very difficult to determine if there is a defect in the part unless the defect is on the out fiber of the plates. Additionally, water intrusion cannot be observed in a sandwich panel. That water intrusion would cause freeze-thaw issues. The open channels here would allow one to visibly inspect the interior and exterior of the stiffeners for defects created by the printing process or by loading damage. While a waffle grid stiffener layout would be challenging to create by hand, this layout is able to utilize the complex geometries able to be manufactured by additive manufacturing. After the waffle-grid of hat stiffeners was chosen as the geometry to be used for the final part design, the sizing of the panel stiffeners needed to be determined.

5.3 Final Design Parameters

The sizing of the panel was determined based on the size and stiffness of the original aluminum access door. There was not an explicit stiffness limitation for the access door, so it was decided to match the stiffness of the new access door to that of the existing one. To match the stiffness of the original door, an approximate FEM model of the original door was created in Abaqus as seen in Figure 5.4.

With this simplified model, all of the stiffener heights were made the same and the curvature of the panel was removed. The drainage holes in the stiffeners were also removed from the model. Additionally, there is no overhanging fuselage skin past the exterior stiffeners. Here fuselage skin refers to the part of the access door that is

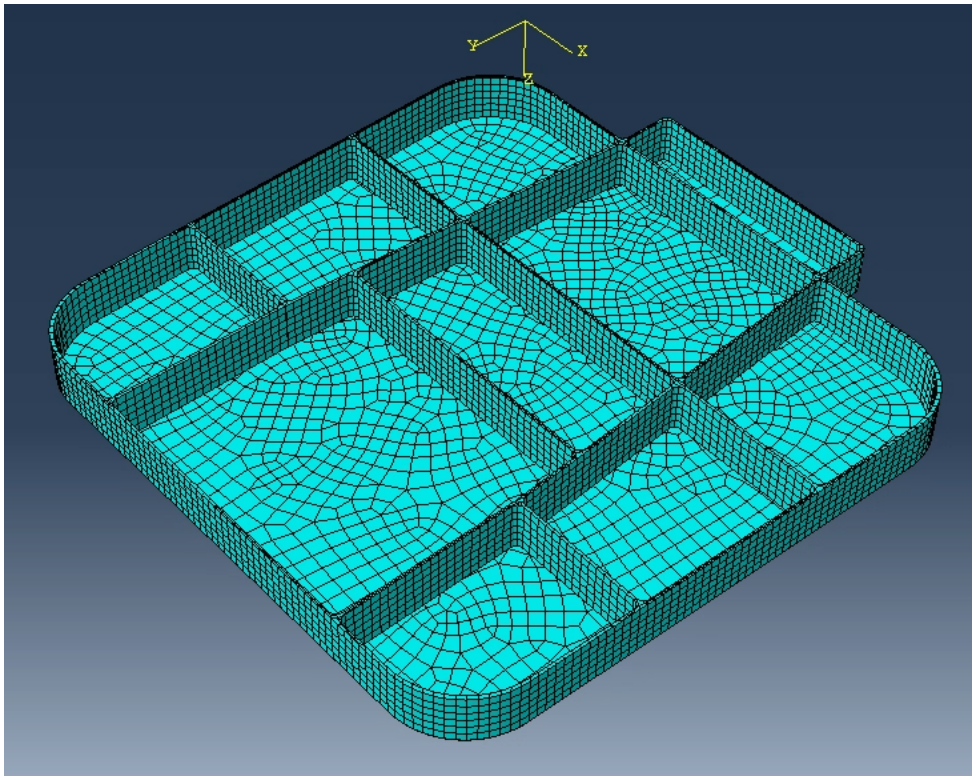

FIGURE 5.4: Approximate Abaqus model of original access door

seen from the exterior of the aircraft, which is the side without the stiffeners. This overhanging skin was removed because the model was treated as being pinned along the exterior edge of the stiffeners. The pinned support was used because the actual support conditions of the access door were unknown. In the actual part, there would be a hinge that causes some additional fixity at one edge, however, the size and stiffness of the hinge were unknown. A uniform static pressure load of 1.5 psi was placed as a distributed transverse load on the skin of the model to determine how much the access door would deflect. This load comes from a blowout pressure that is used for this part of the plane. The access door is in a non-pressurized region so the normal pressure difference between the inside and outside is not very large. In the model, the direction of the load was going towards the skin causing compression in the skin. As can be seen in Figure 5.5, the majority of the deflection occurs in the place where there is the largest space between the stiffeners.

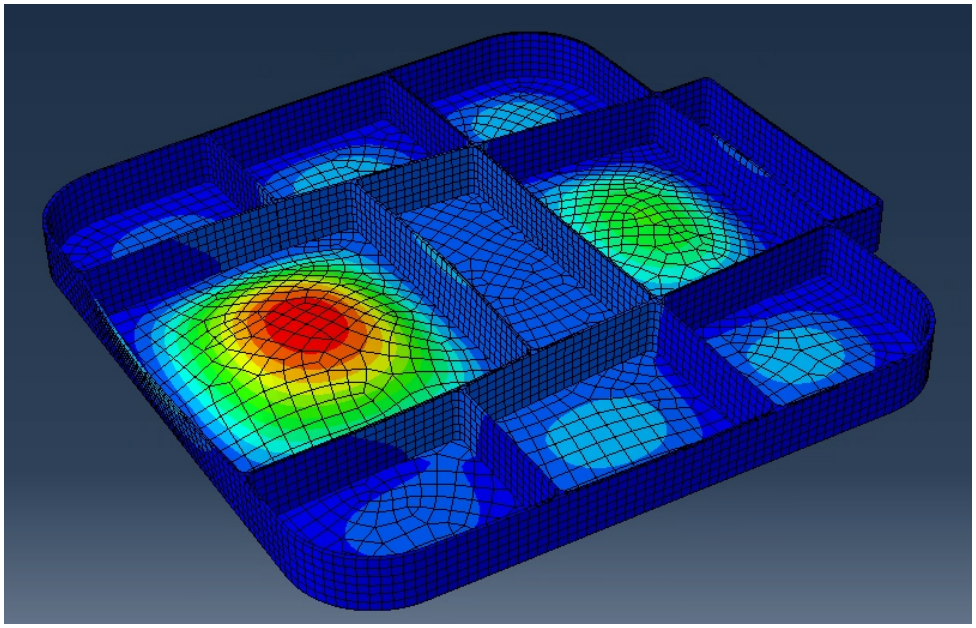

FIGURE 5.5: Approximate Abaqus model of original access door deflection

This location on the panel is also where the access door's handle is located, however, the handle shape and size were unknown. The maximum deflection was taken from this Abaqus model and used as the basis for the design for the new access door. Determining the maximum deflection of the original panel was the first step in the design process. The new access door design would need to have a maximum deflection equal to or less than the value obtained from the original access door Abaqus model.

The second step in the design process was to treat the access door for the new materials as a rectangular plate. Then, thin plate theory was used to determine the thickness of a plate that would be required to achieve a deflection equal to the deflection found from the original access door Abaqus model using the following equation [Ugural and Fenster, 2012]:

$$t = \left(\frac{12(1-\nu^2)D}{E} \right)^{1/3}$$

$t =$ thickness of flat plate required to match the deflection of original part

$D =$ plate bending stiffness required to match the deflection of original part

$\nu =$ Poisson's ratio

$E =$ elastic modulus

The plate bending stiffness required to match the deflection of the original part Abaqus model is found using the following equation:

$$D = \frac{16q}{\pi^6 w} \sum_{n=odd}^{\infty} \sum_{m=odd}^{\infty} \frac{sin\frac{m\pi x}{a} sin\frac{n\pi y}{b}}{mn\left(\frac{m^2}{a^2} + \frac{n^2}{b^2}\right)}$$

$q =$ uniform pressure load used in original access door Abaqus model

$w =$ maximum deflection found from original access door Abaqus model

$a =$ length of the plate in the x direction

$b =$ length of the plate in the y direction

$$x = \frac{a}{2}$$
$$y = \frac{b}{2}$$

While the access door is not perfectly rectangular as a plate would be using flat plate theory, the dimensions a and b were selected based on the average width and height of the original door in the Abaqus model.

The third step in the design process was to create a simply supported rectangular, one-way bending, beam of the same thickness as the two-way bending plate used in the previous step. This simply supported rectangular beam was then compared with a hat stiffener that had the same width to see if, under the same load, the two beams would have the same mid-span deflection. The comparison between the rectangular beam and the hat stiffener beam was the fourth step in the design process. This design process is summarized in Figure 5.6.

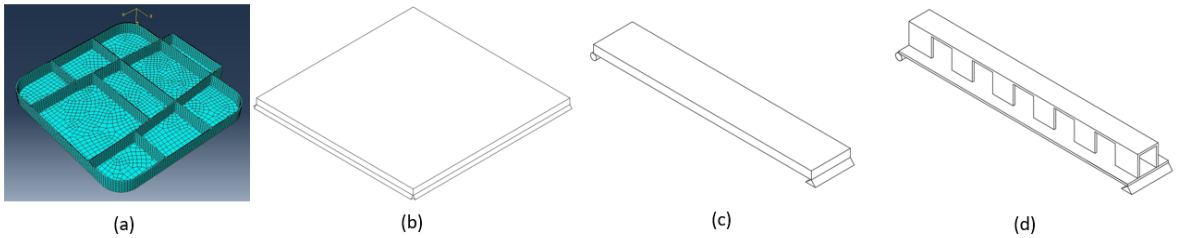

FIGURE 5.6: (a) Step one: Abaqus model of original panel (b) Step Two: Flat plate with new design material (c) Step Three: One way bending beam with new design material (d) Step Four: Hat stiffener beam with new design material

As can be seen in Figure 5.6(d) there are gaps in the webs of the hat stiffeners. These gaps are there because, in the actual waffle grid of stiffeners, that would be present in the final part, there are stiffeners running in both directions. This creates gaps in the webs of the hat stiffeners where perpendicular stiffeners meet.

In order to determine the optimal size of the hat stiffeners, a study was performed to determine which combination of design parameters would produce the lightest panel. The design parameters of the hat stiffener are noted in the bullet points below and shown in Figure 5.7:

- t = part thickness
- bf = stiffener width
- h = stiffener height
- a = stiffener spacing

- aspect ratio = h/bf

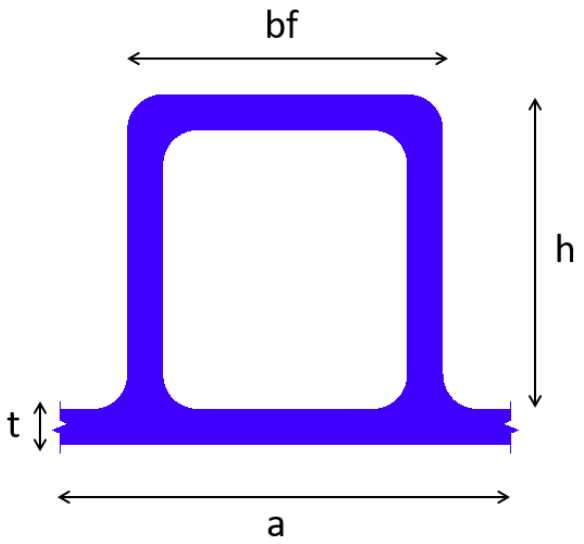

FIGURE 5.7: Hat stiffener design parameters

In Figure 5.7, the fuselage skin is the lower horizontal section, the two vertical sections are the webs, and the horizontal section on the top of the figure is the flange of the stiffener. For simplification, the same thickness was used for the skin, webs, and flange.

The first study of how the hat stiffener parameters affect the weight of the panel was performed on the part thickness and the stiffener width. The stiffener spacing and aspect ratio were kept constant in this study. Since the aspect ratio was kept constant, as the width of the stiffener grew, the height of the stiffener grew as well. The results of the study are shown in Figure 5.8.

Only data points that have enough stiffness to match the deflection from the rectangular beam are shown on the plot. It can be seen that, for each thickness, the weight varies parabolically as the flange width and height increase. The data points before the peak on each parabola are colored in blue while the data points after the peak on each parabola are colored in red. The parabolic relationship between weight and flange width and height is caused by two different behaviors before and after the peak. Before the peak, the stiffener flange and web are getting larger which adds more weight to the

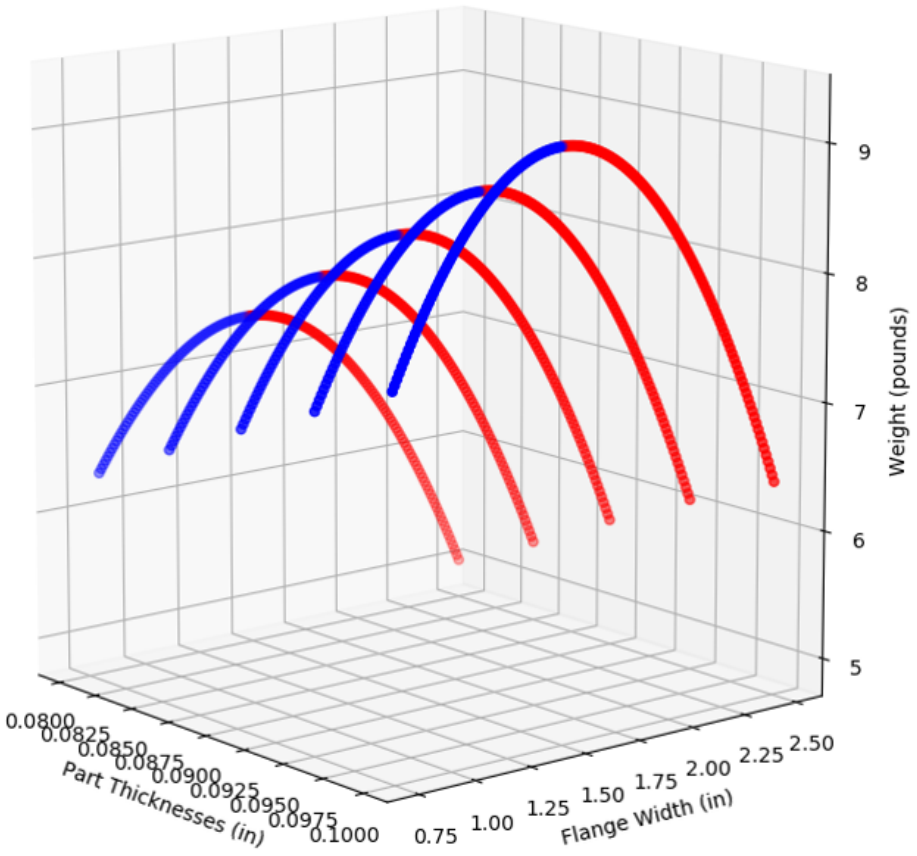

FIGURE 5.8: Door weight vs part thickness and flange width

access door. After the peak, however, more material is actually being removed from the webs. This is due to the fact that there are stiffeners running in two perpendicular directions in the waffle grid of stiffeners. As the flange width grows too large, the length of the web in each stiffener approaches zero until there are no webs at all. This results in an access door that would essentially be a sandwich panel with minimal or no core connecting the plates. While this results in a high bending stiffness when using beam theory, this is not feasible because, in reality, the two plates would not work together to resist load. Additionally, this would make the part weak in shear. Due to this, it was decided that a stiffener with the minimal flange size that would result in a stiff enough part would be the most efficient design choice.

A study was then performed on how the number of stiffeners and aspect ratio affects the size of the panel. The number of stiffeners directly affects the spacing between the

stiffeners or the parameter "a" in Figure 5.7. The results of this study are shown in Figure 5.9.

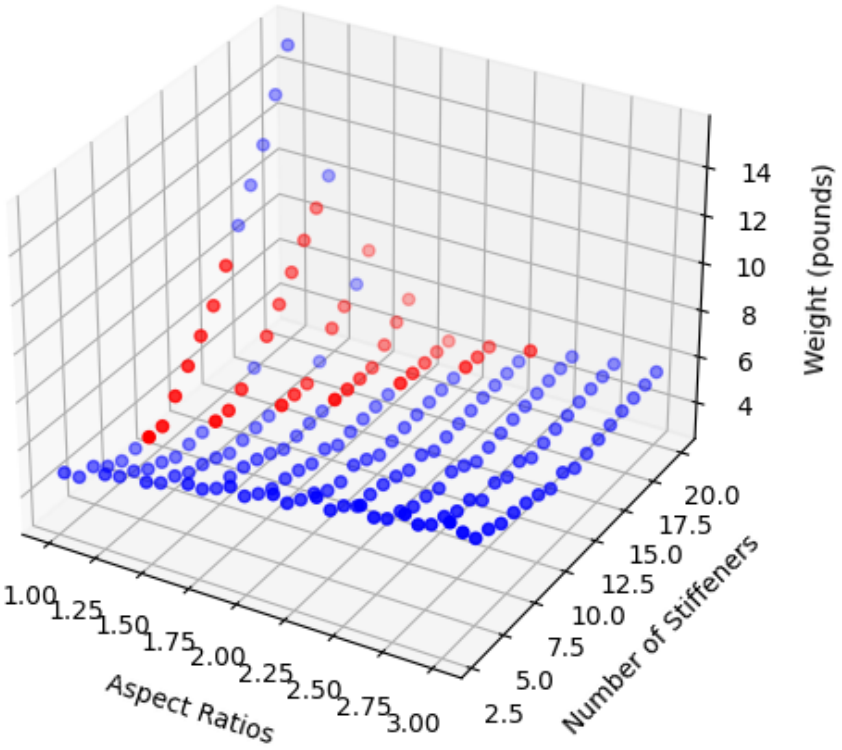

FIGURE 5.9: Door weight vs aspect ratio and number of stiffeners

The data points in Figure 5.9 are colored to match the behavior shown in Figure 5.8. The blue data points are for a flange size before the peak of the parabola in Figure 5.8, and the red data points are for a flange size are after the peak of the parabola. Additionally, in Figure 5.9 the spacing between stiffeners was forced to be larger than one-half the flange width. The minimum spacing between stiffeners is 0 inches when adjacent stiffener webs would be touching. This was done to keep the modeled panel from turning into a sandwich panel with minimal core and to avoid soft spots in the door. A soft spot refers to when there is a location in the waffle grid that has long distances between stiffener webs that would experience excess local deflections even if the global deflection of the part met the stiffness requirements. It can be seen from the figure that for aspect ratios higher than 1.5, the weight of the door does not vary

significantly with changing aspect ratio or number of stiffeners. However, for aspect ratios less than 1.5, the panel is lighter when fewer stiffeners are used. This trend is due to the fact that, when a larger number of stiffeners are used, the stiffeners cannot get tall enough to provide enough global stiffness to the part before the webs touch the webs of a stiffener next to it. To achieve the required stiffness, the thickness of the part must be increased which causes the part to be heavier.

The studies on the stiffener parameters helped inform the final design choices for the stiffeners on the new access door design. For the final design parameters, an aspect ratio of 1.0 was selected. This aspect ratio was chosen to increase the webs resistance from local buckling. With an aspect ratio of 1.0 selected, a lower number of stiffeners was selected to avoid the large weight increase observed in Figure 5.9 when a large number of stiffeners is used with a low aspect ratio. It was decided to use between 8 and 11 stiffeners. The minimum number of stiffeners to use was set at 8 to avoid soft spots that would occur between large gaps between stiffener webs which would be susceptible to large local deflections. The maximum number of stiffeners to use was selected as 11 to avoid a large increase in weight to the part. To help avoid large soft spots in the stiffener flanges or on the skin of the part, the flange width was only allowed to deviate from the gap between consecutive stiffeners by 5%. After design iteration using the process described in Figure 5.6, it was determined that 9 stiffeners would result in the most efficient part design.

After selecting the ideal geometry from the stiffener parameter studies and iterating using the design process in Figure 5.6, Abaqus models were created to check the part stiffness. The Abaqus models created for checking the stiffness of the new part were compared to the stiffness of the Abaqus model created from the original part. Since the FEM model for the original part was an approximated model due to unknown boundary conditions, the Abaqus models created to check the design iterations were also approximate models. These models ignored the curvature of the door skin and

used the same height for all the stiffeners. These models were treated as pinned around the boundary with the same pressure load applied to the original part FEM model. Figure 5.10 shows an example of one of these FEM models.

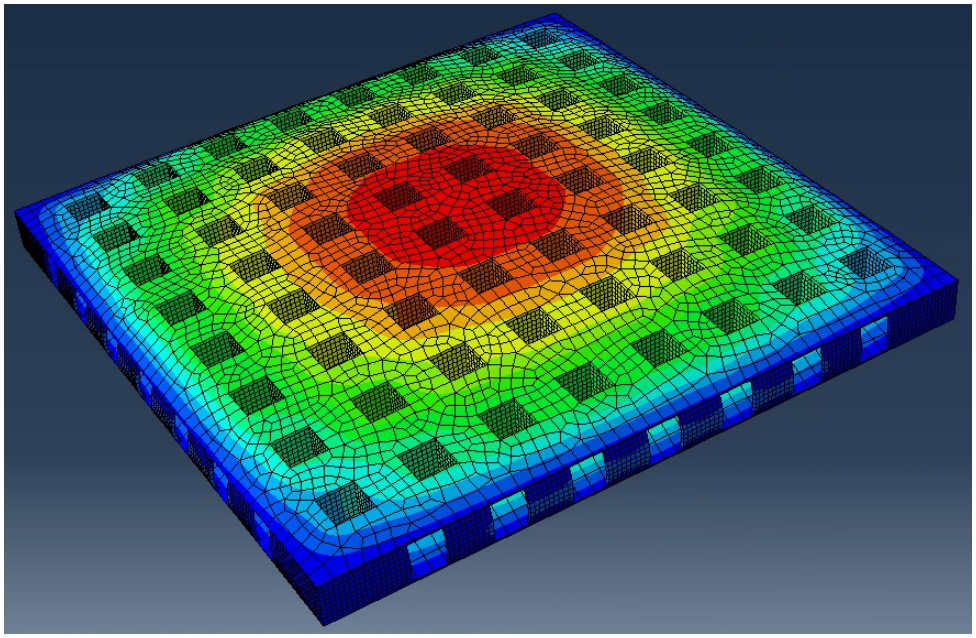

FIGURE 5.10: HT-23 approximate FEM model for stiffness check

The approximate FEM models were used as the final step in the design process. If one of the models did not have enough stiffness, then the thickness would be increased and a new model would be created. This process was done until the FEM models for both HT-23 and ThermaX PEEK had the same or more stiffness than the FEM model for the original part.

The typical final design is shown in Figure 5.2. The hole in the center waffle-grid of stiffeners is left for a handle to be placed on the part. At the rear of the panel, there is also a spot for the door hinge to be placed. The dimensions of the stiffeners for the HT-23 door are shown in Figure 5.11, and the dimensions of the stiffeners for the ThermaX PEEK door are shown in Figure 5.12.

While the thickness, stiffener size, and stiffener spacing differ slightly between the HT-23 and ThermaX PEEK panels based on the stiffness of the materials, the general shape

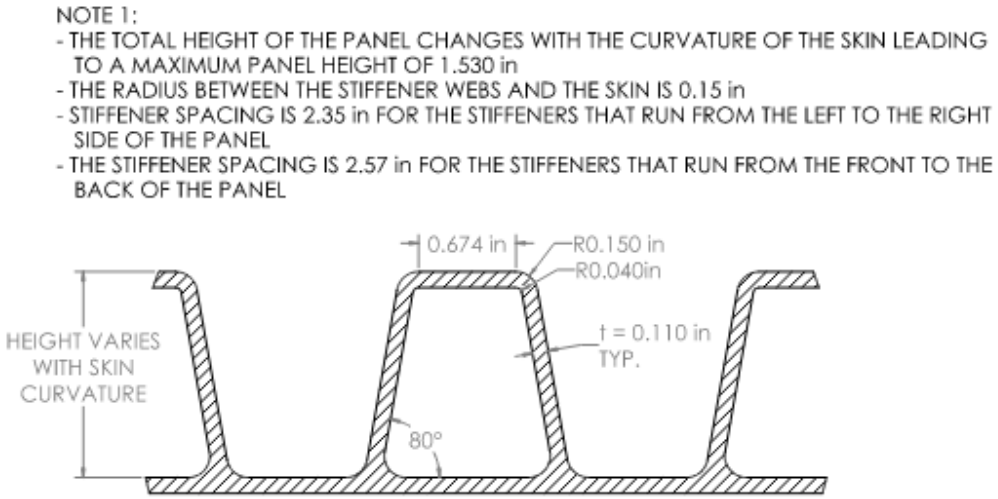

FIGURE 5.11: HT-23 stiffener details

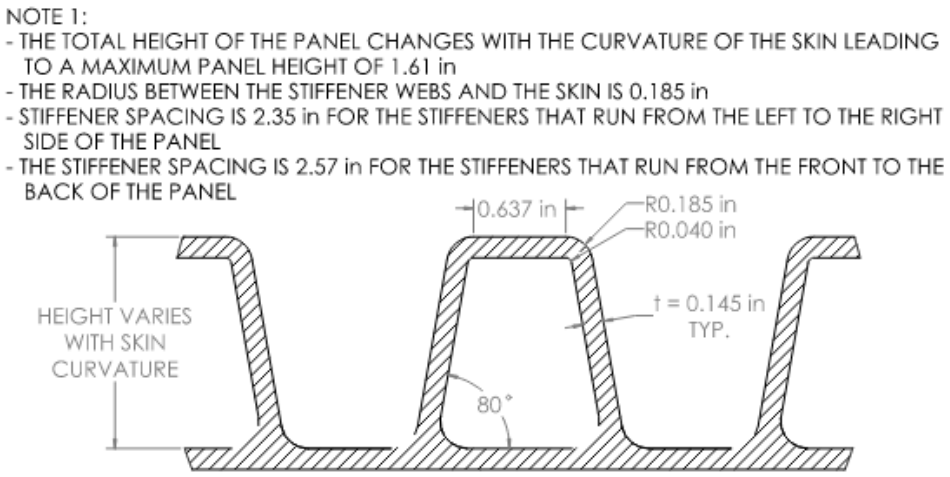

FIGURE 5.12: ThermaX PEEK stiffener details

of the panel remains the same. The final parts for both HT-23 and ThermaX PEEK were turned into Abaqus FEM models for structural analysis which is discussed in Section 5.4.

5.4 Structural Analysis

The design of the panel was approached by trying to achieve the listed design goals: (i) providing a global equivalent stiffness equal to that of the current access door; (ii)

minimizing soft-spots that would result in low local stiffness; (iii) ensuring that yield stress is not exceeded for service loads; (iv) ensuring fracture stress is not exceeded for ultimate loads; (v) ensuring buckling does not occur for ultimate loads. While the approximate Abaqus models were used to compare the global deflection of the new designs and to minimize soft-spots, the full door designs were used to ensure that yield stress was not exceeded under service loads, to ensure that fracture stress was not exceeded for ultimate loads, and to ensure that buckling would not occur under ultimate loads. The following subsections discuss the results of the analysis for design goals (iii), (iv), and (v).

5.4.1 Yield and Fracture Stress Check

This subsection discusses the results of the structural analysis on the access door designs with an ultimate transverse pressure load of 1.5 psi placed on the skin, in the direction of the skin causing compression in the skin, to determine the resulting stresses in the part.

Figure 5.13 shows the results for the model used for the stress analysis of the HT-23 access door design. This model is partitioned at the point of near symmetry on the door, which is along the center of the panel. The actual panel model is not truly symmetrical about this line, but the degree of asymmetry is minimal and is not expected to affect the results of the model. The model boundary conditions consisted of a fixed roller along the partition line and a pinned support along the edge of the exterior stiffeners. The material type used for the HT-23 panel model was elastic with a modulus of elasticity of 866 ksi and a Poisson's ratio of 0.40. This modulus of elasticity is the average modulus for the vertically printed HT-23 tension coupons (see Subsection 2.3.2). The modulus of elasticity for the vertical coupons was used because it is conservative, but there is not a large enough deviation in stiffness from the flat printed coupons that it becomes unreasonable to use vertically printed parts in practice. The Poisson's ratio

of 0.40 was selected because the Poisson's ratio of polymers can vary from 0.32 to 0.49 [Polymer Properties Database, 2021].

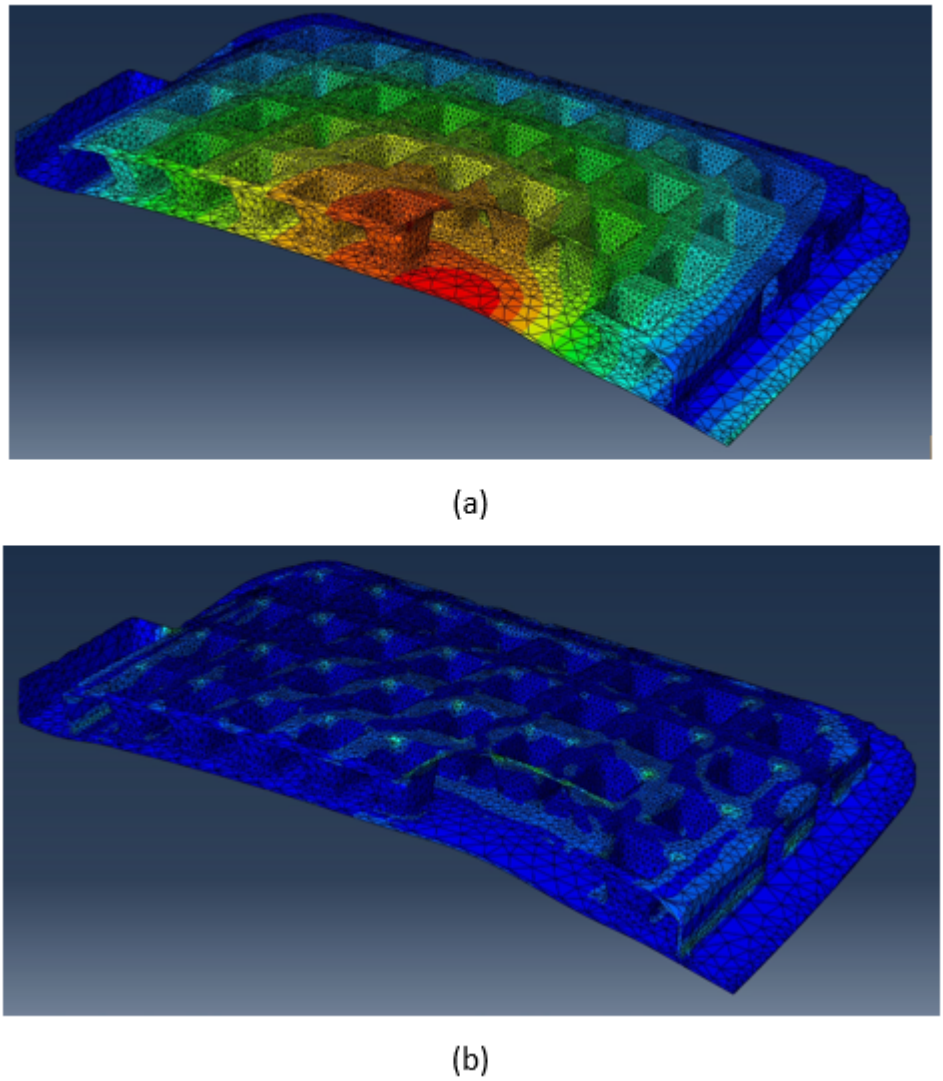

FIGURE 5.13: (a) HT-23 door deflection contour from static pressure load
(b) HT-23 door stress contour from static pressure load

The results of this model show that the peak stress in the access door does not exceed 5.04 ksi or 60% of the fracture stress of the vertically printed tension coupons. Since the stresses in the part do not exceed yield or fracture stresses under the ultimate pressure load, a service level pressure load was not used for analysis.

To perform the yield and fracture stress check for the ThermaX PEEK access door, the

same model was used. However, the modulus in the model was changed to be 505 ksi. This modulus is the average modulus of the [-45,+45] flat tension coupons. Here the vertical printed coupon modulus was not used because, unlike with SLS printing, the vertical part performance of FFF parts is significantly poorer than flat printed parts. Due to this, it would be unlikely that this access door would be printed vertically and therefore the vertical coupon values were not used in the model. The geometry from the HT-23 panel was used to analyze the ThermaX PEEK part because the ThermaX PEEK part uses a similar geometry but the part thickness is increased. This means that the results from this model would be conservative for the ThermaX PEEK design. The results of the analysis showed that the maximum stress in the part does not exceed 5.11 ksi. The fracture stress of [-45,+45] flat printed tension coupons was 10.8 ksi (see Subsection 2.3.5). The yield stress of the ThermaX PEEK occurs at 80% to 90% of the fracture stress (see Subsection 3.2.5) which would make the yield stress in the model 8.64 ksi conservatively. This means that the maximum stress in the model did not exceed 60% of the yield stress of the material. Since the stresses in the part do not exceed yield or fracture stresses under the ultimate pressure load, a service level pressure load was not used for analysis.

5.4.2 Buckling Check

This subsection discusses the results of the structural analysis on the access door designs with a transverse pressure load placed on the skin to determine what load causes buckling.

The material properties and boundary conditions were the same as in the models used in the previous subsection. Figure 5.14 shows the results of the model for the HT-23 access door design.

The first buckling mode of the access door occurs from the local buckling of the gap in the stiffener grid where the access door handle is located. The pressure load on the

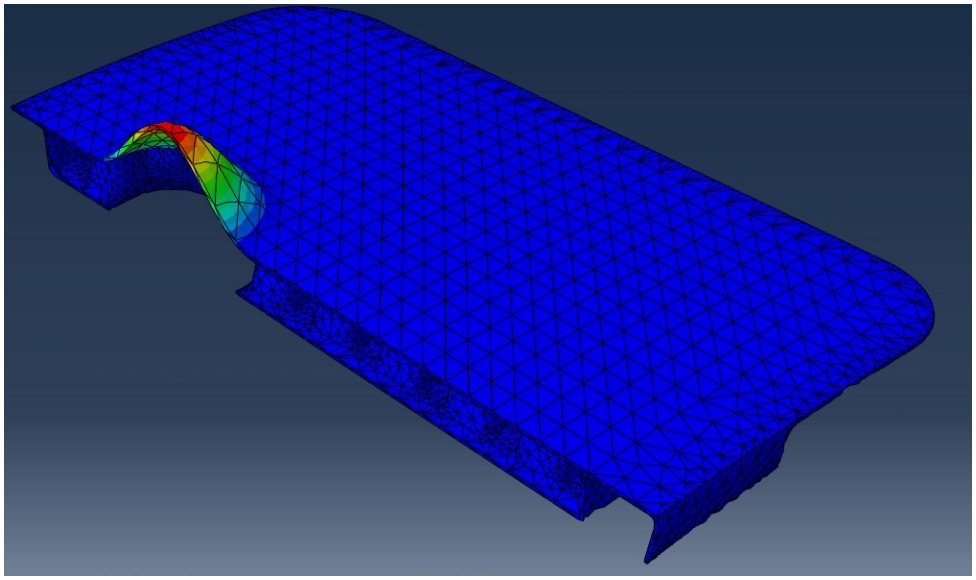

FIGURE 5.14: HT-23 door first buckling mode (exaggerated deflection)

skin, which is a transverse pressure load causing buckling on the compression flange, that caused this buckling was 11.2 psi which is significantly higher than the expected ultimate load.

To determine the buckling load for the ThermaX PEEK door, the same model was used; however, the modulus was changed to be 505 ksi. The buckling mode occurred in the same way as shown in Figure 5.14, in which there is local buckling in the handle location of the access door. The pressure load on the skin, which is a transverse pressure load causing buckling on the compression flange, that caused this buckling was 6.56 psi which is significantly higher than the expected ultimate load.

The models used for HT-23 and ThermaX PEEK show that the access door is conservative for yield stress, fracture stress, and buckling under the expected ultimate transverse pressure load during a flight. This is a result of the fact that the panel design is governed by the global stiffness needed to limit excess deflections. Some design checks that were not performed but could be considered are performing analysis on the access doors when they are subjected to impact and wind loads. After the structural analysis was completed, testing components of the access door was done (see Chapter 6).

6 Component Testing

6.1 Overview

This chapter discusses the testing and analysis of the sub-component testing performed during this project. Ideally, it would be best to test the full-size access door; however, Boeing and the University of Washington do not have SLS or FFF printers large enough to print the whole part. Due to this, sub-components of the access door were printed to test the performance of the stiffeners in the panel. The sub-component tests were limited to Onyx due to time and printer access limitations. Thus, this chapter provides a qualitative study to guide future component tests. The main concern with the stiffener grid used in this project was the strength of the bond between the stiffener webs and flanges. The strength of 3D printed junctions is a large knowledge gap. Much focus has been placed on coupons, but there is a need to characterize built-up parts.

To determine how much deformation could occur in the bond before delamination, T-beam sub-components were printed as seen in Figure 6.1. It can be seen here that the T-beam was printed with attachments for the Instron grips. The grip attachments were printed with an arrowhead shape to help place the load to the centroid of the T-beam cross-section. The T-beams were tested in compression until buckling occurred.

FIGURE 6.1: T-beam before test

6.2 Component Testing Results

Two T-beams were printed and tested with the Onyx material in the flat print orientation. The results of the first test are presented in Figure 6.2. This T-beam was compressed past the point of buckling, and the test was stopped before delimitation between the web and flange occurred. The buckled T-beam at the end of test can be seen in Figure 6.3, which shows torsional buckling of the T-beam.

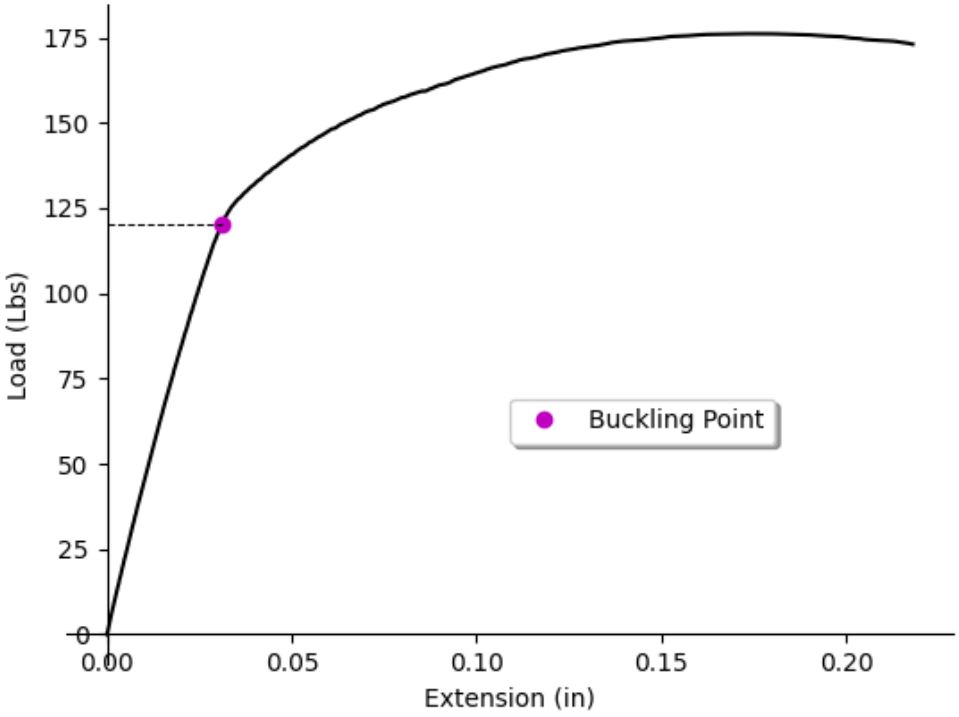

FIGURE 6.2: First T-beam test load vs extension curve

FIGURE 6.3: First T-beam buckled shape at end of test

The results of the second test are presented in Figure 6.4.

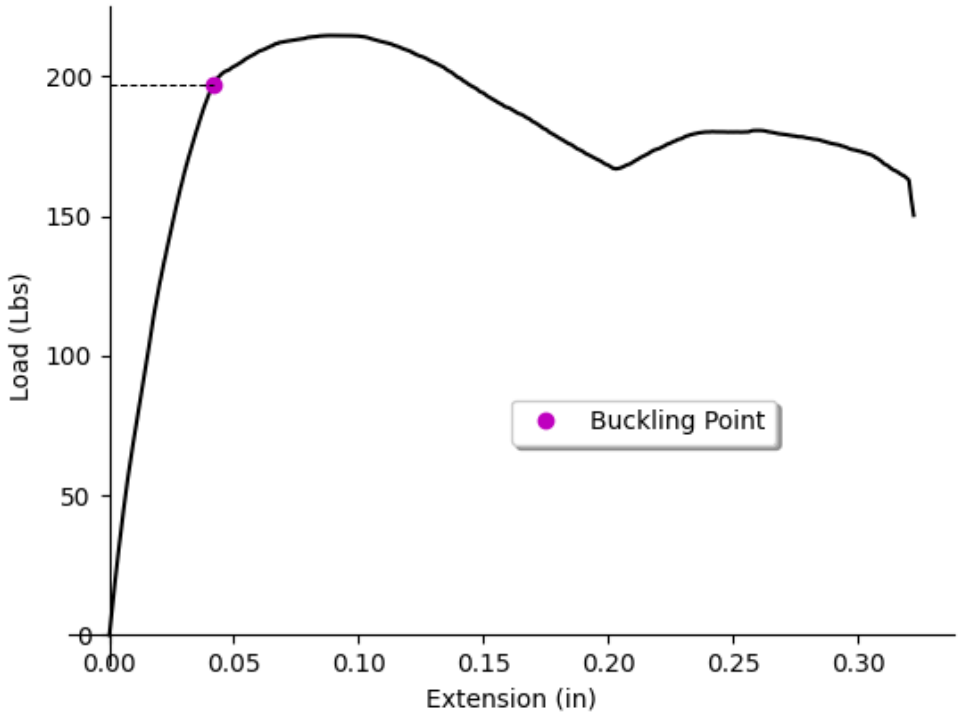

FIGURE 6.4: Second T-beam test load vs extension

This T-beam was compressed past the point of buckling until delimitation occurred between the web and flange. The buckled and delaminated T-beam at the end of test can be seen in Figure 6.5.

FIGURE 6.5: Second T-beam buckled shape at end of test

It can be seen from the test results that the bond between the web and the flange was strong enough to survive buckling of the T-beam. The T-beam was able to be compressed significantly past the buckling point before delamination of the web and flange occurred. While these tests were performed only for Onyx and not for HT-23 and ThermaX PEEK, which are the materials recommended for future use on this project, they do provide qualitative insight into the performance of the stiffeners on the access door. The sub-component buckling tests show that for a material with sufficient ductility, such as Onyx, delamination is unlikely to occur before or at the point of buckling under compressive loading. ThermaX PEEK has shown the potential to have high ductility (see Chapter 3) which means that the T-beams for this material would likely behave similarly to the Onyx T-beams. On the other hand, HT-23 is very brittle. This highly brittle behavior of HT-23 would likely cause an immediate fracture to occur at the point of buckling for a T-beam printed with HT-23.

Due to delamination occurring far after the point of buckling for the T-beams tested and the fact that buckling needs to be avoided in the access door, delamination before the buckling point is unlikely to be an issue for the access door.

6.3 FEM Analysis

While the test results of the T-beams provide qualitative insight into the behavior of the stiffeners of the access door, this section will discuss the stresses between the web and flange that developed at the buckling point of the T-beam. The stress at the web to flange connection on the T-beam at the buckling load was determined by running a buckling analysis in Abaqus. The buckled model from Abaqus can be seen in Figure 6.6.

The boundary conditions for this model were to fix the sides of one grip attachment to simulate the bottom grip on the Instron machine, and the other grip attachment was

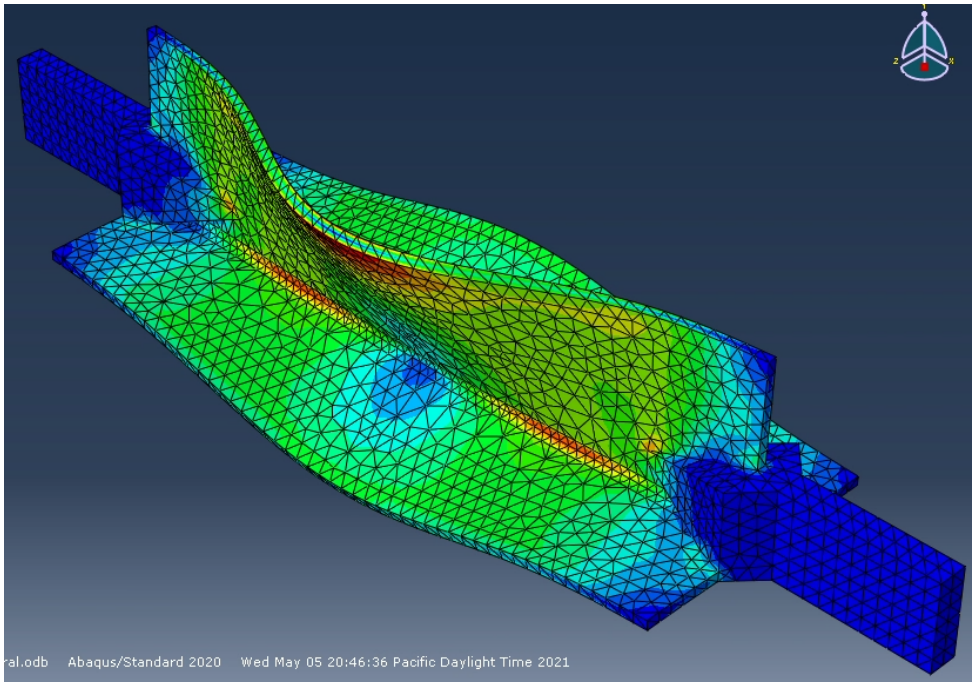

FIGURE 6.6: Abaqus T-beam buckling model stress contour

treated as a fixed roller. The fixed roller allowed displacement in the axial direction only. The loading was applied as a surface traction in the axial direction at the location the fixed roller was placed to simulate the loading from the Instron machine.

The greatest stresses appear at the connection between the web and the flange. Additionally, it can be seen that the buckling mode of the T-beam in the Abaqus model matches the torsional buckling mode seen during the testing of the T-beams. The model shown in Figure 6.6 represents the first T-beam that was tested. The buckling load from this model was 119 lbs which produced a maximum von Mises stress of 0.182 ksi at the web to flange connection. Another model was run with the stiffness of the second T-beam that was tested. The buckling load of that model was 195 lbs with a maximum von Mises stress at the web to flange connection of 0.299 ksi. These stress levels are far below even the vertical tension coupon fracture stresses (see Subsection 2.3.3). While it is good to know that delamination of the flange to web connections would be unlikely to occur even upon buckling of the stiffeners, it would be ideal to repeat these tests and analyses for the material used on the actual part (see Chapter 7).

7 Conclusions and Future Work

7.1 Conclusions

This project identified HT-23 and ThermaX PEEK to be recommended as the best material candidates for future work from the preliminary material selection. This decision was based on the stiffness and strength seen during coupon testing. Additionally, these materials showed high resistance to permanent deformation and degradation due to temperature cycling.

This project identified a test method to determine the approximate yield point of the polymer material systems used. This test method was to cyclically load coupons in tension to increasing stress levels. The stress level at which permanent deformation and loading stiffness degraded was taken to be the yield stress of the material. This test method found that ThermaX PEEK has a yield stress that is 80% to 90% of the fracture stress and that HT-23 behaves elastically until brittle fracture.

This project identified strategies for using structural supports to help ensure successful vertical prints of thin parts for FFF printing. While the use of structural supports was shown to be a successful method of producing thin vertical prints, the project also found that vertical printing of thin parts should be avoided in critical load locations. Vertically printed FFF coupons demonstrated low performance when compared to flat prints of the same material. While it can be economically feasible to treat an SLS material as isotropic for design using the vertical print properties as conservative design values, this is not recommended for FFF printing. This recommendation is due to the

SLS vertical coupons performing only slightly poorer than the flat prints, while the FFF vertical coupons performed much more poorly than the flat prints.

Material system behavior was found to be partially dependent on coupon shape and size for FFF material systems. This was done by testing coupons of varying shapes and thicknesses. The results of this testing showed that the shell layer appears to have a role in the material system behavior for parts that have small cross-sectional areas.

A test protocol was created to determine the effects of print layer time on the performance of vertically printed tensile coupons. This protocol showed that cold joints created from prolonged layer times appear to have more of an effect on ductility than on strength and stiffness.

The project identified a suitable geometry that would be compatible with the additive manufacturing of polymers and the needs of a part requiring the ability to drain liquid. This geometry was a waffle grid of hat stiffeners. This waffle grid combined the advantages of an open stiffener geometry and a sandwich panel by allowing for drainage of liquid and powder but also providing high stiffness. This waffle grid also leverages the primary advantage of additive manufacturing which is being able to produce parts with complex geometries that would not otherwise be cost-effective or feasible with other manufacturing processes.

Through component testing, the project gave a qualitative guide to future component tests. The component testing performed in this project showed that for adequately ductile materials, the bond between the flanges and webs of a stiffener will not fail even when buckling occurs.

7.2 Recommendations for Future Work

The work in this project in regards to the sub-components and full access door has been preliminary exploration. There is a need to more robustly test and analyze these parts in the future.

Additional environmental degradation testing should also be performed for the materials recommended in this project. While these materials were subjected to hot and cold temperature cycles, the moisture in the environmental chambers was not able to be controlled. To better simulate real-world conditions, temperature cycling should be conducted simultaneously with humidity control. Along with the additional environmental testing that should be completed, paint adhesion testing should be performed. The paint placed on a part is critical to the part's resistance to environmental degradation.

There is also a need to determine how drilling affects printed parts with the materials recommended from this project. If drilling can be performed on additively manufactured parts printed with these materials, those parts will become much more versatile.

There is a need to determine the impact response of the materials recommended for this project. While impact response testing was not included in this project, the access door does have impact resistance requirements. Testing should be performed to determine if the materials recommended are suitable to the resistance of impact loads. This is especially important for HT-23 due to its brittle behavior. With its brittle behavior, it is expected that it will perform poorly when subjected to impact loading. The required impact testing could determine if HT-23 is still a strong candidate for the access door or for other parts with impact requirements.

While vertical printing with FFF printers was successful enough to produce coupons to test, further work should be done to help improve the stability and performance of vertically printed FFF parts. Along with this, another study should be done to help

relegate the challenges presented when trying to remove support material from a complex FFF additively manufactured part.

Lastly, more structural testing should be completed. This testing should include more sub-component testing for the materials to be used on the final part, as well as testing of the full-scale part. This additional testing will be the best way to expose any potential problems with the part design, and it will be the best way to determine if the part is ready for use.

A Tension Testing Method

The tension testing in this project was conducted in accordance with ASTM D638-14 [*Standard Test Method for Tensile Properties of Plastics* 2014]. The coupons used for the tension testing were the Type I, Modified Type I, Type II, and Type V coupons. The Type I coupon is the preferred coupon shape for coupons with a thickness of 7 mm or less made with Rigid or Semi-rigid Plastics, and it was the main coupon used for tension testing in this project. A rigid plastic is defined as a plastic with a modulus greater than 100 ksi [*Standard Terminology Relating to Plastics* 2019]. All of the materials used in this project have a modulus higher than 100 ksi, and the largest thickness of a coupon used in this project did not exceed 7 mm. The Modified Type I coupon is not a coupon suggested by ASTM. Instead, the Modified Type I coupon has the same geometry as the Type I coupon with a shorter narrow section that was used to investigate the effect of coupon size on printed part performance (see Chapter 3). The Type II coupon is recommended when a material does not break in the narrow section of the Type I coupon. Many coupons tested with the Type I coupon did break at the radius, however, the Type I coupon was still used to stay consistent in the testing between the different materials. The Type II coupon was used to investigate the effect of coupon size on printed part performance (see Chapter 3). The Type V coupon is recommended for when there is limited material to be tested, or when a large number of specimens are to be exposed in a limited space, such as in an environmental stability test. The Type V coupon was used to investigate the effect of coupon size on printed part performance and for conducting the environmental study on ThermaX PEEK (see Subsection 2.3.5 and Chapter 3). The different coupon shapes can be seen in Figure A.1.

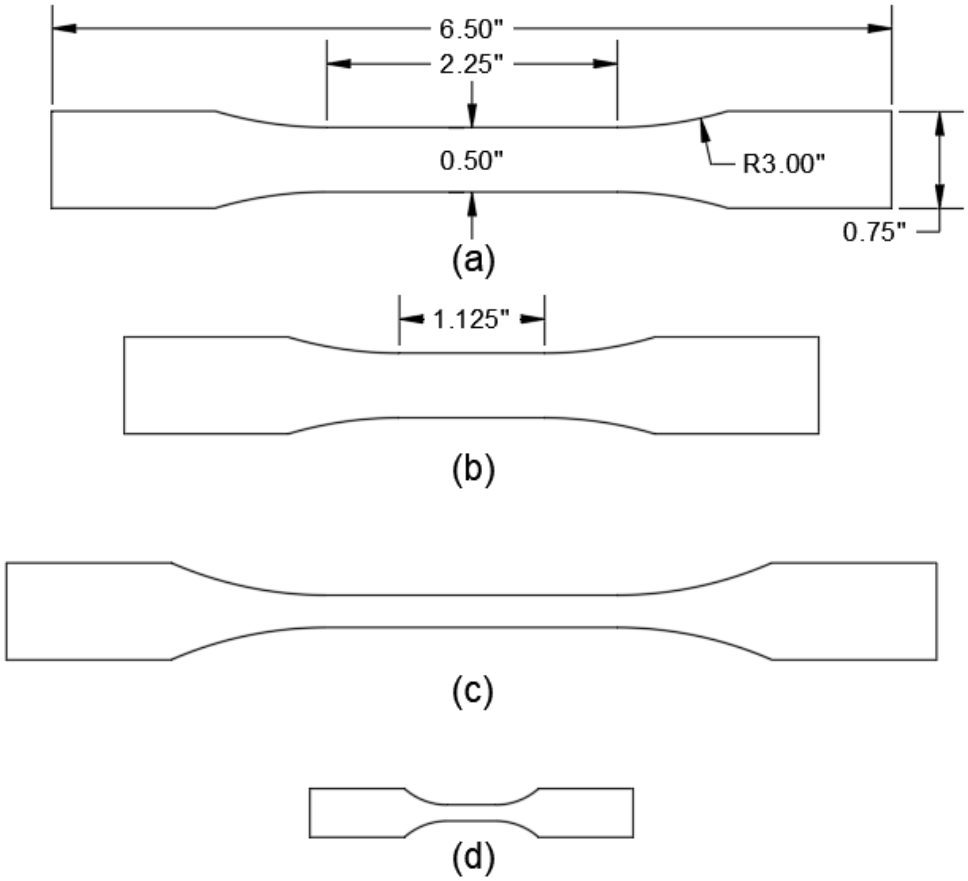

FIGURE A.1: (a) Type I coupon (b) Modified Type I coupon (c) Type II coupon (d) Type V coupon

For the Type I, Modified Type I, and Type II coupons, the strain was measured using an extensometer. For the Type V coupons, the strain was measure using a video extensometer because the narrow section was too short to measure with a physical extensometer. The extension rate was 5 mm/min for all tension tests. An image of the test setup for the Type I coupons can be seen in Figure A.2. All of the tension moduli in this thesis are initial tangent moduli unless otherwise stated. An image of the test setup for the Type V coupons can be seen in Figure A.3.

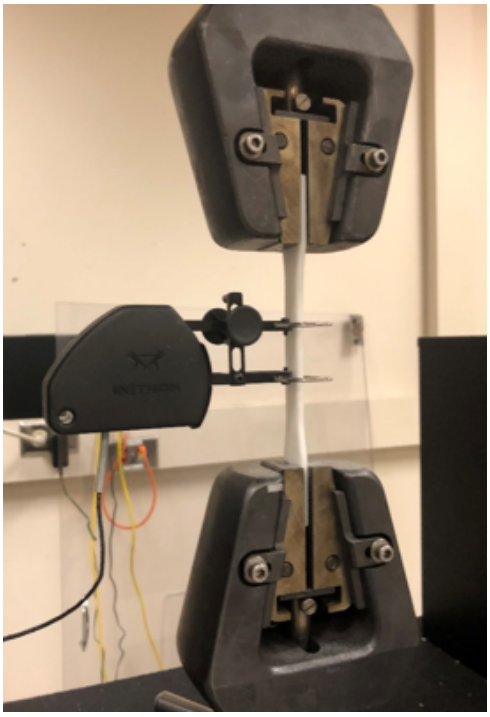

FIGURE A.2: FR-106 Type I tension coupon test setup

FIGURE A.3: Onyx Type V tension coupon test setup

B Bending Testing Method

The bending tests in this project were conducted in accordance with ASTM D790-17 [*Standard Test Methods for Flexural Properties of Unreinforced and Reinforced Plastics and Electrical Insulating Materials* 2017]. The coupons used for the bending tests were 0.50 in wide, 0.13 in thick, and 5 in long, and they were tested at a 16:1 span-to-depth ratio. All of the bending tests performed were 3 point bending tests. All tension tests were stopped at a maximum strain of 0.05 mm/mm if the coupon had not broken yet. This is done because beyond this strain value, bending no longer governs the behavior of the coupon. The rate of extension was calculated using the following equation:

$$R = \frac{ZL^2}{6d}$$

$R =$ rate of crosshead motion, mm/min

$L =$ support span, mm

$d =$ depth of beam, mm

$Z =$ rate of straining of the outer fiber, $\frac{mm}{min}/min$

ASTM suggests the use of two rates of outer fiber straining. The standard value is 0.01 mm/mm/min. If the coupons do not break before the 0.05 mm/mm strain limit, the rate of outer fiber straining is allowed to be increased to 0.10 mm/mm/min. It was common for the bending coupons in this project to not break before the end of test was reached; therefore, both outer fiber straining rates were used. Additionally, many of these materials displayed a toe region at the start of the stress-strain curves.

This toe region seen in many stress-strain curves is often artificial and due to the take-up of slack and alignment or seating of the specimen [*Standard Test Method for Tensile Properties of Plastics* 2014]. To obtain correct values for the materials, a correction has already been made in the figures in Section 2.3. An image of the test setup for the bending tests can be seen in Figure B.1.

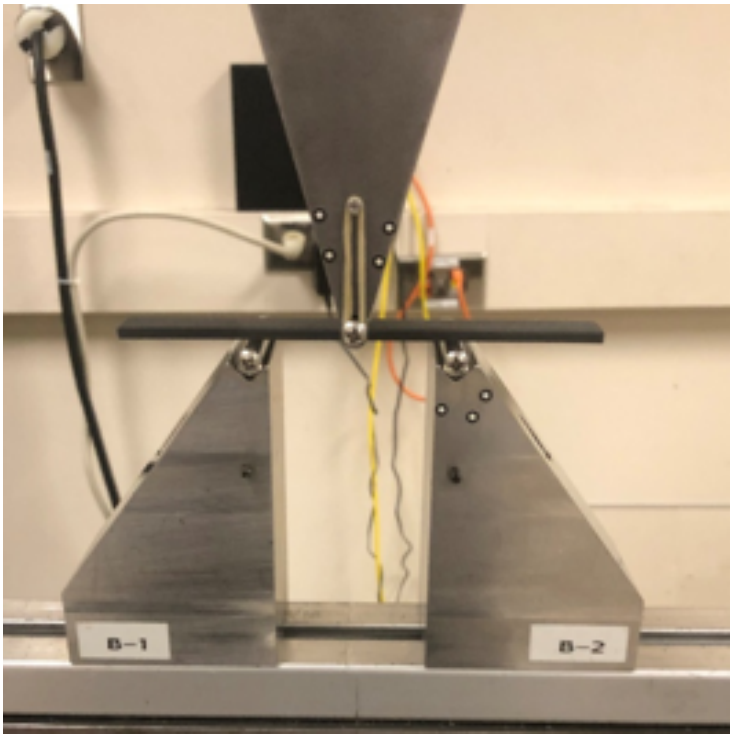

FIGURE B.1: HT-23 bending coupon test setup

Bibliography

[1] Advanced Laser Mechanics. *HT-23 Overview*. https://alm-llc.com/portfolio-items/ht-23/.

[2] H. Al-Qrimli, F. Mahdi, and F. Ismail. "Carbon/Epoxy Woven Composite Experimental and Numerical Simulation to Predict Tensile Performance". In: *Advances in Materials Science and Applications* 4.2 (2015), pp. 33–41.

[3] J. Cantrell et al. "Experimental Characterization of the Mechanical Properties of 3D-Printed ABS and Polycarbonate Parts". In: *Advancement of Optical Methods in Experimental Mechanics, Volume 3*.

[4] *FR-106 - Material Specifications*. Tech. rep. 3115 Lucius McCelvey, Temple, TX 76504: Advanced Laser Materials.

[5] Gedney, Richard. *Measuring the Ductility of Metals*. ADMET, Inc.

[6] Gregurić, Leo. *SLS 3D Printing: Selective Laser Sintering Simply Explained*. https://all3dp.com/2/selective-laser-sintering-sls-3d-printing-simply-explained/. Accessed: 2021-04-07. 2019.

[7] Ani Chen Chuin-Shan Zehnder Alan Ingraffea Anthony Billington Sarah Han Tong-Seok Ural. "Delamination buckling and propagation analysis of honeycombpanels using a cohesive element approach". In: *International Journal of Fracture* 115.2 (2002), pp. 101–123.

[8] Hexcel Corporation. *HexAM Additive Manufacturing*. https://www.hexcel.com/Products/Parts-and-Structures/AdditiveManufacturing. Accessed: 2021-04-07. 2021.

[9] *HT-23 - Material Specifications*. Tech. rep. 3115 Lucius McCelvey, Temple, TX 76504: Advanced Laser Materials.

[10] Markforged. *3D Printer Types Technologies*. https://markforged.com/resources/learn/3d-printing-basics. Accessed: 2021-04-07. 2021.

[11] Markforged. *3D Printing Settings Impacting Part Strength*. https://markforged.com/resources/learn/design-for-additive-manufacturing-plastics-composites/understanding-3d-printing-strength/3d-printing-settings-impacting-part-strength. Accessed: 2021-04-07. 2021.

[12] Markforged. *Onyx*. https://markforged.com/materials/plastics/onyx?utm_source=google&utm_medium=cpc&utm_campaign=12054191260&utm_content=115709747949&utm_term=onyx%203d%20printer&gclid=Cj0KCQjwsLWDBhCmARIsAPSL3_1084ilzDUSoZ3e7t5KzYXrIim5BCNcmwke9EcwcB. Accessed: 2021-04-07. 2021.

[13] *Material Datasheet - Composites*. Tech. rep. 4.0. 480 Pleasant St, Watertown, MA 02472: Markforged, 2020.

[14] *Material Descriptions - Composites*. Tech. rep. 4.0. 480 Pleasant St, Watertown, MA 02472: Markforged, 2020.

[15] MechaniCalc Inc. *Mechanical Properties of Materials*. https://mechanicalc.com/reference/mechanical-properties-of-materials. Accessed: 2021-04-16. 2021.

[16] Polymer Properties Database. *Typical Poisson's Ratios of Polymers at Room Temperature*. http://polymerdatabase.com/polymer%20physics/Poisson%20Table.html. Accessed: 2021-05-04. 2021.

[17] M. Rinaldi et al. "Additive layer manufacturing of poly (ether ether ketone) via FDM". In: *Composites Part B: Engineering* 145 (2018), pp. 162–172.

[18] *Standard Terminology Relating to Plastics*. Tech. rep. D883-19a. West Conshohocken, PA: ASTM International, 2019.

[19] *Standard Test Method for Tensile Properties of Plastics*. Tech. rep. D638-14. West Conshohocken, PA: ASTM International, 2014.

[20] *Standard Test Methods for Flexural Properties of Unreinforced and Reinforced Plastics and Electrical Insulating Materials*. Tech. rep. D790-17. West Conshohocken, PA: ASTM International, 2017.

[21] *Technical Data Sheet: ThermaX™ PEEK 3D Printing Filament*. Tech. rep. 3.0. 3DXTECH, 2021.

[22] Ansel C. Ugural and Saul K. Fenster. *Advanced Mechanics of Materials and Applied Elasticity Fifth Edition*. Boston, MA: Prentice Education, Inc., 2012.

[23] Varotsis, Alkaios B. *Introduction to FDM 3D printing*. `https://www.3dhubs.com/knowledge-base/introduction-fdm-3d-printing/`. Accessed: 2021-04-07. 2021.

[24] Varotsis, Alkaios B. *Introduction to SLS 3D printing*. `https://www.3dhubs.com/knowledge-base/introduction-sls-3d-printing/`. Accessed: 2021-04-07. 2021.